ESTIMATION OF CEREBRAL PHYSIOLOGY AND HEMODYNAMICS VIA NEAR-INFRARED SPECTROSCOPY

by

Jeffrey W Barker

Bachelor of Science, Pennsylvania State University, 2010

Submitted to the Graduate Faculty of

the Swanson School of Engineering in partial fulfillment

of the requirements for the degree of

Doctor of Philosophy

University of Pittsburgh

2014

UNIVERSITY OF PTTSBURGH

SWANSON SCHOOL OF ENGINEERING

This dissertation was presented

by

Jeffrey W Barker

It was defended on

November 25, 2014

and approved by

Patrick Loughlin, PhD, Professor
Department of Bioengineering

Tamer Ibrahim, PhD, Associate Professor
Department of Bioengineering

Ashok Panigrahy, MD, Associate Professor
Department of Radiology

Alberto Vazquez, PhD, Assistant Professor
Department of Bioengineering

Dissertation Director: Theodore Huppert, PhD, Associate Professor
Department of Radiology

ESTIMATION OF CEREBRAL PHYSIOLOGY AND HEMODYNAMICS VIA NEAR-INFRARED SPECTROSCOPY

Jeffrey W Barker, PhD

University of Pittsburgh, 2014

Near-infrared spectroscopy (NIRS) is a non-invasive optical imaging technique that has rapidly been gaining popularity for study of the brain. Near-infrared spectroscopy measures absorption of light, primarily due to hemoglobin, through an array of light sources and detectors that are coupled to the scalp. Measurements can generally be divided into measurements of baseline physiology (related to total absorption) and measurements of hemodynamic time-series data (related to relative absorption changes). Because light intensity drops off rapidly with depth, NIRS measurements are highly sensitive to extracerebral tissues. Attempts to recover baseline physiology measurements of the brain can be confounded by high sensitivity to the scalp and skull. Time-series measurements contain high contributions of systemic physiology signals, including cardiac, respiratory, and blood pressure waves. Furthermore, measurements over time inevitably introduce artifacts due to subject motion.

The aim of this thesis was to develop improved analysis methods in the context of these NIRS specific confounding factors. The thesis consists of four articles that address specific issues in NIRS data analysis: (i) assessment of common data analysis procedures used to estimate oxygen saturation and hemoglobin content that assume a semi-infinite, homogeneous medium, (ii) testing the feasibility of improving oxygen saturation and hemoglobin measurements using multi-layered models, (iii) development of methods to estimate the general linear model for functional brain imaging that are robust to systemic physiology signals and motion artifacts, and (iv) the extension of (iii) to an adaptive method that is suitable for real-time analysis. Overall, this thesis helps to validate and advance analysis methods for NIRS.

TABLE OF CONTENTS

LIST OF TABLES

LIST OF FIGURES

1.0 INTRODUCTION

Near infrared spectroscopy (NIRS) is a non-invasive method for measuring brain physiology and hemodynamics that has rapidly been gaining popularity. Near infrared spectroscopy measures optical absorption, primarily due to hemoglobin, from an array of light sources and optical detectors coupled to the scalp. Applications of NIRS to the brain are generally divided into two goals: (i) estimation of baseline physiology, such as oxygen saturation, hemoglobin content, or blood flow and (ii) analysis of hemodynamic time-series data, such as with functional brain imaging or resting state connectivity. This body of work will examine data analysis issues within the context of both of these goals.

Near-infrared spectroscopy instruments are relatively portable compared to other modalities such as MRI or PET. This makes NIRS especially useful to applications where portability is an advantage. In the context of physiological measurements, NIRS is especially suitable for bedside monitoring. Several previous studies have shown promising results in applications to monitoring cerebral physiology during cardiac surgery [1, 2], detecting hypoxic or ischemic brain injuries in neonatal populations [3, 4]. Approximately 40% of patients experience long-term post-operative cognitive decline after cardiopulmonary bypass surgery [5], and approximatey 25% of neonates with hypoxic-ischemic brain injury will suffer from long-term neurological disorders, including behavioral deficits, mental impairment, visual dysfunction, hyperactivity, cerebral palsy, and epilepsy [6]. Bedside monitoring with NIRS has potential to make a significant impact in patient care.

Light in the visible range has poor penetration into tissues due to especially high absorption by hemoglobin. Infrared light exhibits very high absorption by water. Light between 650-900 nm is often called the optical window, where absorption of light by tissues is a few orders of magnitude lower, which allows light to penetrate a few centimeters into tissues, reaching the outer portion of the cortex; however, light intensity falls off rapidly with depth, which can make NIRS analysis challenging, and NIRS measurements are significantly influenced by extracerebral tissues. In the

context of baseline physiology estimation, it can be difficult to separate absorption due to the scalp and skull from absorption in the brain.

For functional brain imaging, the portability of NIRS allows it to be used where other modalites, such as functional MRI are not practical, such as walking [7, 8], balance [9, 10, 11], and social interaction [12]. However, the high sensitivity to superficial tissues introduces high contributions of systemic physiology, including cardiac, respiratory, and blood pressure waves, to the NIRS time-series data. Additionally, motion can cause slippage of the probe from scalp causing sharp artifacts in the data. Together these sources of noise deteriorate the performance of analysis methods that aim to detect evoked hemodynamic changes that are related to task performance or stimulus conditions.

The main goal of this thesis was to develop improved analysis methods for both estimation of baseline physiology and the detection of evoked hemodynamic changes. The main contributions of this work to the field are: (i) assessment of common data analysis procedures used to estimate oxygen saturation and hemoglobin content that assume a semi-infinite, homogeneous medium, (ii) testing the feasibility of improving oxygen saturation and hemoglobin measurements using multi-layered anatomical models, (iii) development of methods to estimate the general linear model for functional brain imaging that are robust to systemic physiology signals and motion artifacts, and (iv) the extension of this method to an adaptive estimator that is also robust to motion and systemic physiology and is suitable for real-time analysis.

The contents of this thesis are as follows: Chapter 2 gives an overview of background information, including an overview of light interactions with tissue, the physics governing light propagation through tissues, solutions to light propagation in simple geometries, numerical methods for computation of light propagation, and an introduction to functional NIRS analysis. Chapter 3 gives an assessment of the use of a semi-infinite, homogeneous slab model of the head for estimation of oxygen saturation and total hemoglobin content in a neonate model using FD-NIRS. Chapter 4 investigates multi-layered models for improved estimation of tissue hemoglobin in neonates. Chapter 5 develops a new method for fNIRS data analysis that is robust to systemic physiology and motion artifacts. Chapter 6 extends the work from chapter 5 to an adaptive algorithm that is suitable for real-time fNIRS analysis. Finally, chapter 7 concludes the thesis.

2.0 BACKGROUND

This chapter covers the background behind NIRS measurements and data analysis. Section 2.1 reviews the interactions of light with tissue. Section 2.2 discusses the materials and instruments used to obtain NIRS measurements. Section 2.3 gives a detailed overview of the models governing light propagation through tissues, including an overview of numerical techniques. Finally, section 2.4 discusses the methods used for modeling evoked hemodynamics in the context of functional brain imaging.

2.1 OPTICAL PROPERTIES OF TISSUES

2.1.1 Absorption

Absorption is a physical process in which the energy of a photon is taken up by matter. For media without scattering, the probability of photon absorption per unit distance travelled is given by the absorption coefficient μ_a. Thus, the attenuation of light follows the following differential equation:

$$\frac{dI}{d\ell} = -\mu_a \, I \ , \tag{2.1}$$

whose solution gives the Beer-Lambert law:

$$I = I(0) \ e^{-\mu_a \ell} \ , \tag{2.2}$$

where ℓ is the distance traveled through the medium. The absorption coefficient can be parameterized in terms of the concentration of chromophores in the medium:

$$\mu_a = \sum_j \epsilon_j c_j \ , \tag{2.3}$$

where c_j is the concentration of chromophore j, and ϵ is the extinction coefficient.

The main sources of absorption (chromophores) in tissues are melanin, water, lipid, hemoglobin, myoglobin, and cytochromes [13]. The interval of wavelengths between approximately 650-900 nm (the optical window) allows light to penetrate tissue and be used for non-invasive optical spectroscopy. Wavelengths below this range are in the visible spectrum, in which absorption by hemoglobin and other chromophores is very high. Wavelengths above this range are in the infrared region where absorption by water dominates. Figure 2.1 illustrates main components contributing to the absorption spectrum for brain tissue.

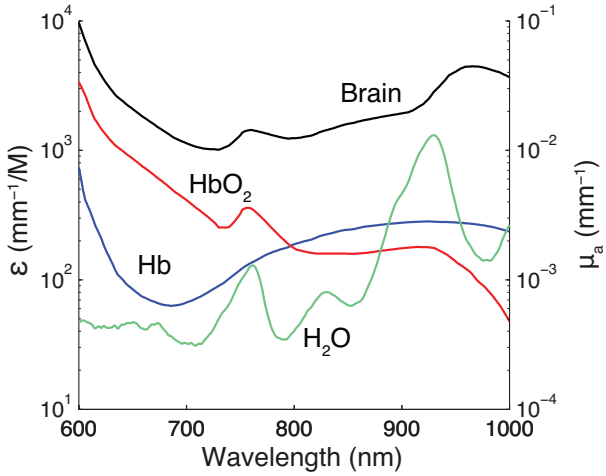

Figure 2.1: Absorption spectra of components in the brain. The extinction coefficients (left axis) are shown for oxyhemoglobin (HbO_2, red) and deoxyhemoglobin (Hb, blue). The absorption coefficients (right axis) are shown for water and brain tissue. The absorption coefficients for brain were calculated assuming 40 μM HbO_2, 20 μM Hb, 70% water content, and negligible absorption from other sources.

2.1.2 Scattering

Scattering describes the change in direction of photons due to collisions with matter. Mie scattering theory describes the scattering of photons off of a sphere [14]. In the limit that the radius of the sphere is much smaller than the wavelength of light, this reduces to Rayleigh scattering. Thus, scattering off of particles smaller than the wavelength of the light is typically referred to as Rayleigh scattering, and scattering off of particles on same order or larger than the than the wavelength is referred to Mie scattering, although Mie scattering theory generally describes both cases [14]. In

biological tissues, only very small structures, such and microtubules and filaments will exhibit Rayleigh scattering in the near-infrared region [13]. Scattering off of larger structures, such as whole red blood cells, large organelles (mitochondria, lysosomes, etc.), and myelin sheathes will exhibit Mie scattering [13]. Other structures, such as centrioles, the Golgi apparatus, and the endoplastic reticulum, may be somewhere between the Rayleigh and Mie scattering regimes.

Single scattering events are probabilistic with the probability of a photon traveling a distance x before scattering given by an exponential distribution:

$$p(x) = \mu_s \, e^{-\mu_s \, x} \, , \tag{2.4}$$

where μ_s is the scattering coefficient. In tissues, scattering is highly anisotropic, favoring only small deflections from the forward direction. Often, the Henyey-Greenstein function [15] is used to model the probability of the polar scattering angle:

$$p(\theta) = \frac{1}{4\pi} \frac{1 - g^2}{(1 + g^2 - 2g\cos(\theta))^{3/2}} \, , \tag{2.5}$$

where g is the anisotropy factor. Figure 2.2 illustrates the probability density functions for different values of g.

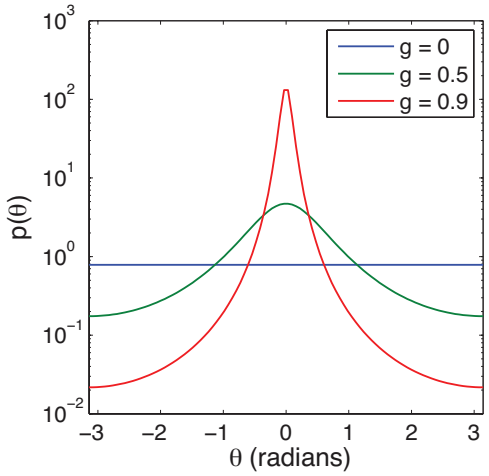

Figure 2.2: Probability density functions for different anisotropic factors. Note the log scale on the y-axis.

In tissues, the photons undergo many scattering events, in which the light behaves much like a diffusion process (see section 2.3.2). In this case, we are typically interested in the reduced scattering coefficient:

$$\mu_s' = (1-g)\ \mu_s \tag{2.6}$$

$$g = \ \langle \cos\theta \rangle\ , \tag{2.7}$$

where the angle brackets denote the mean value. The reduced scattering coefficient gives the scattering coefficient of a an equivalent isotropic scattering process for modeling light propagation through tissue that is valid when scattering is much greater than absorption.

From Mie scattering theory, we can model the wavelength dependence of the scattering coefficient as

$$\mu_s' = a\left(f\left(\frac{\lambda}{500\ \text{nm}}\right)^{-4} + (1-f)\left(\frac{\lambda}{500\ \text{nm}}\right)^{-b}\right)\ , \tag{2.8}$$

where the left term models Rayleigh scattering with the fraction of Rayleigh scattering components given by f; a is an overall scaling term that gives μ_s' at 500 nm; and b is the exponent associated with Mie scattering off of large particles. The rapidly decaying λ^{-4} dependence of Rayleigh scattering shows that Mie scattering may often dominate the scattering interactions in tissues, unless f is particularly high.

The high degree of scattering increases the average pathlength of detected photons, introducing correction terms to the Beer-Lambert law:

$$I = I(0)\ e^{-\mu_a \ell \cdot \text{DPF} + G}\ , \tag{2.9}$$

where DPF is the differential pathlength factor, and G is a term associated with geometry [16]. This equation is often referred to as the modified Beer-Lambert law (MBLL).

2.1.3 Refractive Index

The third major property of tissues is refractive index. Refractive index governs the speed of light propagating through a medium, the reflection and transmittance of light through a boundary, and the change of direction of light transmitted through a boundary (refraction). The speed of light through a medium is given by

$$\nu = \frac{c}{n}\ , \tag{2.10}$$

where n is the refractive index, and c is the speed of light in a vacuum (2.998×10^{11} mm/s). The interface between two media is illustrated in Fig. 2.3. For reflected photons, the angle of incidence (θ_i) equals the angle of reflection (θ_r). Transmitted photons change direction according to Snell's law:

$$n_i \ \sin\theta_i = n_t \ \sin\theta_t \ . \tag{2.11}$$

The fraction of reflected photons is given by R, referred to as reflectance, reflectivity, or reflection coefficient. According to Fresnel's law, the reflection coefficient for s-polarized (R_s, perpendicular to the plane in Fig. 2.3) and p-polarized (R_p, parallel with the plane in Fig. 2.3) are given by

$$R_s = \left(\frac{n_i \cos\theta_i - n_t \cos\theta_t}{n_i \cos\theta_i + n_t \cos\theta_t} \right)^2 \tag{2.12}$$

$$R_p = \left(\frac{n_i \cos\theta_t - n_t \cos\theta_i}{n_i \cos\theta_t + n_t \cos\theta_t} \right)^2 \ , \tag{2.13}$$

and the relection coefficient for unpolarized light is simply given by

$$R = \ \frac{1}{2}(R_s + R_p) \ . \tag{2.14}$$

In the context of NIRS, reflection is important to consider at the tissue/air interface and also at the interface of two tissues with significantly different refractive indices, such as the interface between the brain and cerebrospinal fluid (CSF). These equations can either be applied directly when simulating photons propaging through a medium, such as with Monte Carlo methods, or to derive appropriate boundary conditions when computing light propagation via other methods.

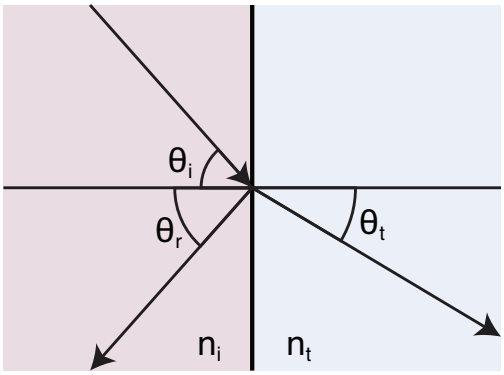

Figure 2.3: Illustration of an interface between two optical media with different refractive indices.

2.2 INSTRUMENTATION

There are three main types of NIRS measurements: continuous wave (CW), frequency-domain (FD), and time-resolved (TR). These measurements are illustrated in Fig. 2.4. Continuous wave NIRS uses light sources that are constantly on and measures the attenuation of the light. Often, CW-NIRS measurements are only used to investigate the temporal changes in the signal due to physiology, such as task-evoked changes or resting state dynamics. The main advantage of CW-NIRS is that it has the least stringent requirements for light sources, detectors, and on-board signals processing hardware. Thus, many CW systems combine a large number of inexpensive laser diode light sources with photodiode detectors to achieve many measurement channels in a relatively inexpensive system.

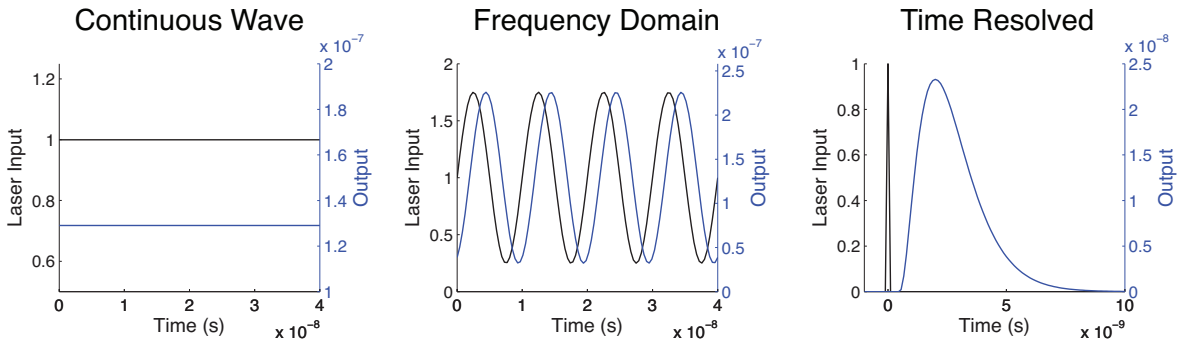

Figure 2.4: Illustration of the different types of NIRS measurements. Note the different y-axes pertaining to the input (left) and output (right).

Frequency domain systems use a light source that is sinusoidally amplitude modulated. Thus, the light intensity is given by

$$I(\boldsymbol{r}, t) = D(\boldsymbol{r}) + A(\boldsymbol{r}) \sin\left(\omega_s t + \phi(\boldsymbol{r})\right) \ , \tag{2.15}$$

where D is the DC amplitude; A is the AC amplitude; ω_s is the modulation frequency of the source; and $\phi(\boldsymbol{r})$ is the phase. In general, D, A, and ϕ depend on the position ($\boldsymbol{r}$), the geometry of the optical medium, and optical properties of the medium. The modulation frequency is typically around 100 MHz, which prevents wrapping of the phase offset. In order to measure the AC and phase terms, the output signal is converted to a lower frequency via a heterodyne system, in

which the signal from the detector is modulated at another frequency ω_d. The mixing of the two frequencies is given by

$$\tilde{I}(\boldsymbol{r}_d, t) = [D(\boldsymbol{r}_d) + A(\boldsymbol{r}_d)\sin(\omega_s t + \phi(\boldsymbol{r}_d))] \times [B + C\sin(\omega_d t))] \ , \tag{2.16}$$

where B and C are the DC and AC amplitudes of the signal being mixed with the output of the detector, and $\boldsymbol{r}_d$ is the position of the detector. Using a trigonometric identity this can be rewritten as

$$\begin{aligned}\tilde{I}(\boldsymbol{r}_d, t) = BD(\boldsymbol{r}_d) &- \frac{1}{2}CA(\boldsymbol{r}_d)\sin((\omega_s - \omega_d)t + \phi(\boldsymbol{r}_d)) \\ &+ \frac{1}{2}CA(\boldsymbol{r}_d)\sin((\omega_s + \omega_d)t + \phi(\boldsymbol{r}_d)) \\ &+ CD(\boldsymbol{r}_d)\sin(\omega_d t)) \\ &+ BA(\boldsymbol{r}_d)\sin(\omega_s t + \phi(\boldsymbol{r}_d)) \ .\end{aligned} \tag{2.17}$$

Thus, if we choose the modulation frequencies appropriately, we can now extract A and ϕ from a much lower frequency signal equal to the difference between the modulation of frequencies $(\omega_s - \omega_d)$. For example, the Imagent ISS system modulates the sources at 110 MHz and the detectors at 110.005 MHz, producing a 5 kHz signal. The last three terms in the result above can be removed by low pass filtering in hardware. Many FD-NIRS analysis methods rely on the changes in these values over multiple source-detector distances. Thus, these systems have more strict technical requirements in terms of dynamic range for the detectors. Furthermore, the light sources must be capable of amplitude modulation at ∼100 MHz, and additional on-board hardware is necessary to perform the signal processing necessary to extract the DC, AC, and phase values at specified sampling rate (∼2 Hz). Therefore, FD-NIRS hardware is usually more expensive than CW.

Time-resolved NIRS systems use a very short laser pulse (on the order of 100s of femtoseconds), followed by measurement of the arrival time of a single photon (if a photon reaches the detector). Light pulses are sent into the tissue at a rate of ∼100 MHz, and a histogram of the photon time-of-flight measurements is estimated (see [17] for a review of TR-NIRS). Because TR-NIRS has high technical requirements for hardware, it is typically the most expensive of the three techniques.

In the context of baseline physiology estimation, CW-NIRS measurements do not give any direct information about optical pathlength. This makes accurate quantification of hemoglobin difficult without making assumptions about scattering. The FD-NIRS systems obtain direct information about optical pathlength by measuring the phase change over multi-distance measurements. The

larger the phase offset, the longer it took light to reach the detector and the longer the optical path-length. This information improves the quantification of tissue hemoglobin. The FD-NIRS signal is related to the TR-NIRS signal by a discrete Fourier transform at a particular modulation frequency. Thus, we can view TR-NIRS measurements as having the same information as if we had obtained FD-NIRS measurements at all modulation frequencies. Therefore, TR-NIRS measurements should contain the most information for quantification of hemoglobin. However, the hardware requirements for obtaining TR-NIRS measurements make the instruments more expensive than other CW-NIRS or FD-NIRS instruments. Furthermore, TR-NIRS systems are less portable and are currently not as widely available as CW or FD systems.

Figure 2.5 shows three examples of NIRS systems. The Techen CW6 system shown is a CW system with 32 photodiode detectors and 32 lasers (16 $\times$ 690 nm and 16 $\times$ 830 nm). The Imagent ISS is a FD-NIRS system that is modulated at 110 MHz. It offers 4 photomultiplier tube detectors and 32 lasers. The particular system shown in Fig. 2.5 offers 7 wavelengths between 690 nm and 830 nm, although more common setups have only 690 nm and 830 nm lasers. While the CW6 and ISS systems fit onto a cart and are portable, the subjects are still restricted to the length of the fiber optics connected to the system. The Techen system shown on the right in Fig. 2.5, run the fiber optics to a small box that the subject attaches to their waist via a belt. Data is then sent from the system to a computer via Bluetooth, allowing subject to move freely within a range of 75 m. The design constraints of the portable instrument restricts the system to 6 photodiode detectors and 8 lasers (4 $\times$ 690 nm and 4 $\times$ 830 nm).

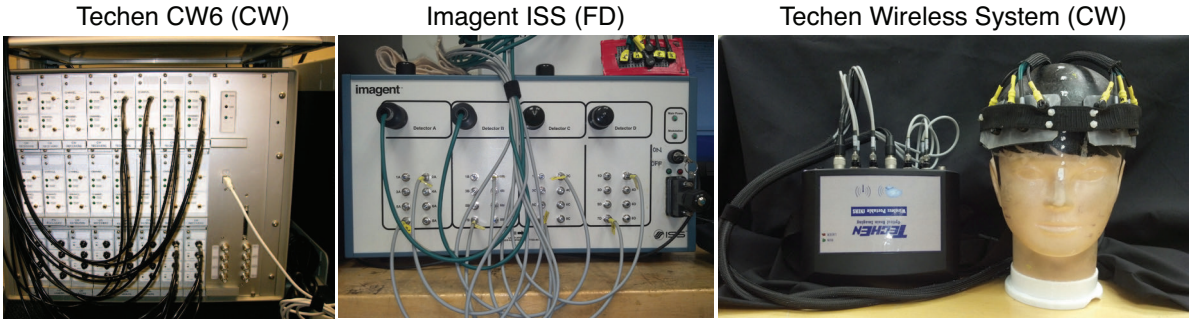

Figure 2.5: (left) Techen CW6 CW-NIRS system with 32 avalanche photodiode detectors and 32 lasers (center) Imagent ISS FD-NIRS system with 4 photomultiplier tube detectors and 32 lasers. (right) Techen wireless CW-NIRS system with 6 photodiode detectors and 8 lasers.

The NIRS instruments are coupled to the subject via fiber optic cables that are arranged in a specific layout or probe design, depending on the purpose of the measurement. Source fibers are often bifurcated so that lasers of two wavelengths can output light to the same optode (the end of the fiber that is placed on the skin). Figure 2.6 shows an example of a bifurcated source fiber. An example CW probe is shown in Fig. 2.7. Because the probe was used for functional brain imaging, the layout was designed for spatial coverage of the brain regions of interest, with all of the measurements at the same source-detector distance. Figure 2.8 shows an example of a simple FD-NIRS probe that was designed for maximum number of source-detector distances.

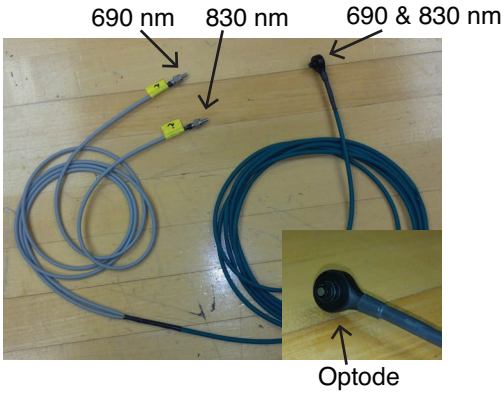

Figure 2.6: A bifurcated source fiber that achieves overlapping measurements at two wavelengths.

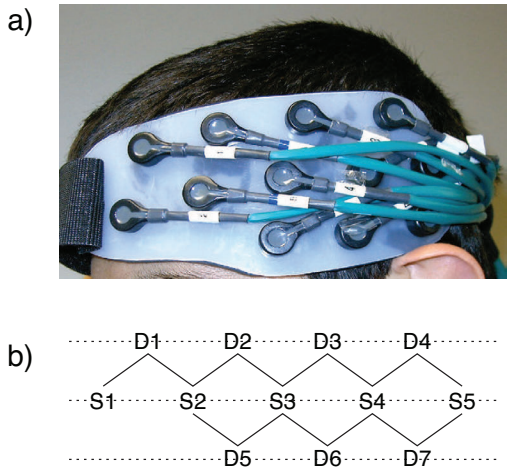

Figure 2.7: (a) An example CW-NIRS probe designed for functional brain imaging. (b) The source-detector geometry. Measurements have the same source-detector distance, and the probe layout was designed for the desired spatial coverage.

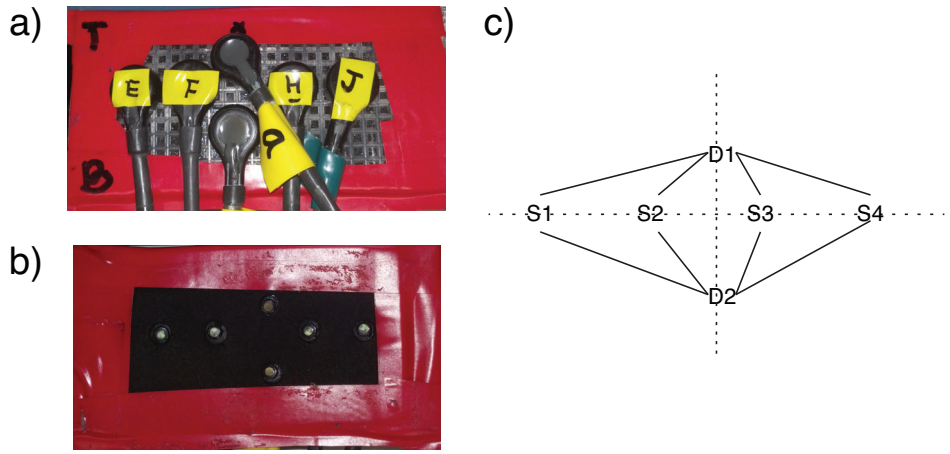

Figure 2.8: A simple FD-NIRS probe. (a) The outside of the probe. (b) The skin side of the probe. (c) The sources and detectors are arranged such that there are 8 unique distances.

2.3 LIGHT PROPAGATION IN TISSUES

2.3.1 Radiative Transfer Equation

Light propagation through tissue can be modeled as particles (photons) transported through a medium via the radiative transfer equation (RTE), which can be derived from conservation of energy [18]. The photon density $L(\boldsymbol{r}, \hat{\Omega}, t)$ at a position $\boldsymbol{r}$, solid angle $\hat{\Omega}$, and at time t is given by:

$$\begin{aligned}\frac{1}{\nu}\frac{\partial}{\partial t}L(\boldsymbol{r}, \hat{\Omega}, t) = &- \hat{\Omega} \cdot \nabla L(\boldsymbol{r}, \hat{\Omega}, t) - (\mu_a + \mu_s)\ L(\boldsymbol{r}, \hat{\Omega}, t) \\ &+ \mu_s \int L(\boldsymbol{r}, \hat{\Omega}', t)\ f(\hat{\Omega}, \hat{\Omega}')\ d\hat{\Omega}' + S(\boldsymbol{r}, \hat{\Omega}, t)\ ,\end{aligned} \tag{2.18}$$

where ν is the speed of light in the medium determined by the refractive index; $f(\hat{\Omega}', \hat{\Omega})$ is the probability density of scattering from a direction $\hat{\Omega}$ to a new direction $\hat{\Omega}'$; μ_a and μ_s are the absorption and scattering coefficients; and $S(\boldsymbol{r}, \hat{\Omega}, t)$ defines contributions from a light source. Note that in heterogeneous media, μ_a and μ_s are generally a function of position ($\boldsymbol{r}$). The RTE can be solved generally using Monte Carlo methods to simulate photons propagating through a medium with scattering and absorption, but at high computational expense with current computers.

2.3.2 Diffusion Approximation

Under certain assumptions, the RTE can be reduced to a simpler diffusion equation. First, some integrals that come up repeatedly are

$$\int d\hat{\Omega} = 4\pi \tag{2.19}$$

$$\int \hat{\Omega}\ d\hat{\Omega} = 0 \tag{2.20}$$

$$\int (\boldsymbol{A} \cdot \hat{\Omega})\ \hat{\Omega}\ d\hat{\Omega} = \frac{4\pi}{3}\boldsymbol{A}\ , \tag{2.21}$$

where in the last expression, $\boldsymbol{A}$ is independent of $\hat{\Omega}$. The results above can be derived by writing out the terms for $\hat{\Omega}$ and $\mathrm{d}\hat{\Omega}$ in terms of Cartesian coordinates:

$$\hat{\Omega} = \sin\theta\cos\phi\ \hat{\mathbf{x}} + \sin\theta\sin\phi\ \hat{\mathbf{y}} + \cos\theta\ \hat{\mathbf{z}} \tag{2.22}$$

$$d\hat{\Omega} = \sin\theta\ d\theta\ d\phi \tag{2.23}$$

where θ is the polar angle, and ϕ is the azimuthal angle, integrated from 0 to π and from 0 to 2π, respectively. A first order expansion of radiance can be written as

$$L(\boldsymbol{r}, \hat{\Omega}, t) \approx L_0(\boldsymbol{r}, t) + \boldsymbol{L}_1(\boldsymbol{r}, t) \cdot \hat{\Omega}\ . \tag{2.24}$$

This expression is equivalent to a first degree approximation of L using spherical harmonics (i.e., see [19]). Next, we will assume an isotropic light source:

$$S(\boldsymbol{r}, \hat{\Omega}, t) = \frac{1}{4\pi} S_0(\boldsymbol{r}, t) \ , \tag{2.25}$$

where the $1/4\pi$ has been added for convenience. Lastly, we will assume that distribution of scattering angles f only depends on the angle between $\hat{\Omega}$ and $\hat{\Omega}'$.

$$f(\hat{\Omega}, \hat{\Omega}') = f(\hat{\Omega} \cdot \hat{\Omega}') \tag{2.26}$$

A first order expansion of f around $(\hat{\Omega} \cdot \hat{\Omega}') = 0$ is given by

$$f(\hat{\Omega} \cdot \hat{\Omega}') \approx f_0 + f_1 \ (\hat{\Omega} \cdot \hat{\Omega}') \tag{2.27}$$

$$f(\cos\gamma) \approx f_0 + f_1 \cos\gamma \ , \tag{2.28}$$

where γ is the angle between $\hat{\Omega}$ and $\hat{\Omega}'$. Using a coordinate system that points in the direction of $\hat{\Omega}$, such that γ is the polar angle, we can find the coefficients f_0 and f_1. The first coefficient is found evaluating the following integral:

$$f(\cos\gamma) = f_0 + f_1 \cos\gamma \tag{2.29}$$

$$\int_0^{2\pi} \int_0^{\pi} f(\cos\gamma) \ \sin\gamma \ d\gamma \ d\phi = \int_0^{2\pi} \int_0^{\pi} (f_0 + \cancel{f_1 \cos\gamma}) \sin\gamma \ d\gamma \ d\phi \tag{2.30}$$

$$1 = 4\pi \ f_0 \tag{2.31}$$

$$f_0 = \frac{1}{4\pi} \tag{2.32}$$

where we have used the fact that $f(\cos\gamma)$ is a probability distribution over all 4π steraradians and must integrate to one. We can find the coefficient f_1 by multiplying by both sides of the equation $\cos\gamma$ and integrating:

$$f(\cos\gamma)\cos\gamma = f_0 \cos\gamma + f_1 \cos^2\gamma \tag{2.33}$$

$$\int_0^{2\pi} \int_0^{\pi} f(\cos\gamma) \ \cos\gamma \ \sin\gamma \ d\gamma \ d\phi = \int_0^{2\pi} \int_0^{\pi} (\cancel{f_0 \cos\gamma} + f_1 \cos^2\gamma) \sin\gamma \ d\gamma \ d\phi \tag{2.34}$$

$$\langle \cos\gamma \rangle = \frac{4\pi}{3} f_1 \tag{2.35}$$

$$f_1 = \frac{3}{4\pi} \langle \cos\gamma \rangle = \frac{3}{4\pi} \ g \tag{2.36}$$

where the angle brackets indicate the expectation of the enclosed quantity. Thus, the anisotropy factor g is given by the average of the cosine of the scattering angle. The final expression for f is given by

$$f(\hat{\Omega} \cdot \hat{\Omega}') \approx \frac{1}{4\pi} + \frac{3g}{4\pi} \ (\hat{\Omega} \cdot \hat{\Omega}') \ . \tag{2.37}$$

Two defined quantities of interest are fluence rate ($\Phi(\boldsymbol{r},t)$) and current density ($\boldsymbol{J}(\boldsymbol{r},t)$) given by the following definitions:

$$\Phi(\boldsymbol{r},t) \equiv \int L(\boldsymbol{r},\hat{\Omega},t)\; d\hat{\Omega} \tag{2.38}$$

$$\boldsymbol{J}(\boldsymbol{r},t) \equiv \int L(\boldsymbol{r},\hat{\Omega},t)\; \hat{\Omega}\; d\hat{\Omega}\;. \tag{2.39}$$

If we plug our approximation in Eq. 2.24 into the definitions above for fluence rate and current density, we can find their relationship to $L_0(\boldsymbol{r},t)$ and $\boldsymbol{L}_1(\boldsymbol{r},t)$:

$$\begin{aligned}
\Phi(\boldsymbol{r},t) &= \int L_0(\boldsymbol{r},t)\; d\hat{\Omega} + \int (\boldsymbol{L}_1(\boldsymbol{r},t)\cdot\hat{\Omega})\; d\hat{\Omega} \\
&= L_0(\boldsymbol{r},t)\int d\hat{\Omega} + \boldsymbol{L}_1(\boldsymbol{r},t)\cdot\cancel{\int \hat{\Omega}\, d\hat{\Omega}} \\
&= 4\pi\; L_0(\boldsymbol{r},t) \qquad (2.40)\\
\boldsymbol{J}(\boldsymbol{r},t) &= \int L_0(\boldsymbol{r},t)\;\hat{\Omega}\; d\hat{\Omega} + \int (\boldsymbol{L}_1(\boldsymbol{r},t)\cdot\hat{\Omega})\;\hat{\Omega}\; d\hat{\Omega} \\
&= L_0(\boldsymbol{r},t)\cancel{\int \hat{\Omega}\, d\hat{\Omega}} + \frac{4\pi}{3}\boldsymbol{L}_1(\boldsymbol{r},t) \\
&= \frac{4\pi}{3}\boldsymbol{L}_1(\boldsymbol{r},t)\;, \qquad (2.41)
\end{aligned}$$

for which we have used the results in Eqs. 2.19-2.21 to perform the integrals. Thus, we can rewrite Eq. 2.24 as

$$L(\boldsymbol{r},\hat{\Omega},t) \approx \frac{1}{4\pi}\Phi(\boldsymbol{r},t) + \frac{3}{4\pi}\boldsymbol{J}(\boldsymbol{r},t)\cdot\hat{\Omega}\;. \tag{2.42}$$

Using our first order expansions for f (Eq. 2.37) and L (2.42), we can now simplify the integral term in the RTE (Eq. 2.18):

$$\begin{aligned}
\int L(\boldsymbol{r},\hat{\Omega}',t)\; f(\hat{\Omega},\hat{\Omega}')\; d\hat{\Omega}' &= \int \left(\frac{1}{4\pi}\Phi(\boldsymbol{r},t) + \frac{3}{4\pi}\boldsymbol{J}(\boldsymbol{r},t)\cdot\hat{\Omega}'\right)\;\left(\frac{1}{4\pi} + \frac{3g}{4\pi}\;(\hat{\Omega}\cdot\hat{\Omega}')\right)\; d\hat{\Omega}' \\
&= \frac{3}{16\pi^2}\Phi(\boldsymbol{r},t)\int d\hat{\Omega}' \\
&\quad + \frac{3g}{16\pi^2}\Phi(\boldsymbol{r},t)\;\hat{\Omega}\cdot\cancel{\int \hat{\Omega}'\, d\hat{\Omega}'} \\
&\quad + \frac{3}{16\pi^2}\;\boldsymbol{J}(\boldsymbol{r},t)\cdot\cancel{\int \hat{\Omega}'\, d\hat{\Omega}'} \\
&\quad + \frac{3g}{16\pi^2}\;\hat{\Omega}\cdot\int (\boldsymbol{J}(\boldsymbol{r},t)\cdot\hat{\Omega}')\;\hat{\Omega}'\; d\hat{\Omega}' \\
&= \frac{1}{4\pi}\Phi(\boldsymbol{r},t) + \frac{3g}{4\pi}\boldsymbol{J}(\boldsymbol{r},t)\cdot\hat{\Omega}\;, \qquad (2.43)
\end{aligned}$$

again using the results in Eqs. 2.19-2.21 to perform the integrals. Thus, Eq. 2.18 can be rewritten as

$$\frac{1}{\nu}\frac{\partial}{\partial t}L(\boldsymbol{r},\hat{\Omega},t) = -\hat{\Omega}\cdot\nabla L(\boldsymbol{r},\hat{\Omega},t) - (\mu_a+\mu_s)\ L(\boldsymbol{r},\hat{\Omega},t) + \mu_s\left(\frac{1}{4\pi}\Phi(\boldsymbol{r},t) + \frac{3g}{4\pi}\boldsymbol{J}(\boldsymbol{r},t)\cdot\hat{\Omega}\right) + \frac{1}{4\pi}S_0(\boldsymbol{r},t)\ . \tag{2.44}$$

We can get a scalar differential equation by integrating both sides of the equation over all 4π steraradians:

$$\begin{aligned}\frac{1}{\nu}\frac{\partial}{\partial t}\int L(\boldsymbol{r},\hat{\Omega},t)\ d\hat{\Omega} = &-\nabla\cdot\int\hat{\Omega}\ L(\boldsymbol{r},\hat{\Omega},t)\ d\hat{\Omega}\\ &-(\mu_a+\mu_s)\int L(\boldsymbol{r},\hat{\Omega},t)\ d\hat{\Omega}\\ &+\mu_s\ \frac{1}{4\pi}\Phi(\boldsymbol{r},t)\int d\hat{\Omega}\\ &+\mu_s\ \frac{3g}{4\pi}\boldsymbol{J}(\boldsymbol{r},t)\cdot\cancel{\int\hat{\Omega}\ d\hat{\Omega}}\\ &+\frac{1}{4\pi}S_0(\boldsymbol{r},t)\int d\hat{\Omega}\end{aligned} \tag{2.45}$$

where we have used the indentity $\hat{\Omega}\cdot\nabla L(\boldsymbol{r},\hat{\Omega},t) = \nabla\cdot(\hat{\Omega}L(\boldsymbol{r},\hat{\Omega},t)) - L(\boldsymbol{r},\hat{\Omega},t)\nabla\cdot\hat{\Omega}$, noting that $\nabla\cdot\hat{\Omega} = 0$. This simplifies to

$$\frac{1}{\nu}\frac{\partial}{\partial t}\Phi(\boldsymbol{r},t) = -\nabla\cdot\boldsymbol{J}(\boldsymbol{r},t) - \mu_a\ \Phi(\boldsymbol{r},t) + S_0(\boldsymbol{r},t)\ . \tag{2.46}$$

Next, we multiply both sides of Eq. 2.44 by $\hat{\Omega}$ and integrate over all 4π steraradians to obtain a vectorial differential equaiton:

$$\begin{aligned}\frac{1}{\nu}\frac{\partial}{\partial t}\int\hat{\Omega}L(\boldsymbol{r},\hat{\Omega},t)\ d\hat{\Omega} = &-\frac{1}{4\pi}\int(\hat{\Omega}\cdot\nabla\Phi(\boldsymbol{r},t))\ \hat{\Omega}\ d\hat{\Omega}\\ &\cancel{-\frac{3}{4\pi}\int(\hat{\Omega}\cdot\nabla(\boldsymbol{J}(\boldsymbol{r},t)\cdot\hat{\Omega})\ \hat{\Omega}\ d\hat{\Omega}}\\ &-(\mu_a+\mu_s)\int\hat{\Omega}L(\boldsymbol{r},\hat{\Omega},t)\ d\hat{\Omega}\\ &+\mu_s\ \frac{1}{4\pi}\Phi(\boldsymbol{r},t)\cancel{\int\hat{\Omega}\ d\hat{\Omega}}\\ &+\mu_s\ \frac{3g}{4\pi}\int\hat{\Omega}(\boldsymbol{J}(\boldsymbol{r},t)\cdot\hat{\Omega})\ d\hat{\Omega}\\ &+\frac{1}{4\pi}S_0(\boldsymbol{r},t)\cancel{\int\hat{\Omega}\ d\hat{\Omega}}\end{aligned} \tag{2.47}$$

where the second term can be shown to cancel to zero by writing out all the terms using Eqs. 2.22 and 2.23 and showing that each term integrates to zero. The equation above simplifies to

$$\begin{aligned}\frac{1}{\nu}\frac{\partial}{\partial t}\boldsymbol{J}(\boldsymbol{r},t) &= -\frac{1}{3}\nabla\Phi(\boldsymbol{r},t) - (\mu_a + (1-g)\mu_s)\boldsymbol{J}(\boldsymbol{r},t) \\ &= -\frac{1}{3}\nabla\Phi(\boldsymbol{r},t) - (\mu_a + \mu_s')\boldsymbol{J}(\boldsymbol{r},t)\ ,\end{aligned} \tag{2.48}$$

where the quantity $\mu_s' = (1-g)\mu_s$ is the reduced scattering coefficient. After making the assumption that left-hand side goes to zero, we get

$$\boldsymbol{J}(\boldsymbol{r},t) = -\frac{\nabla\Phi(\boldsymbol{r},t)}{3(\mu_a + \mu_s')} = -D\ \nabla\Phi(\boldsymbol{r},t)\ , \tag{2.49}$$

where the term $D = 1/(3\mu_a + 3\mu_s')$ is the diffusion coefficient. Finally, plugging Eq. 2.49 into Eq. 2.46, we get the diffusion approximation in the time domain:

$$\frac{1}{\nu}\frac{\partial}{\partial t}\Phi(\boldsymbol{r},t) - \nabla\cdot(D\ \nabla\Phi(\boldsymbol{r},t)) + \mu_a\ \Phi(\boldsymbol{r},t) = S_0(\boldsymbol{r},t)\ . \tag{2.50}$$

Applying a Fourier transform to both sides, we get the final result

$$-\nabla\cdot(D\ \nabla\tilde{\Phi}(\boldsymbol{r},\omega)) + \left(\mu_a + \frac{i\omega}{\nu}\right)\tilde{\Phi}(\boldsymbol{r},\omega) = \tilde{S}_0(\boldsymbol{r},\omega)\ , \tag{2.51}$$

using the property that the Fourier transform of the derivative of a function is the Fourier transform of the function multiplied by $i\omega$. The diffusion approximation can be solved analytically for a few simple geometries and numerically using finite element methods.

2.3.3 Infinite Homogeneous Medium

The diffusion approximation can be solved analytically for an infinite, homogeneous medium [20]. Starting with Eq. 2.51, we can expand the first term and simplify:

$$\cancel{-\nabla\Phi(\boldsymbol{r},\omega)\cdot\nabla D} - D\nabla^2\Phi(\boldsymbol{r},\omega) + \left(\mu_a + \frac{i\omega}{\nu}\right)\Phi(\boldsymbol{r},\omega) = S(\boldsymbol{r},\omega) \tag{2.52}$$

$$\nabla^2\Phi(\boldsymbol{r},\omega) - \left(\frac{\mu_a}{D} + \frac{i\omega}{\nu D}\right)\Phi(\boldsymbol{r},\omega) = -\frac{S(\boldsymbol{r},\omega)}{D}\ , \tag{2.53}$$

where $\nabla D = 0$ in a homogeneous medium. Note that we have dropped the tilde notation and subscript zero on the source term. Making a substitution for constants in the second term gives

$$(\nabla^2 + \kappa^2)\Phi(\boldsymbol{r},\omega) = -\frac{S(\boldsymbol{r},\omega)}{D} \tag{2.54}$$

$$\kappa^2 = -\left(\frac{\mu_a}{D} + \frac{i\omega}{\nu D}\right)\ , \tag{2.55}$$

which is the inhomogeneous Helmholtz equation. Noting that $(\nabla^2 + \kappa^2)$ is translation invariant, Eq. 2.54 can be solved for any arbitrary function on the right-hand side using the Green's function $G(\boldsymbol{r}, \omega)$ as follows:

$$(\nabla^2 + \kappa^2)\Phi(\boldsymbol{r}, \omega) = F(\boldsymbol{r}, \omega) \tag{2.56}$$

$$\Phi(\boldsymbol{r}, \omega) = \int F(\boldsymbol{r}', \omega)\ G(\boldsymbol{r} - \boldsymbol{r}', \omega)\ d^3\boldsymbol{r}' \tag{2.57}$$

where $G(\boldsymbol{r}, \omega)$ is given by the solution to the following equation:

$$(\nabla^2 + \kappa^2)G(\boldsymbol{r}, \omega) = \delta^3(\boldsymbol{r})\ . \tag{2.58}$$

Applying a Fourier transform to the equation above gives

$$\int (\nabla^2 + \kappa^2)G(\boldsymbol{r}, \omega)\ e^{-i\boldsymbol{s}\cdot\boldsymbol{r}}\ d^3\boldsymbol{r} = \int \delta^3(\boldsymbol{r})\ e^{-i\boldsymbol{s}\cdot\boldsymbol{r}}\ d^3\boldsymbol{r} \tag{2.59}$$

which can be solved algebraically to find the Green's function as a function of spatial frequency $\boldsymbol{s}$:

$$(-s^2 + \kappa^2)\tilde{G}(\boldsymbol{s}, \omega) = 1 \tag{2.60}$$

$$\tilde{G}(\boldsymbol{s}, \omega) = \frac{1}{\kappa^2 - s^2}\ , \tag{2.61}$$

where s is the length of the vector $\boldsymbol{s}$. Now, we can invert the Fourier transform to get back to the spatial domain:

$$G(\boldsymbol{r}, \omega) = \frac{1}{8\pi^3} \int \frac{1}{\kappa^2 - s^2}\ e^{i\boldsymbol{s}\cdot\boldsymbol{r}}\ d^3\boldsymbol{s}\ . \tag{2.62}$$

We can evaluate this integral by choosing a coordinate system with the polar axis along $\boldsymbol{s}$:

$$\begin{aligned} G(\boldsymbol{r}, \omega) &= \frac{1}{8\pi^3} \int_0^{2\pi} \int_0^{\pi} \int_0^{\infty} \frac{e^{isr\cos\theta}}{\kappa^2 - s^2}\ \boldsymbol{s}^2 \sin\theta\ ds\ d\theta\ d\phi \\ &= \frac{1}{4\pi^2} \int_{-1}^{1} \int_0^{\infty} \frac{e^{isru}}{\kappa^2 - s^2}\ s^2 ds\ du \\ &= -\frac{i}{4\pi^2 r} \int_0^{\infty} \frac{s}{\kappa^2 - s^2}(e^{isr} - e^{-isr})\ ds \\ &= \frac{i}{8\pi^2 r} \int_{-\infty}^{\infty} \frac{s}{s^2 - \kappa^2}(e^{isr} - e^{-isr})\ ds\ , \end{aligned} \tag{2.63}$$

where $r = |\boldsymbol{r}|$. The last integral above can be performed using Cauchy's integral formula [21], giving the final result for the Green's function:

$$G(\boldsymbol{r}, \omega) = -\frac{e^{i\kappa r}}{4\pi r}\ . \tag{2.64}$$

The Green's function can be used to solve Eq. 2.54 for any arbitrary source distribution by evaluating the integral in Eq. 2.57. Often, the light source is modeled as an isotropic point source defined by

$$S(\boldsymbol{r},\omega) = A\ \delta^3(\boldsymbol{r})\ , \tag{2.65}$$

where A is the amplitude of a light source that is intensity-modulated at an angular frequency ω. Plugging Eq. 2.65 into Eq. 2.57 and evaluating the result gives the final solution for an isotropic light source in an infinite, homogeneous medium:

$$\begin{aligned}\Phi(\boldsymbol{r},\omega) &= \int \left(-\frac{e^{i\kappa|\boldsymbol{r}-\boldsymbol{r}'|}}{4\pi|\boldsymbol{r}-\boldsymbol{r}'|}\right)\left(-\frac{A\ \delta^3(\boldsymbol{r}')}{D}\right)\ d^3\boldsymbol{r}' \\ &= \frac{A}{4\pi D}\frac{e^{i\kappa r}}{r}\ ,\end{aligned} \tag{2.66}$$

where $r = |\boldsymbol{r}|$ is the distance from the point source. The real and imaginary parts of κ are given by

$$\Re(\kappa) = -\sqrt{\frac{\mu_a}{2D}}\left(-1+\sqrt{1+\frac{\omega^2}{\nu^2\mu_a^2}}\right)^{1/2} \tag{2.67}$$

$$\Im(\kappa) = \sqrt{\frac{\mu_a}{2D}}\left(1+\sqrt{1+\frac{\omega^2}{\nu^2\mu_a^2}}\right)^{1/2}\ , \tag{2.68}$$

which can be used to write expressions for the amplitude and phase:

$$|\Phi(\boldsymbol{r},\omega)| = \frac{A}{4\pi D}\frac{e^{-r\Im(\kappa)}}{r} \tag{2.69}$$

$$\arg(\Phi(\boldsymbol{r},\omega)) = r\Re(\kappa)\ . \tag{2.70}$$

Note that we have chosen the proper root of κ such that $|\Phi(\boldsymbol{r},\omega)|$ goes to zero as r goes to infinity. Also, note that phase is decreasing with distance ($\Re(\kappa) < 0$) as the signal at a position $r \neq 0$ "lags" the intensity-modulated light source; however, much of the literature uses a reversed sign convention for the phase. An illustration of the fluence field in an infinite homogeneous medium is shown in Fig. 2.9.

2.3.4 Semi-Infinite Homogeneous Medium

Near-infared spectroscopic measurements are typically made on the surface of the scalp or skin. Thus, the infinite medium solution is not appropriate for modeling NIRS measurements; however, measurements on the surface of the scalp or skin can be approximated as measurements at the

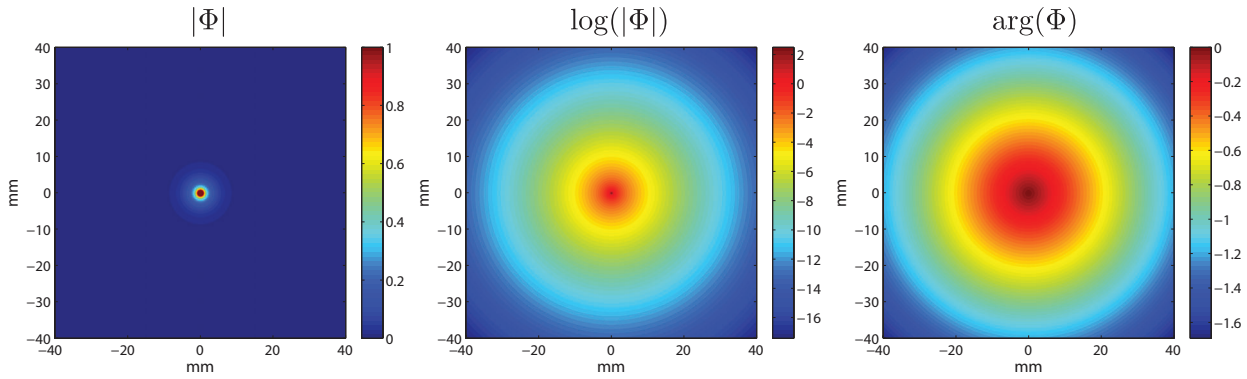

Figure 2.9: Illustration of fluence field for an infinite, homogeneous medium. The intensity is shown on a linear scale (left) and log scale (center), and the phase is also shown (right).

boundary of a semi-infinite, homogeneous medium (i.e., the "slab model"). An analytical solution to diffusion approximation equation in the frequency domain can be derived using the method of images [20], in which the fluence goes to zero at an extrapolated boundary at a distance b above the infinite slab. The position of the extrapolated boundary is determined based on Fresnel reflection giving the following expression according to [20]:

$$b = \left(\frac{1 + R_{eff}}{1 - R_{eff}}\right) \frac{2}{3} \ \ell \tag{2.71}$$

where R_{eff} is the effective reflection coefficient ($\sim$0.4-0.5 for tissue [20]), and ℓ is the mean free path length given by $1/(\mu_s' + \mu_a)$.

A beam of light incident onto the surface of a medium can be approximated as an isotropic point source located one mean free path inside the medium [20]. Thus, a negative source (sink) can be placed $2b + \ell$ above the boundary, causing the fluence to be zero everywhere on the extrapolated boundary due to symmetry. This configuration is illustrated in Fig. 2.10.

The source function is modeled as

$$S(\boldsymbol{r}, \omega) = A \ \delta^3(\boldsymbol{r}_s) - A \ \delta^3(\boldsymbol{r}_i) \ , \tag{2.72}$$

where A gives the amplitude of the light source. The solution for the fluence in a semi-infinite,

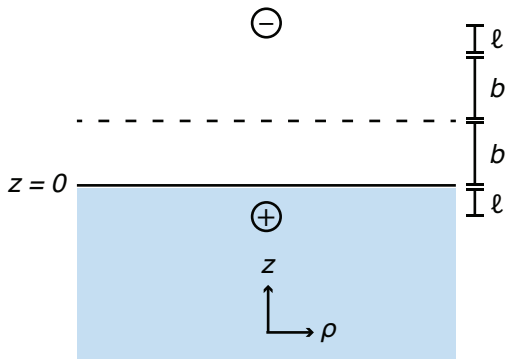

Figure 2.10: Illustration of extrapolated boundary. A sink is placed equidistant from the extrapolated boundary so that fluence is zero everywhere on the boundary due to symmetry.

homogeneous slab is found simply by integrating the source function above with the the Green's function in Eq. 2.64:

$$\Phi(\boldsymbol{r},\omega) = \int \left(-\frac{e^{i\kappa|\boldsymbol{r}-\boldsymbol{r}'|}}{4\pi|\boldsymbol{r}-\boldsymbol{r}'|}\right)\left(-\frac{A\ \delta^3(\boldsymbol{r}'-\boldsymbol{r}_s) - A\ \delta^3(\boldsymbol{r}'-\boldsymbol{r}_i)}{D}\right)\ d^3\boldsymbol{r}'\ , \tag{2.73}$$

This gives the following simple expression for the fluence in a semi-infinite, homogeneous medium:

$$\Phi(\boldsymbol{r},\omega) = \frac{A}{4\pi D}\left(\frac{e^{i\kappa|\boldsymbol{r}-\boldsymbol{r}_s|}}{|\boldsymbol{r}-\boldsymbol{r}_s|} - \frac{e^{i\kappa|\boldsymbol{r}-\boldsymbol{r}_i|}}{|\boldsymbol{r}-\boldsymbol{r}_i|}\right)\ , \tag{2.74}$$

We are typically only interested in the fluence at the boundary, in which the distance to the source and sink can be written as:

$$|\boldsymbol{r}-\boldsymbol{r}_s| = \sqrt{\ell^2+\rho^2} \tag{2.75}$$

$$|\boldsymbol{r}-\boldsymbol{r}_i| = \sqrt{(2b+\ell)^2+\rho^2}\ . \tag{2.76}$$

Substituting the above expressions into Eq. 2.74 gives

$$\Phi(\rho, z=0,\omega) = \frac{A}{4\pi D}\left(\frac{e^{i\kappa\sqrt{\ell^2+\rho^2}}}{\sqrt{\ell^2+\rho^2}} - \frac{e^{i\kappa\sqrt{(2b+\ell)^2+\rho^2}}}{\sqrt{(2b+\ell)^2+\rho^2}}\right)\ . \tag{2.77}$$

We can simply this expression by taking the Taylor expansion of the first term around ℓ and the second term around $2b + \ell$:

$$\Phi(\rho, 0, \omega) = \frac{A}{4\pi D}\left[\left(\frac{e^{i\kappa\rho}}{\rho^3} + \frac{e^{i\kappa\rho}}{\rho^3}\ (1 - i\kappa\rho)\ \ell^2\right) - \left(\frac{e^{i\kappa\rho}}{\rho^3} + \frac{e^{i\kappa\rho}}{\rho^3}\ (1 - i\kappa\rho)\ (2b + \ell)^2\right)\right]\ , \tag{2.78}$$

which simplifies to

$$\Phi(\rho, 0, \omega) = \frac{A}{4\pi D}\frac{e^{i\kappa\rho}}{\rho^3}\ (1 - i\kappa\rho)\ (4b\ell - 4b^2)\ . \tag{2.79}$$

We can write the complex numbers $e^{i\kappa\rho}$ and $1 - i\kappa\rho$ in exponential form in terms of amplitude and phase:

$$e^{i\kappa\rho} = e^{-\Im(\kappa)\rho}e^{i\Re(\kappa)\rho} \tag{2.80}$$

$$1 - i\kappa\rho = [(1 + \Im(\kappa)\rho)^2 + (\Re(\kappa)\rho)^2]^{1/2}\ e^{i\tan^{-1}\left(\frac{\Re(\kappa)\rho}{1+\Im(\kappa)\rho}\right)}\ , \tag{2.81}$$

which allows us to write the following expression for the amplitude and phase of the of the fluence at the surface:

$$|\Phi(\rho, 0, \omega)| = \frac{A}{4\pi D}\frac{e^{-\Im(\kappa)\rho}}{\rho^3}\ [(1 + \Im(\kappa)\rho)^2 + (\Re(\kappa)\rho)^2]^{1/2}(4b\ell - 4b^2) \tag{2.82}$$

$$\arg(\Phi(\rho, 0, \omega)) = \Re(\kappa)\rho\ + \tan^{-1}\left(\frac{\Re(\kappa)\rho}{1 + \Im(\kappa)\rho}\right)\ . \tag{2.83}$$

Light propagation through a semi-infinite, homogeneous slab is illustrated in Fig. 2.11. Rearranging the terms and taking the log of the first expression gives

$$\ln\left(\frac{|\Phi(\rho, 0, \omega)|\rho^3}{[(1 + \Im(\kappa)\rho)^2 + (\Re(\kappa)\rho)^2]^{1/2}}\right) = -\Im(\kappa)\rho + \ln\left(\frac{A}{4\pi D}(4b\ell - 4b^2)\right) \tag{2.84}$$

$$\arg(\Phi(\rho, 0, \omega)) - \tan^{-1}\left(\frac{\Re(\kappa)\rho}{1 + \Im(\kappa)\rho}\right) = \Re(\kappa)\rho\ \ , \tag{2.85}$$

which gives two linear equations in ρ. The slopes of these equations can be determined from experimental measurements and used to recover the absorption and reduced scattering via algebra. Note that the position of the extrapolated boundary ends up in the intercept term, in which the actual value is unimportant for data analysis.

2.3.5 Monte Carlo Methods

With the exception of very simple geometries, such as infinite or semi-infinite media discussed above, deriving analytical expression for light propagation in tissue is generally not feasible. This has led to the development of several numerical methods to solve for light propagation through complex

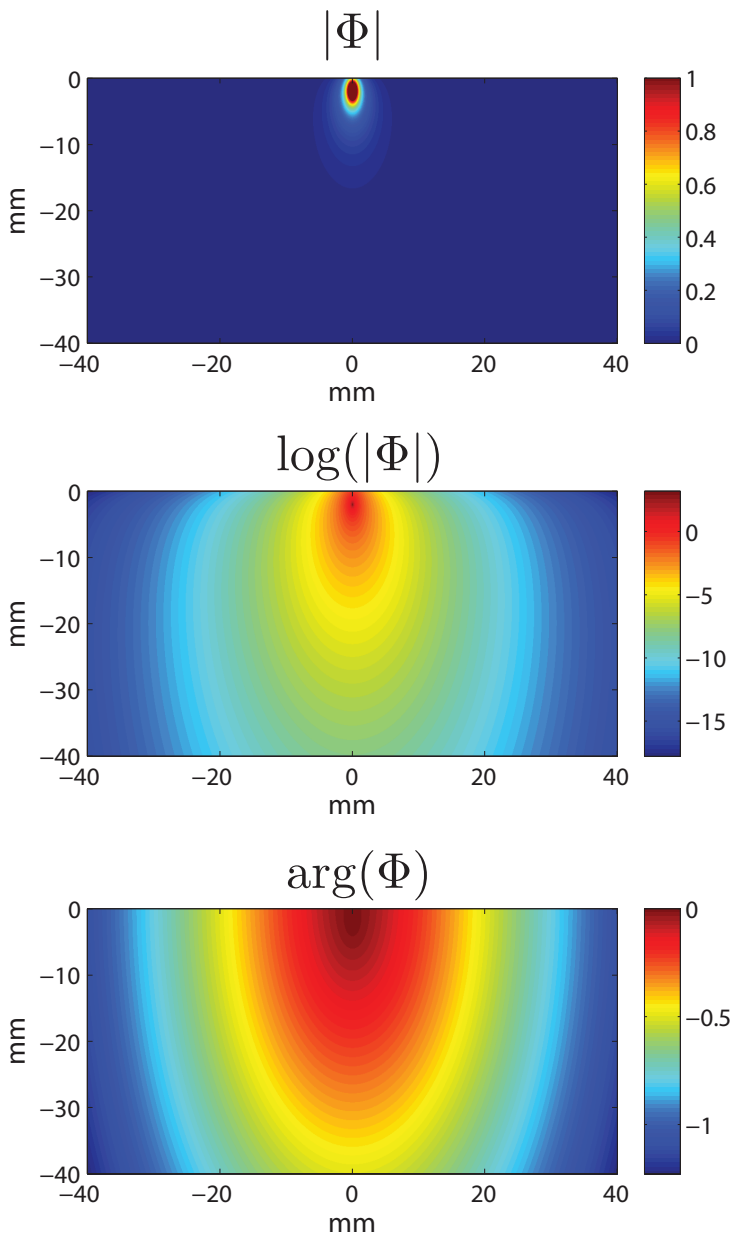

Figure 2.11: Illustration of fluence field for a semi-infinite, homogeneous medium. The intensity is shown on a linear scale (top) and log scale (center), and the phase is also shown (bottom).

heterogeneous media. The two major computation methods that have been used are Monte Carlo simulations and finite element methods (section 2.3.6). Monte Carlo methods are conceptually very simple, in which photon propagation through a volumetric discretization of the medium is simulated directly.

Photon scattering events are simulated as stochastic events using a probabilistic functions. Three random numbers are needed per scattering event: (i) to determine the distance to the next scattering event, (ii) polar scattering angle, and (iii) azimuthal scattering angle. The distance to the next scattering event is given by an exponential distribution parameterized by the scattering coefficient (Eq. 2.4). The polar scattering is often modeled using the Henyey-Greenstein phase function (Eq. 2.5). Lastly, the azimuthal angle is a uniformly distributed number between 0 and 2π. Photon absorption can be treated as a stochastic event; however, photons are typically simulated as "photon packets", in which the weight of the photon is decreased deterministically along the path between scattering events. This improves the convergence and reduces the total number of photons that must be simulated.

Because Monte Carlo methods simulate the physical process of photon propagation, they can solve the RTE without assumptions or approximations. This typically makes Monte Carlo the "gold standard" for comparison and validation other methods. Unfortunately, many photons ($\sim 10^7$) are needed to reach an acceptable level of accuracy, which is very computationally expensive on traditional CPU hardware. A number of researchers have implemented Monte Carlo solvers on GPU hardware [22, 23, 24, 25], which can speed up computations by a factor of more than 300 [25].

2.3.6 Finite Element Methods

Finite element methods (FEM) are another popular method for solving the forward problem [26]. The finite element approach is based on solving the weak form of the diffusion approximation given in Eq. 2.51. In the weak formulation, Eq. 2.51 is multiplied by a suitable "test function" and integrated over the problem domain giving

$$\int_{\Omega} \left[-v(\boldsymbol{r})\ \nabla \cdot \left(D(\boldsymbol{r})\ \nabla \Phi(\boldsymbol{r},\omega) \right) + v(\boldsymbol{r})\ \left(\mu_a(\boldsymbol{r}) + \frac{j\omega}{\nu} \right) \Phi(\boldsymbol{r},\omega) \right] d\Omega = \int_{\Omega} v(\boldsymbol{r})\ S(\boldsymbol{r},\omega)\ d\Omega\ , \tag{2.86}$$

where $v(\boldsymbol{r})$ is an arbitrary test function that also satisfies the boundary conditions. Applying integration by parts to the first term on the left-hand side gives

$$\int_{\Omega} D(\boldsymbol{r})\ \nabla v(\boldsymbol{r}) \cdot \nabla \Phi(\boldsymbol{r},\omega))\ d\Omega + \int_{\partial\Omega} v(\boldsymbol{r})\ D(\boldsymbol{r})\ \nabla \Phi(\boldsymbol{r},\omega)) \cdot \hat{\boldsymbol{n}}\ d(\partial\Omega)$$
$$+ \int_{\Omega} v(\boldsymbol{r}) \left(\mu_a(\boldsymbol{r}) + \frac{j\omega}{\nu}\right) \Phi(\boldsymbol{r},\omega))\ d\Omega = \int_{\Omega} v(\boldsymbol{r})\ S(\boldsymbol{r},\omega)\ d\Omega\ , \tag{2.87}$$

where $\partial\Omega$ indicates an integration over the boundary.

There are several ways to implement boundary conditions, which are explored by Schweiger et. al. [27] including Dirichlet conditions on the boundary, Dirichlet conditions on an extrapolated boundary, and Robin boundary conditions. The Robin boundary condition is given by

$$\Phi(\boldsymbol{r},\omega) + 2D(\boldsymbol{r})A\ \nabla \Phi(\boldsymbol{r},\omega) \cdot \hat{\boldsymbol{n}} = 0 \tag{2.88}$$

where $\hat{\boldsymbol{n}}$ is a unit vector normal to the boundary, and A is a constant. This expression effectively says that the exitance at the boundary is proportional to the fluence on the boundary, adjusted for reflection at the boundary. The constant A is given by

$$A = (1 + R)/(1 - R) \tag{2.89}$$

$$R \approx -1.4399n^{-2} + 0.7099n^{-1} + 0.6681 + 0.0636n\ , \tag{2.90}$$

where n is the refractive index mismatch, and R is from a phenomenological model fit to experimental data [28]. Alternatively, A can be specified by

$$A = \frac{2/(1 - R_0) - 1 + |\cos(\theta_c)|^3}{1 - |\cos(\theta_c)|^2} \tag{2.91}$$

$$R_0 = (n - 1)^2/(n + 1)^2 \tag{2.92}$$

$$\theta_c = \arcsin(1/n)\ , \tag{2.93}$$

which is derived from Fresnel's law in [29]. In either case, rearranging the terms in Eq. 2.88 and substituting into the third term in Eq. 2.87 gives final expression for the global weak form:

$$\int_{\Omega} D(\boldsymbol{r})\ \nabla v(\boldsymbol{r}) \cdot \nabla \Phi(\boldsymbol{r},\omega))\ d\Omega - \int_{\partial\Omega} \frac{1}{2A} v(\boldsymbol{r})\ \Phi(\boldsymbol{r},\omega))\ d(\partial\Omega)$$
$$+ \int_{\Omega} v(\boldsymbol{r}) \left(\mu_a(\boldsymbol{r}) + \frac{j\omega}{\nu}\right) \Phi(\boldsymbol{r},\omega))\ d\Omega = \int_{\Omega} v(\boldsymbol{r})\ S(\boldsymbol{r},\omega)\ d\Omega\ . \tag{2.94}$$

In order to numerically solve the global weak formulation, the tissue volume is discretized into a mesh, given by a set of nodes with very structured connectivity, usually in the form of tetrahedral

units. This allows a function to be determined at any point based on an interpolation defined by a set of basis functions on the enclosing nodes. Thus, the fluence can be expanded in terms of compactly supported basis functions $u_j(\boldsymbol{r})$:

$$\Phi(\boldsymbol{r},\omega) = \sum_j \phi_j \; u_j(\boldsymbol{r}) \; , \tag{2.95}$$

where ϕ_j are the nodal fluence values. Substituting this expression into Eq. 2.94 gives

$$\begin{aligned} \sum_j \Bigg[& \int_\Omega D(\boldsymbol{r}) \; \nabla v(\boldsymbol{r}) \cdot \nabla u_j(\boldsymbol{r}) \; d\Omega \\ & + \int_\Omega v(\boldsymbol{r}) \left(\mu_a(\boldsymbol{r}) + \frac{j\omega}{\nu} \right) u_j(\boldsymbol{r}) \; d\Omega \\ & - \int_{\partial\Omega} \frac{1}{2A} \; v(\boldsymbol{r}) \; u_j(\boldsymbol{r}) \; d(\partial\Omega) \Bigg] \\ & = \int_\Omega v(\boldsymbol{r}) \; S(\boldsymbol{r},\omega) \; d\Omega \; . \end{aligned} \tag{2.96}$$

We can choose the test function $v(\boldsymbol{r})$ from the basis functions giving

$$\begin{aligned} \sum_j \Bigg[& \int_\Omega D(\boldsymbol{r}) \; \nabla u_i(\boldsymbol{r}) \cdot \nabla u_j(\boldsymbol{r}) \; d\Omega \\ & + \int_\Omega u_i(\boldsymbol{r}) \left(\mu_a(\boldsymbol{r}) + \frac{j\omega}{\nu} \right) u_j(\boldsymbol{r}) \; d\Omega \\ & - \int_{\partial\Omega} \frac{1}{2A} \; u_i(\boldsymbol{r}) \; u_j(\boldsymbol{r}) \; d(\partial\Omega) \Bigg] \\ & = \int_\Omega u_i(\boldsymbol{r}) \; S(\boldsymbol{r},\omega) \; d\Omega \; . \end{aligned} \tag{2.97}$$

We can do this for every function $u_j(\boldsymbol{r})$ giving a system of linear equations which can be written in matrix form as

$$(K + B)\phi = s \; , \tag{2.98}$$

where ϕ is a vector containing the nodal fluence values, and the entries of K, B, and s are given by

$$K_{ij} = \int_\Omega D(\boldsymbol{r}) \; \nabla u_i(\boldsymbol{r}) \cdot \nabla u_j(\boldsymbol{r}) \; d\Omega + \int_\Omega u_i(\boldsymbol{r}) \left(\mu_a(\boldsymbol{r}) + \frac{j\omega}{\nu} \right) u_j(\boldsymbol{r}) \; d\Omega \tag{2.99}$$

$$B_{ij} = -\int_{\partial\Omega} \frac{1}{2A} \; u_i(\boldsymbol{r}) \; u_j(\boldsymbol{r}) \; d(\partial\Omega) \tag{2.100}$$

$$s_i = \int_\Omega u_i(\boldsymbol{r}) \; S(\boldsymbol{r},\omega) \; d\Omega \; . \tag{2.101}$$

Because the basis functions have compact support, the matrices K and B are sparse, giving a linear system that can be solved very efficiently using iterative methods, such as biconjugate gradient.

Compared to Monte Carlo methods, the finite element approach is much more computationally efficient. This is true even when comparing to Monte Carlo implementations on GPU hardware, since a full simulation must to be carried out for every source position (and detector position for Jacobian calculations) at each wavelength. For the finite element method, once the matrices K and B are formed (and a factorization of $K+B$ computed for preconditioning), the system can be solved for any arbitrary number of sources (or detectors) with only a minimal increase in computational time.

2.3.7 Nonlinear Inversion

We have examined ways to calculate the forward problem, in which we are interested in finding the fluence as a function of space given optical properties. The more clinically important process involves reversing this procedure. In other words, in the clinic we can make measurement of the light intensity on the scalp and try to estimate the optical properties that generated these measurements (this is called the inverse problem). We have already discussed how to do this with the semi-infinite, homogeneous slab model; however, we may wish to use a more complicated geometry that incorporates anatomical information, such as with a segmented MRI. In this case, the inverse problem is typically solved iteratively, in which we attempt to minimize the sum of squared errors of the residuals:

$$C(\boldsymbol{x}) = \frac{1}{2}(\boldsymbol{y} - f(\boldsymbol{x}))^T \Sigma^{-1} (\boldsymbol{y} - f(\boldsymbol{x})) \ , \tag{2.102}$$

where $\boldsymbol{y}$ is a vector of measurements; Σ^{-1} is the inverse of the covariance matrix of the measurements; and $f(\boldsymbol{x})$ are the predicted measurements by solving the forward problem given a set of parameters in the vector $\boldsymbol{x}$. In the context of NIRS, $\boldsymbol{y}$ may contain measurements from a list of source-detector pairs and $f(\boldsymbol{x})$ is computed using finite element methods using absorption and scattering coefficients as the parameters in $\boldsymbol{x}$. The solution is found by finding a solution where gradient of $C(\boldsymbol{x})$ is zero.

Since f is nonlinear, we take the first two terms of a Taylor expansion around $\boldsymbol{x}$ which gives

$$C(\boldsymbol{x}) = \frac{1}{2}(\boldsymbol{y} - f(\boldsymbol{x}) - J\Delta\boldsymbol{x})^T\Sigma^{-1}(\boldsymbol{y} - f(\boldsymbol{x}) - J\Delta\boldsymbol{x}) \ , \tag{2.103}$$

where J is the Jacobian matrix containing the partial derivatives of f with respect to $\boldsymbol{x}$. Taking the derivative of with respect to $\Delta\boldsymbol{x}$ and setting it to zero gives

$$-J^T\Sigma^{-1}(y - f(\boldsymbol{x}) - J\Delta\boldsymbol{x})^T) = 0 \ , \tag{2.104}$$

Solving this expression for $\Delta\boldsymbol{x}$ gives

$$\Delta\boldsymbol{x} = (J^T\Sigma^{-1}J)^{-1}J^T\Sigma^{-1}(y - f(\boldsymbol{x})) \ , \tag{2.105}$$

which is the update step for an iterative Gauss-Newton method. In many cases, this inversion may be poorly conditioned, and we may wish to add a regularization term to the cost function at each step form of $\lambda\ \Delta\boldsymbol{x}^T\Delta\boldsymbol{x}/2$, in which λ is a regularization parameter. Repeating the derivation gives the update rule

$$\Delta\boldsymbol{x} = (J^T\Sigma^{-1}J + \lambda I)^{-1}J^T\Sigma^{-1}(y - f(\boldsymbol{x})) \ , \tag{2.106}$$

which is the Levenberg-Marquadt update rule [30]. Lastly, we may also consider scaling the magnitude of each parameter by the inverse of the magnitude of $\text{diag}(J^T\Sigma^{-1}J)$, in which we get the final update rule for the Levenberg-Marquadt algorithm:

$$\Delta\boldsymbol{x} = (J^T\Sigma^{-1}J + \lambda\ \text{diag}(J^T\Sigma^{-1}J))^{-1}J^T\Sigma^{-1}(y - f(\boldsymbol{x})) \ . \tag{2.107}$$

In order to perform any type of iterative regression, we need an efficient method to calculate the derivatives. The naive approach would be to perturb the optical properties at every point in our discretized tissue volume and recalculate the fluence. Clearly, this approach is not feasible if the discretization of the tissue volume includes tens to hundreds of thousands of points. In the case of multi-layered models, in which the optical properties are homogeneous within each layer, this procedure may be feasible, but a direct calculation using the adjoint method described below is more efficient.

The quantity we are interested in can be written as

$$y_{s,d} = \int_\Omega \Phi^s(\boldsymbol{r})\ \delta(\boldsymbol{r} - \boldsymbol{r}_d)\ d\Omega \ , \tag{2.108}$$

where $y_{s,d}$ is the fluence at the detector position $\boldsymbol{r}_d$, and $\Phi^s(\boldsymbol{r})$ represents the fluence field from a light source. The key to the adjoint method is simply to consider expressing the delta function above as a point source obeying the diffusion approximation (Eq. 2.51) with its respective fluence

field denoted as $\Phi^d(\boldsymbol{r})$. Under this consideration, we can plug the entirety of the left-hand side of Eq. 2.51 into the integral above to give the expression

$$y_{s,d} = -\int_{\Omega} \Phi^s(\boldsymbol{r}) \left[\nabla \cdot (D\ \nabla\Phi^d(\boldsymbol{r})) + \left(\mu_a + \frac{i\omega}{\nu}\right) \Phi^d(\boldsymbol{r}) \right]\ d\Omega\ . \tag{2.109}$$

Using the integration by parts on the first term gives

$$y_{s,d} = \int_{\Omega} D(\boldsymbol{r})\ \nabla\Phi^s(\boldsymbol{r}) \cdot \nabla\Phi^d(\boldsymbol{r})\ d\Omega + \int_{\Omega} \mu_a(\boldsymbol{r})\ \Phi^s(\boldsymbol{r})\ \Phi^d(\boldsymbol{r})\ d\Omega + ... \tag{2.110}$$

where we have left out the terms that do not depend on $D(\boldsymbol{r})$ or $\mu_a(\boldsymbol{r})$. Remember that substitution of the boundary conditions in section 2.3.6 removed the dependence on $D(\boldsymbol{r})$ from the boundary integral. We can find the functional derivative with respect to absorption by directly evaluating the definition of a functional derivative:

$$\begin{aligned}
\frac{\delta y_{s,d}}{\delta \mu_a(\boldsymbol{r})} &= \lim_{\epsilon \to 0}\ \frac{1}{\epsilon} \left(y_{s,d}\big[\mu_a(\boldsymbol{r}') + \epsilon\ \delta(\boldsymbol{r}' - \boldsymbol{r})\big] - y_{s,d}\big[\mu_a(\boldsymbol{r}')\big] \right) \\
&= \lim_{\epsilon \to 0}\ \frac{1}{\epsilon} \int_{\Omega} \epsilon\ \delta(\boldsymbol{r}' - \boldsymbol{r})\ \Phi^s(\boldsymbol{r}')\ \Phi^d(\boldsymbol{r}')\ d\Omega \\
&= \Phi^s(\boldsymbol{r})\ \Phi^d(\boldsymbol{r})\ .
\end{aligned} \tag{2.111}$$

Performing the exact same procedure for $D(\boldsymbol{r})$ gives

$$\frac{\delta y_{s,d}}{\delta D(\boldsymbol{r})} = \nabla\Phi^s(\boldsymbol{r}) \cdot \nabla\Phi^d(\boldsymbol{r})\ . \tag{2.112}$$

The significance of this result is quite profound in that we can calculate the derivatives with respect to the optical properties everywhere by only performing two forward model calculations. This process is illustrated in Fig. 2.12. For further discussion of this result see [31].

2.4 FUNCTIONAL BRAIN IMAGING

Functional NIRS acquires measurements (usually with a CW system) over time while a subject performs a task or responds to a stimulus. The investigator is interested in relative absorption changes that are related to the task or stimulus. Typically, the investigator uses the stimulus timing to generate a linear model of the evoked hemodynamics. The linear model is then inverted to recover information about the evoked response (e.g., the magnitude of the response). This can be done for each channel and for all subjects. Finally, the subject level statistics are passed to a

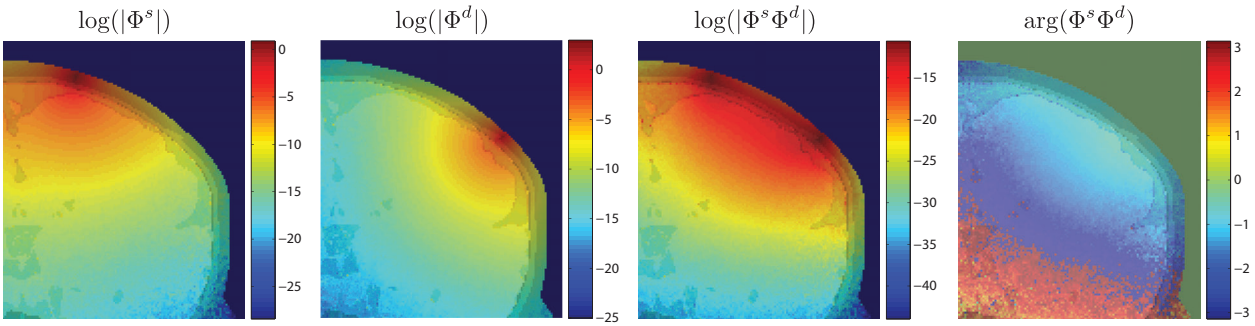

Figure 2.12: Illustration of derivative calculations for absorption based on the adjoint method. The source field (Φ^s) and adjoint field (Φ^s) are shown. The product of the two fields gives the derivative of the source-detector measurement with respect to absorption at every position in the volume.

statistical analysis to make inferences about the population level response. This section reviews the basics of subject level analysis. Group level analyses can differ depending on the experiment, and specific knowledge of group level analyses is not necessary to review the works in chapters 5 and 6, which focus on subject level analysis.

2.4.1 Spectral Estimation of Hemoglobin

The modified Beer-Lambert law [16] is used to model the light intensity for functional imaging:

$$I = I(0)\, \exp\left(-\mathrm{DPF} \cdot d \cdot \sum_j \varepsilon_j c_j + G \right) \ , \tag{2.113}$$

where c_j is the concentration of chromophore j; ε_j is the extinction coefficient relating absorption to chromophore concentration; and d is the source-detector distance. Equation 2.113 can be rewritten in terms of optical density giving

$$\mathrm{OD} = -\ln\left(\frac{I}{I(0)}\right) = \mathrm{DPF} \cdot d \cdot \sum_j \varepsilon_j c_j + G \ . \tag{2.114}$$

For fNIRS, the chromophores of interest are typically oxy-hemoglobin (HbO_2) and deoxy-hemoglobin (Hb).

Brain activity perturbs the chromophore concentration in the cortex because of localized changes in blood flow and oxygen metabolism. Thus, functional studies are typically only interested in changes in chromophore concentration from the baseline:

$$\Delta \mathrm{OD} = -\ln\left(\frac{I}{\langle I \rangle}\right) = \mathrm{DPF} \cdot d \cdot \sum_j \varepsilon_j \Delta c_j \ , \tag{2.115}$$

where $\langle I \rangle$ denotes the mean intensity over time. Because the hemodynamic changes may be focal in nature, an additional correction factor, partial pathlength factor (PPF), is introduced to account for the fraction of optical pathlength that is affected by the evoked activity:

$$\Delta \mathrm{OD} = -\ln\left(\frac{I}{\langle I \rangle}\right) = \mathrm{PPF} \cdot \mathrm{DPF} \cdot d \cdot \sum_j \varepsilon_j \Delta c_j \ . \tag{2.116}$$

The correction factor DPF can be determined with reasonable accuracy given probe geometry, head geometry, and baseline optical properties using numerical simulations; however, accurate calculation of PPF would require *a priori* knowledge of the spatial extent of the hemodynamic activity. This inherently limits the quantification of chromophore changes (see [32] for further discussion). If the ultimate goal of the analysis is calculate t-statistics and no dependence of the optical pathlength on wavelength is modeled, then the actual values of DPF and PPF are irrelevant as they will scale both the numerator and denominator of the t-statistic. In any case, once some assumptions are made about DPF and PPF, the changes in chromophore concentration can be estimated by making measurements at multiple wavelengths:

$$\frac{1}{\mathrm{PPF} \cdot \mathrm{DPF} \cdot d} \ \Delta \mathrm{OD}_i = \sum_j \varepsilon_{ij} \Delta c_j \ , \tag{2.117}$$

where the subscript i denotes the wavelength index and j denotes the chromophore index. Provided there are at least as many wavelengths as chromophores, this gives a system of equations that can easily be solved for chromophore concentrations using matrix algebra.

2.4.2 Generalized Linear Model

Once the fNIRS time-series data has been preprocessed, either by conversion to either optical density for single wavelength of light or ΔHbO_2 and ΔHb in the case of multiple wavelengths, the time-series data can be modeled using a generalized linear model [33]:

$$y = X\beta + \epsilon \tag{2.118}$$

$$\text{E}[\epsilon] = 0 \tag{2.119}$$

$$\text{cov}[\epsilon] = \Sigma \ , \tag{2.120}$$

where X is the design matrix with regressors in each column; β is a vector of model parameters; and ϵ is the error term.

In the context of fNIRS, there are generally two approaches to assembling X: finite impulse response (FIR) models and canonical hemodynamic response function (HRF) models [34]. Finite impulse response models attempt to fit the shape of the evoked hemodynamic response to a set of temporally lagged basis functions at each stimulus onset. Some examples of basis functions that can be used include delta functions, mini box-car functions, gamma functions, or Gaussian functions. Choosing a basis function other than delta functions can impose smoothness on the resulting evoked HRF. Figure 2.13 illustrates some examples of basis functions.

In the case of the canonical HRF model, for each stimulus condition a vector containing values of one during periods of task and zero during rest is convolved with a canonical HRF function to generate the predicted shape of the evoked hemodynamic response. This model makes several assumptions: (i) the hemodynamic response can be modeled as a linear time-invariant process, and (ii) assumptions are made about the shape of impulse response, such as time to onset, time to peak, width (dispersion), etc. The introduction of these assumptions reduces the model to a single regressor per stimulus condition (plus nuisance regressors), which increases statistical power when the canonical model is close to the true model.

Once the model is chosen for the fNIRS time-series, the generalized least squares (GLS) solution [33] is given by

$$\beta = (X^T\Sigma^{-1}X)^{-1}X^T\Sigma^{-1}y \tag{2.121}$$

$$\text{cov}(\beta) = (X^T\Sigma^{-1}X)^{-1} \ . \tag{2.122}$$

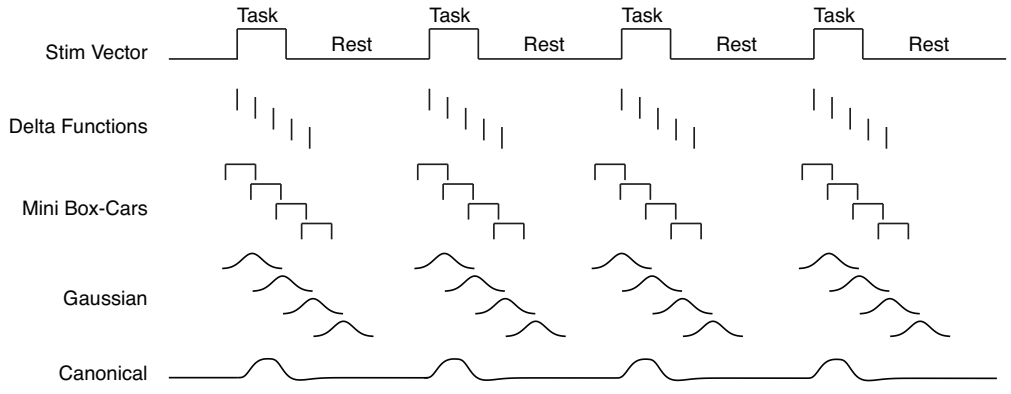

Figure 2.13: Illustration of different basis functions commonly used in the GLM for to fNIRS data.

While the solution is easy to write, implementation is not trivial as the covariance matrix Σ is generally unknown. There are several sources of noise that contribute to the error term in Eq. 2.118 for fNIRS, including instrumentation noise, ambient light, motion artifacts, and systemic physiology. Instrumentation noise is typically dominated by other sources of noise, and ambient light can be controlled through careful experimental conditions or by including an ambient light sensor; however, motion artifacts and systemic physiology, such as Mayer waves (blood pressure), cardiac, and respiratory oscillations, must be carefully accounted for in estimated Eq. 2.118 in order to produce reliable results. Figure 2.14 shows an example power spectrum from fNIRS data. Estimating the GLM in the context of these noise sources is an active area of research, including the developments in chapter 5, which deal with specifically with motion artifacts and systemic physiology.

Once the model is estimated, t-statistics can be estimated for the regressor(s) of interest in order to make statistical inferences about which channels contained evoked brain activity. We can define a contrast vector c, such that $c^T\beta$ gives a linear combination of the regressors. The t-statistic is then given by

$$t = \frac{c^T\beta}{\sqrt{c^T \mathrm{cov}(\beta) c}} \,. \tag{2.123}$$

For example, to test the statistical significance of the first regressor, we would define $c = [1 \;\; 0 \;\; 0 \;\; ...]^T$. If we wanted to test the difference between regressor 1 and regressor 2, we would define $c = [1 \quad -1 \quad 0 \quad ...]^T$.

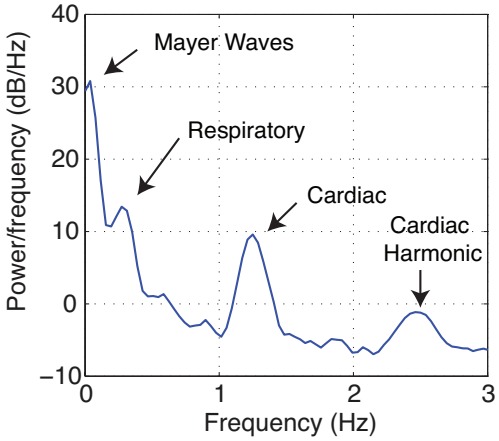

Figure 2.14: Example power spectrum from fNIRS data.

2.4.3 Adaptive Estimation

In some cases, we may wish to perform model estimation recursively, updating the model estimate in real time as new data is acquired. This could be done for a number reasons from simply wanting to give feedback to the investigator as data is acquired to the development of brain machine interfaces. Naively, we could simply update the measurement vector y and regression matrix X and perform the full model estimation procedure; however, current hardware is often not fast enough to perform these calculations at a high sampling rates ($10 - 50+$ Hz in NIRS). Furthermore, as the y and X grow, the computational requirements for inversion continues to grow.

The linear Kalman filtering algorithm is an efficient way to recursively update model estimates using the previous model estimate and the new data only. The model that the Kalman filter solves is given by

Model

$$\beta\{t\} = A\{t\}\beta\{t-1\} + B\{t\}u\{t\} + q\{t\} \tag{2.124}$$

$$q\{t\} \sim N(0, Q\{t\}) \tag{2.125}$$

$$y\{t\} = X\{t\}\beta\{t\} + r\{t\} \tag{2.126}$$

$$r\{t\} \sim N(0, R\{t\}) \ , \tag{2.127}$$

where $\beta\{t\}$ describes the "state" of the system; $A\{t\}$ is the state transition matrix; $B\{t\}$ is the

control input matrix; $u\{t\}$ is the control input vector; $q\{t\}$ is the process noise with covariance $Q\{t\}$; $y\{t\}$ contains observed measurements; $X\{t\}$ is the observation matrix; $r\{t\}$ is the measurement noise with covariance $R\{t\}$. The quantities $A\{t\}$, $B\{t\}$, $u\{t\}$, $X\{t\}$, and $y\{t\}$ are known quantities, while $\beta\{t\}$ is estimated. In many cases, such as the methods developed in chapter 6, $A\{t\}$, is an identity matrix, and $B\{t\}$ and $u\{t\}$ are discarded (set to zero). In this case, we have essentially have a linear model with time-varying coefficients when $Q\{t\}$ is non-zero.

The estimation procedure for the linear Kalman filter is given by the following equations:

Prediction Step

$$\hat{\beta}\{t|t-1\} = A\{t\}\hat{\beta}\{t-1|t-1\} + B\{t\}u\{t\} \tag{2.128}$$

$$C\{t|t-1\} = C\{t-1|t-1\} + Q\{t\} \tag{2.129}$$

Prediction Error

$$\hat{r}\{t\} = y\{t\} - X\{t\}\hat{\beta}\{t|t-1\} \tag{2.130}$$

Update Step

$$S = X\{t\}C\{t|t-1\}X^T\{t\} + R\{t\} \tag{2.131}$$

$$K = C\{t|t-1\}X^T\{t\}S^{-1} \tag{2.132}$$

$$C\{t|t\} = C\{t|t-1\} - KX\{t\}C\{t|t-1\} \tag{2.133}$$

$$\hat{\beta}\{t|t\} = \hat{\beta}\{t|t-1\} + K\hat{r}\{t\} \ , \tag{2.134}$$

where C is the covariance matrix of β. Here, the notation $\{m|n\}$ denotes the quantity at time m given the measurements up to time n. The process noise covariance $Q\{t\}$ is generally set *a priori*.

Given the previous estimate of β, we can simply take the expectation to predict the next value of β:

$$\begin{aligned}\hat{\beta}\{t|t-1\} &= \mathrm{E}[\beta\{t\}|\hat{\beta}\{t-1|t-1\}] \\ &= A\{t\}\hat{\beta}\{t-1|t-1\} + B\{t\}u\{t\} \ ,\end{aligned} \tag{2.135}$$

where we have used the fact that $q\{t\}$ is mean zero. Using the properties of covariance, we can estimate the covariance matrix of our predicted β:

$$\begin{aligned} C\{t|t-1\} &= \text{cov}(\beta\{t\} - \hat{\beta}\{t|t-1\}) \\ &= \text{cov}(\beta\{t\}) + \text{cov}(A\{t\}\hat{\beta}\{t|t-1\}) \\ &= Q\{t\} + A\{t\}C\{t-1|t-1\}A^T\{t\} \ . \end{aligned} \tag{2.136}$$

The prediction error is simply given by

$$\hat{r}\{t\} = y\{t\} - X\{t\}\hat{\beta}\{t|t-1\} \ . \tag{2.137}$$

Again, we can simply use the properties of covariance to derive an expression for the covariance of the prediction error:

$$\begin{aligned} S &= \text{cov}(\hat{r}\{t\}) \\ &= \text{cov}(y\{t\}) + \text{cov}(X\{t\}\hat{\beta}\{t|t-1\}) \\ &= R\{t\} + X\{t\}C\{t|t-1\}X^T\{t\} \ . \end{aligned} \tag{2.138}$$

We will assume an update of model states given by

$$\hat{\beta}\{t|t\} = \hat{\beta}\{t|t-1\} + K\hat{r}\{t\} \ , \tag{2.139}$$

where K is referred to as the Kalman gain. The Kalman filter minimizes the mean squared error (MSE) given by

$$\text{MSE} = ||\beta\{t\} - \hat{\beta}\{t|t-1\}||^2 = \text{tr}(C\{t|t\}) \ , \tag{2.140}$$

where the MSE is simply the sum of the diagonal elements of the covariance matrix (trace). The covariance can be expanded as

$$\begin{aligned} C\{t|t\} &= \text{cov}\left(\beta\{t\} - \hat{\beta}\{t|t\}\right) \\ &= \text{cov}\left(\beta\{t\} - \hat{\beta}\{t|t-1\} - K\hat{r}\{t\}\right) \\ &= \text{cov}\left(\beta\{t\} - \hat{\beta}\{t|t-1\} - K(y\{t\} - X\{t\}\hat{\beta}\{t|t-1\})\right) \\ &= \text{cov}\left(\beta\{t\} - \hat{\beta}\{t|t-1\} - K(X\{t\}\beta\{t\} + r\{t\} - X\{t\}\hat{\beta}\{t|t-1\})\right) \ . \end{aligned} \tag{2.141}$$

Collecting the terms and using the properties of covariance gives

$$\begin{aligned} C\{t|t\} &= \text{cov}\left((I - KX\{t\})(\beta\{t\} - \hat{\beta}\{t|t-1\}) - Kr\{t\}\right) \\ &= (I - KX\{t\})C\{t|t-1\}(I - KX\{t\})^T + KR\{t\}K^T \ , \end{aligned} \tag{2.142}$$

which gives an update rule for the covariance given an arbitrary Kalman gain. This result can be expanded to

$$\begin{aligned} C\{t|t\} &= C\{t|t-1\} - C\{t|t-1\}X^T\{t\}K^T - KX\{t\}C\{t|t-1\} \\ &\quad + KX\{t\}C\{t|t-1\}X^T\{t\}K^T + KR\{t\}K^T \\ &= C\{t|t-1\} - C\{t|t-1\}X^T\{t\}K^T - KX\{t\}C\{t|t-1\} \\ &\quad + K(X\{t\}C\{t|t-1\}X^T\{t\} + R\{t\})K^T \\ &= C\{t|t-1\} - C\{t|t-1\}X^T\{t\}K^T - KX\{t\}C\{t|t-1\} + KSK^T \ . \end{aligned} \tag{2.143}$$

Finally, we can take the derivative with respect to K and set it to zero to find the optimal Kalman gain:

$$\frac{\partial}{\partial K}\mathrm{tr}(C\{t|t\}) = -2C\{t|t-1\}X^T\{t\} + 2KS = 0 \ , \tag{2.144}$$

which has the solution

$$K = C\{t|t-1\}X^T\{t\}S^{-1} \ . \tag{2.145}$$

From the above, it is easy to see that $KSK^T = C\{t|t-1\}X^T\{t\}K^T$, which cancels the last two terms in Eq. 2.142, giving the simplified update rule for covariance:

$$C\{t|t\} = C\{t|t-1\} - C\{t|t-1\}X^T\{t\}K^T \ . \tag{2.146}$$

Note that Eq. 2.127 assumes that the prediction error is independent of the previous time points. In the previous section we discussed the sources of noise in NIRS and showed that this assumption is clearly not true. Chapter 6 modifies this procedure to account for the sources of noise in NIRS.

3.0 ASSESSMENT OF SEMI-INFINITE HOMOGENEOUS SLAB MODEL FOR BASELINE PHYSIOLOGY ESTIMATION IN NEONATES

The semi-infinite, homogeneous slab model is commonly used for analysis of FD-NIRS data due to its ease of implementation and the availability of an analytic solution to the diffusion approximation. This chapter attempts to thoroughly investigate the accuracy of these estimates in neonates. The work presented in this chapter has been published in Biomedical Optics Express [35], and is available online at http://www.opticsinfobase.org/boe/abstract.cfm?uri=boe-5-12-4300 (©2014 Optical Society of America).

3.1 ABSTRACT

Frequency domain near-infrared spectroscopy (FD-NIRS) is a non-invasive method for measuring optical absorption in the brain. Common data analysis procedures for FD-NIRS data assume the head is a semi-infinite, homogeneous medium. This assumption introduces bias in estimates of absorption (μ_a), scattering (μ_s'), tissue oxygen saturation (S_tO_2), and total hemoglobin (HbT). Previous works have investigated the accuracy of recovered μ_a values under this assumption. The purpose of this study was to examine the accuracy of recovered S_tO_2 and HbT values in FD-NIRS measurements of the neonatal brain. We used Monte Carlo methods to compute light propagation through a neonate head model in order to simulate FD-NIRS measurements at 690 nm and 830 nm. We recovered μ_a, μ_s', S_tO_2, and HbT using common analysis procedures that assume a semi-infinite, homogeneous medium and compared the recovered values to simulated values. Additionally, we characterized the effects of curvature via simulations on homogeneous spheres of varying radius. Lastly, we investigated the effects of varying amounts of extra-axial fluid. Curvature induced underestimation of μ_a, μ_s', and HbT, but had minimal effects on S_tO_2. For the morphologically

normal neonate head model, the mean absolute percent errors (MAPE) of recovered μ_a values were 12% and 7% for 690 nm and 830 nm, respectively, when source-detector separation was at least 20 mm. The MAPE for recovered S_tO_2 and HbT were 6% and 9%, respectively. Larger relative errors were observed (∼20-30%), especially as S_tO_2 and HbT deviated from normal values. Excess CSF around the brain caused very large errors in μ_a, μ_s', and HbT, but had little effect on S_tO_2.

3.2 INTRODUCTION

Near-infrared spectroscopy (NIRS) is a non-invasive method for measuring the optical absorption of cerebral blood due to hemoglobin [36]. Measurements acquired at multiple wavelengths of light can be used for spectral estimation of both oxy-hemoglobin (HbO_2) and deoxy-hemoglobin (Hb), which subsequently provide estimates of tissue oxygen saturation (S_tO_2) and total hemoglobin (HbT). Because NIRS is portable, non-ionizing, and non-restraining, it is an attractive technique for bedside measurements of cerebral physiology in neonates with applications in assessing brain development [37], detecting hypoxic-ischemic brain injuries [3, 4], and monitoring during pediatric cardiac surgery [2].

Current clinical NIRS systems use continuous wave (CW-) light sources, in which light intensity is constant. These systems have shown promising evidence in monitoring trends in cerebral physiology, but lack quantitative accuracy in absolute estimates of baseline physiology [38]. Frequency domain (FD-) NIRS systems use a light source that is modulated in intensity by a sinusoidal function, which provides measurements of both amplitude and phase of the modulated light. The phase measurement contains information about the optical pathlength, which improves quantification.

A common method for analysis of FD-NIRS data assumes a homogeneous, semi-infinite medium [39]. The existence of an analytical solution to light propagating in such a medium provides a convenient and computationally efficient method for data analysis, but introduces bias in recovered absorption values due to curvature/finite volume and the heterogeneous structure of tissues in the head. Dehaes et. al. investigated the accuracy of recovered optical absorption coefficients using this model by simulating FD-NIRS measurements on one-, two-, and three-layered segmentations of structural magnetic resonance images (MRI) and comparing recovered absorption coefficients to simulated values [40]. They found typical errors of 8-24% in recovered absorption coefficients in

neonates. Based on the errors in absorption, they predicted errors of 8% and 11% in S_tO_2 and HbT, respectively.

In this work, we used simulations of light propagation through tissue to directly investigate the accuracy of S_tO_2 and HbT estimates in neonates. We used a four-layer segmentation of a structural MRI from a full term, 24 day old neonate to simulate FD-NIRS measurements. We used literature values for the scalp, skull, and cerebrospinal fluid (CSF) and parameterized the brain properties in terms of S_tO_2 and HbT. Simulations were performed for varying S_tO_2 (30-100%) and HbT (15-120 μM) in the brain layer. Recovered S_tO_2, HbT, μ_a, and μ_s' values were compared to the simulated values. Additionally, we characterized the effects of curvature on recovered values via simulations on homogeneous spheres of varying radius (30-120 mm). Lastly, we examined the effects of extra-axial fluid increasing the thickness of the CSF layer.

3.3 METHODS

3.3.1 Simulation of measurements

Simulated NIRS measurements were obtained by computing light propagation through volumetric images via the Monte Carlo Extreme software (MCXLAB 0.7.9 [25]). The volumetric images contained tissue labels, specifying the optical properties compiled in Table 3.1. Simulations were performed using reduced scattering coefficients with anisotropy factor set to zero (isotropic scattering). For all simulations, wavelengths of 690 nm and 830 nm were used according to the findings in [32]. The optical properties of the brain were calculated based on tissue oxygen saturation (S_tO_2) and total hemoglobin (HbT) content. Normal baseline values of 70% S_tO_2 and 60 μM HbT were assumed for the brain. Additionally, background absorption from 70% water content was assumed for the brain voxels. The time-domain signal output from MCXLAB was converted to a frequency-domain measurement via discrete Fourier transform at a modulation frequencies of 50 MHz, 100 MHz, 150 MHz, and 200 MHz.

3.3.2 Calibration

The simulated FD-NIRS data were calibrated in the same manner as the calibration procedure for experimental data (e.g., [45]) by simulating an additional calibration data set on a homogeneous

Table 3.1: Optical properties of tissues; RI = refractive index.

	$\mu_{a,690}$ (mm^{-1})	$\mu_{a,830}$ (mm^{-1})	$\mu'_{s,690}$ (mm^{-1})	$\mu'_{s,830}$ (mm^{-1})	RI
Skin/Scalp	0.0206[a]	0.0122[a]	2.37[a]	1.81[a]	1.45[b]
Skull	0.0255[c]	0.0252[c]	2.35[c]	1.75[c]	1.45[b]
CSF	0.0004[d]	0.0026[d]	0.01[d]	0.01[d]	1.33[b]
Brain	0.0039-0.0285[f]	0.0051-0.0256[f]	1.44[b]	1.07[b]	1.45[b]

[a][41]; [b][14]; [c][42]; [d][32]; [f]Based on spectra from [43, 44]

slab of 180 mm × 180 mm × 100 mm with optical properties matching the brain at 70% S_tO_2 and 60 μM HbT. The respective calibration terms for intensity and phase are calculated as

$$c_\psi = \psi_{theo}/\psi_{slab} \tag{3.1a}$$

$$c_\Phi = \Phi_{theo} - \Phi_{slab} \ , \tag{3.1b}$$

where ψ_{theo} and Φ_{theo} are the theoretical intensity and phase values, and ψ_{slab} and Φ_{slab} are the intensity and phase measured on the calibration slab. The calibrated data is then given by

$$\psi_{cal} = c_\psi \ \psi \tag{3.2a}$$

$$\Phi_{cal} = \Phi + c_\Phi \ , \tag{3.2b}$$

where ψ_{cal} and Φ_{cal} are the calibrated intensity and phase values, and ψ and Φ are the measured intensity and phase values. The calibration procedure reduces errors due to the diffusion approximation, especially at short source-detector separation distances [40].

3.3.3 Recovery of optical properties and physiological parameters

The solution to light propagation through a semi-infinite, homogeneous medium is described in detail by Fantini et. al. [39]. The exact equations used in this work were as follows:

$$\ln\left(\frac{\psi\ \rho^3}{\left[1+\rho\left(\frac{2\mu_a}{D}\right)^{1/2}V^+ + \rho^2\frac{\mu_a}{D}\left(1+\left(\frac{\omega}{\nu\mu_a}\right)^2\right)^{1/2}\right]^{1/2}}\right) = -\rho\left(\frac{\mu_a}{2D}\right)^{1/2}V^+ + F_\psi \tag{3.3a}$$

$$\Phi + \arctan\left[\frac{\rho\left(\frac{\mu_a}{2D}\right)^{1/2}V^-}{1+\rho\left(\frac{\mu_a}{2D}\right)^{1/2}V^+}\right] = \rho\left(\frac{\mu_a}{2D}\right)^{1/2}V^- + \Phi_0\ , \tag{3.3b}$$

where ψ and Φ are the amplitude and phase measurements with angular modulation frequency of ω; ρ is the source-detector separation; μ_a is the absorption coefficient; D is the diffusion constant equal to $1/(3\mu_a+3\mu_s')$, in which μ_s' is the reduced scattering coefficient; ν is the speed of light in the media; F_ψ is a complicated function of many variables, including ρ, μ_a, and D that is approximately constant; Φ_0 is the instrument phase offset. The terms V^+ and V^- are given by

$$V^+ = \left[\left(1+\left(\frac{\omega}{\nu\mu_a}\right)^2\right)^{1/2} + 1\right]^{1/2} \tag{3.4a}$$

$$V^- = \left[\left(1+\left(\frac{\omega}{\nu\mu_a}\right)^2\right)^{1/2} - 1\right]^{1/2}\ . \tag{3.4b}$$

Note that Eq. 3.3 is an approximation of the full solution in [39]. This is often further approximated to the following equations:

$$\ln\left(\psi\ \rho^2\right) = -\rho\left(\frac{\mu_a}{2D}\right)^{1/2}V^+ + F_\psi \tag{3.5a}$$

$$\Phi = \rho\left(\frac{\mu_a}{2D}\right)^{1/2}V^- + F_\Phi\ . \tag{3.5b}$$

where F_Φ replaces the additional terms in Eq. 3.3(b), and is assumed to be constant. We chose to use Eq. 3.3 for estimation of optical properties for this work, since we found Eq. 3.3 to produce more accurate results with uncalibrated data from simulations on a homogeneous slab than Eq. 3.5. With either set of equations, the left-hand side quantities form a linear relationship with ρ with the following slope values:

$$\alpha = -\left(\frac{\mu_a}{2D}\right)^{1/2}V^+ \tag{3.6a}$$

$$\varphi = \left(\frac{\mu_a}{2D}\right)^{1/2}V^-\ , \tag{3.6b}$$

for the equations for ψ and Φ, respectively. The optical absorption and scattering coefficients are solved for algebraically in terms of the slope values:

$$\mu_a = \frac{\omega}{2\nu}\left(\frac{\varphi}{\alpha} - \frac{\alpha}{\varphi}\right) \tag{3.7a}$$

$$\mu_s' = \frac{\alpha^2 - \varphi^2}{3\mu_a} - \mu_a \ , \tag{3.7b}$$

Note that in the continuous wave case ($\omega = 0$), Φ is a constant and solving for μ_a and μ_s' is no longer possible.

The regression of Eqs. 3.5(a) and 3.5(b) is straightforward. The regression of Eq. 3.3(a) and 3.3(b) is performed iteratively, starting with an initial estimate of μ_a and μ_s' from regression of Eq. 3.5. The optical absorption coefficients recovered from Eq. 3.7(a) above are related to hemoglobin by

$$\mu_{a,\lambda} = \epsilon_{\mathrm{HbO_2},\lambda}[\mathrm{HbO_2}] + \epsilon_{\mathrm{Hb},\lambda}[\mathrm{Hb}] + B(\lambda) \ . \tag{3.8}$$

where the $[\mathrm{HbO_2}]$ and $[\mathrm{Hb}]$ are the tissue concentrations of oxy-hemoglobin and deoxy-hemoglobin, respectively; $\epsilon_{\mathrm{HbO_2},\lambda}$ and $\epsilon_{\mathrm{Hb},\lambda}$ are the respective extinction coefficients for $\mathrm{HbO_2}$ and Hb at a wavelength of λ; $B(\lambda)$ is the background absorption at the wavelength λ. In this study, background absorption was assumed to be from 70% water content, in which $B(\lambda)$ was set to 70% of the absorption coefficient of water (absorption spectrum from [44]). With two or more wavelengths, Eq. 3.8 can be used to form a system of linear equations, which can be organized in matrix notation as

$$\begin{matrix} u \\ \\ \end{matrix} \quad \begin{matrix} \\ \\ \end{matrix} \quad \begin{matrix} E \\ \\ \end{matrix} \quad \begin{matrix} h \\ \\ \end{matrix}$$

$$\begin{bmatrix} \mu_{a,\lambda_1} - B(\lambda_1) \\ \mu_{a,\lambda_2} - B(\lambda_2) \\ \vdots \\ \mu_{a,\lambda_n} - B(\lambda_n) \end{bmatrix} = \begin{bmatrix} \epsilon_{\mathrm{HbO_2},\lambda_1} & \epsilon_{\mathrm{Hb},\lambda_1} \\ \epsilon_{\mathrm{HbO_2},\lambda_2} & \epsilon_{\mathrm{Hb},\lambda_2} \\ \vdots & \vdots \\ \epsilon_{\mathrm{HbO_2},\lambda_n} & \epsilon_{\mathrm{Hb},\lambda_n} \end{bmatrix} \begin{bmatrix} [\mathrm{HbO_2}] \\ [\mathrm{Hb}] \end{bmatrix} \ , \tag{3.9}$$

where u is the vector containing the absorption coefficients, corrected for background absorption; E is the matrix gathering the extinction coefficients; h is the vector containing oxy- and deoxy-hemoglobin concentrations. The least-squares solution to the matrix expression is given by

$$h = (E^T E)^{-1} E^T u \ , \tag{3.10}$$

where the superscript T is the transpose operation. The estimated values for [HbO_2] and [Hb] can be used to calculate S_tO_2 and HbT as follows:

$$[\text{HbT}] = [\text{HbO}_2] + [\text{Hb}] \tag{3.11a}$$

$$S_tO_2 = [\text{HbO}_2]/[\text{HbT}] \times 100\% \ , \tag{3.11b}$$

Equations 3.10 and 3.11 give some insight into the propagation of errors from recovered μ_a values to S_tO_2 and HbT. In the limit that background absorption goes to zero ($B(\lambda) = 0$), we find that [HbO_2] and [Hb] are linear combinations of the recovered μ_a values with coefficients from the matrix given by $(E^TE)^{-1}E^T$. From Eq. 3.11, we can conclude that HbT is also a linear combination of recovered μ_a values, and S_tO_2 is a ratio with linear combinations of μ_a values in the numerator and denominator. Thus, scaling all μ_a values by a factor, c, will scale HbT by c, but have no effect on S_tO_2 (when $B(\lambda) = 0$). We can use this fact to conclude that if relative errors in μ_a are similar across wavelengths, the errors in HbT will be sensitive to the magnitude errors in μ_a, but errors in S_tO_2 will be minimal; however, in the case that the relative errors in μ_a are dissimilar across wavelengths, the errors in S_tO_2 can be large or unpredictable.

3.3.4 Effects of curvature

In order to examine the effects of head curvature on estimates of S_tO_2 and HbT, data were simulated on homogeneous spheres of varying radius from 30-120 mm, as well as a flat slab (infinite radius) with dimensions of 180 mm × 180 mm × 100 mm. All voxels within the sphere or slab were labeled with optical properties matching the brain at 70% S_tO_2 and 60 μM HbT. The volumetric images defining the optical properties were all created with 1 mm isotropic resolution. A single source position was simulated with detectors arranged in a linear fashion along the surface at distances from 10-40 mm in 1 mm increments. In order to decrease the effects of discretization of the spherical geometry, the position and orientation of the probe were randomized for each iteration. A total of 128 repetitions of 10^7 photon packets were simulated per wavelength for each simulation. Recovery of S_tO_2 and HbT was performed for four subsets of the measurements based on source-detector separation: 10-25 mm, 15-30 mm, 20-35 mm, and 25-40 mm. Recovery of μ_a, μ_s', S_tO_2, and HbT was performed via the methods in Section 3.3.3 and compared to the simulated values.

3.3.5 Simulations of varying S_tO_2 and HbT in the brain

In order to investigate the magnitude of errors in a realistic model of an infant head with normal morphology, simulations were performed on a segmented structural MRI of a neonate (full term, 24 days old). Segmentation of gray matter, white matter, and CSF was performed via SPM8 (Wellcome Trust Centre for Neuroimaging, London, UK) using the UNC neonate atlas [46]. Segmentation of the scalp and skull layers was performed via manually thresholding the structural image after masking out the brain. A sample of the segmentation results is shown in Fig. 3.1(a). The segmented volume had a 1 mm isotropic resolution. A single source position was simulated. Detector locations were chosen as random points on the surface of the head with uniformly distributed distances between 10-40 mm. The source and detector locations are shown in Fig. 3.1(b).

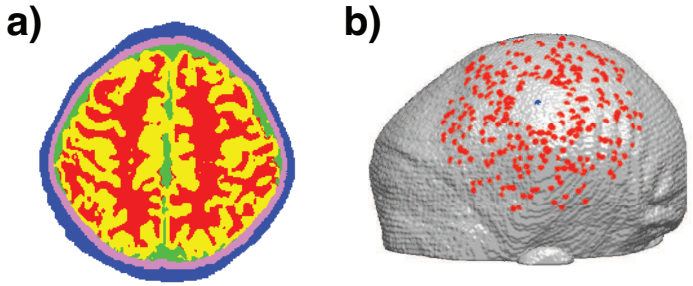

Figure 3.1: (a) Sample segmentation results. The layers from outer to inner are scalp (blue), skull (purple), cerebrospinal fluid (green), gray matter (yellow), and white matter (red). (b) The optical probe used to simulate data. The blue dot in the center was the source position, while the red dots were detector positions.

Optical properties of the skin/scalp, skull, and CSF layers were fixed according to Table 3.1 for all simulations. The white and gray matter regions were combined to a single brain region with optical properties based on S_tO_2 and HbT. Simulations were performed with varying S_tO_2 (30-100%) with fixed HbT (60 μM). A second set of simulations were performed with varying HbT (15-120 μM) with fixed S_tO_2 (70%). A total of 128 repetitions of 10^7 photon packets were simulated per wavelength for each simulation. Recovery of μ_a, μ_s', S_tO_2, and HbT was performed via the methods in Section 3.3.3 for four subsets of the measurements according to source-detector separation: 10-25 mm, 15-30 mm, 20-35 mm, and 25-40 mm. Recovered values were compared with simulated values for the brain.

3.3.6 Effects of increased extra-axial fluid

In order to simulate the effects of extra-axial fluid, we increased the thickness of the CSF layer by performing a binary erosion of the brain mask with varying sized kernels and replacing the outer brain voxels with CSF in the resulting segmented volumes. This is in-effect similar to the actual morphological changes associated with extra-axial fluid, in which the build up of excess CSF in the subarachnoid space pushes the brain away from the the skull. The resulting segmentations had CSF layers that varied in thickness from approximately 1 mm to 4 mm with some spatial heterogeneity due to anatomy. The probe shown in Fig. 3.1(b) was used for simulation as in the previous section. Simulations were performed for varying S_tO_2 (30-90%) with fixed HbT (60 μM). Recovery of μ_a, μ_s', S_tO_2, and HbT was performed via the methods in Section 3.3.3 for four subsets of the measurements according to source-detector separation: 10-25 mm, 15-30 mm, 20-35 mm, and 25-40 mm.

3.4 RESULTS

3.4.1 Simulations on homogeneous spheres

Figure 3.2 shows the results of simulating data on homogeneous spheres and recovering μ_a (top row) and μ_s' (bottom row) via the methods in Section 3.3.3. In all cases, curvature induced underestimation of μ_a and μ_s' with more severe effects as radius of curvature decreased. There were no strong trends between the magnitude of errors and source-detector separation distance. Errors in μ_s' were more severe than errors in μ_a. Figure 3.3 shows the results from calculating S_tO_2 and HbT from the recovered μ_a values in Fig. 3.2(a)-3.2(d). In general, curvature had little effect on S_tO_2, but caused significant underestimation of HbT. There were no strong trends across source-detector distance for errors in HbT. The average circumference of the neonatal head was reported to be 343 mm [47], giving an approximate radius of curvature of 55 mm using a circular approximation. At a radius of curvature of 60 mm, the percent errors were 5-7%, 6-7%, 7-8%, and less than 1.5% for $\mu_{a,690}$, $\mu_{a,830}$, HbT, and S_tO_2, respectively.

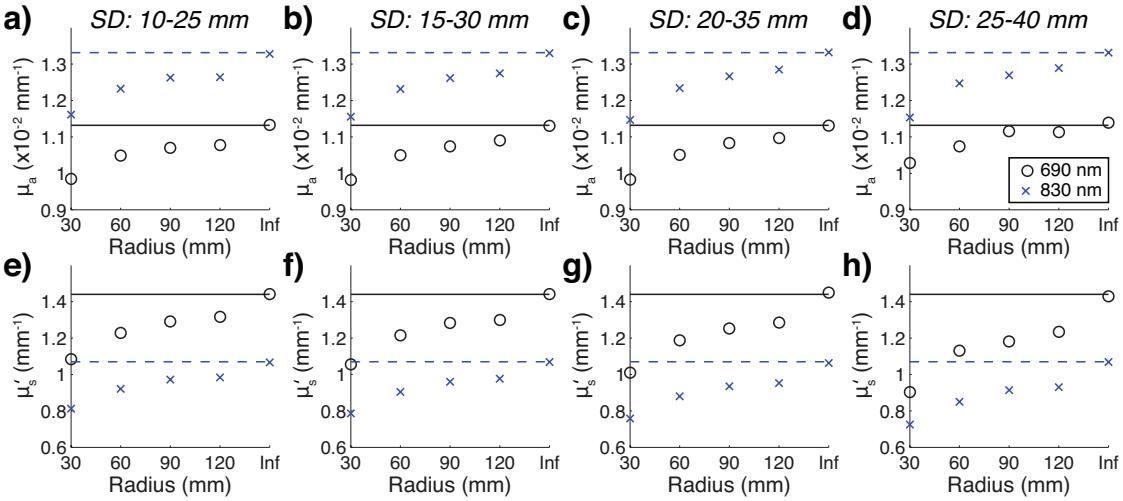

Figure 3.2: Recovered absorption (a-d) and scattering (e-h) coefficients for data simulated on homogeneous spheres of varying radius. The solid and dashed lines show the simulated values for 690 nm and 830 nm, respectively. Source-detector separation increases with each column from left to right. Modulation frequency was 100 MHz.

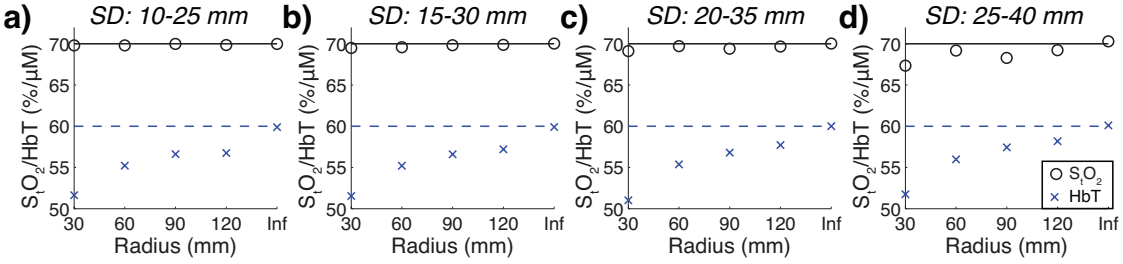

Figure 3.3: Recovered S_tO_2 (O's) and HbT (X's) values for data simulated on homogeneous spheres of varying radius. The solid and dashed lines show the simulated values for S_tO_2 and HbT, respectively. Source-detector separation increases with each column from left to right. Modulation frequency was 100 MHz.

3.4.2 Normalized partial pathlength

Figure 3.4 shows the normalized partial pathlength (i.e., fraction of the total pathlength) of the simulated photons through each tissue type in the neonate model as a function of source-detector distance. The data shown was for 70% S_tO_2 and 60 μM HbT in the brain. Each point on the graph represents one of the source-detector measurements. In general, the fraction through the brain increased as a function of source-detector distance, while the fraction through the scalp and skull decreased with source-detector distance. There appeared to be a split between increasing and decreasing trends in the partial pathlength through CSF with source-detector separation, potentially due to anatomical variations in CSF across the head. Overall, the results in Fig. 3.4 suggest that longer source-distances will be more sensitive to the brain and less sensitive to superficial layers.

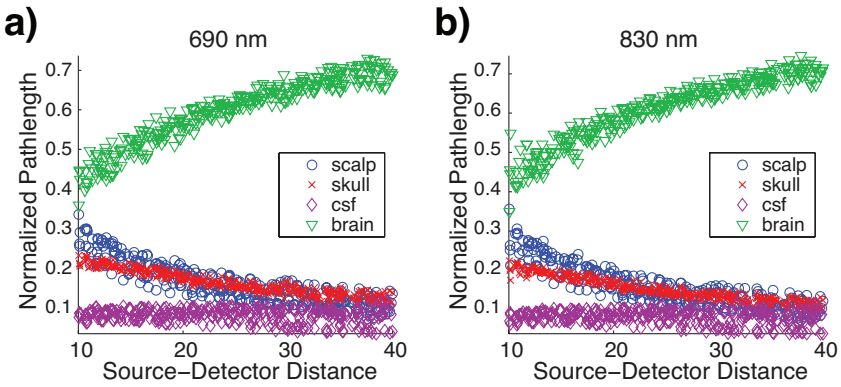

Figure 3.4: Normalized partial pathlength of light through a neonate head model with 70% S_tO_2 and 60 μM HbT as a function or source-detector distance for 690 nm (a) and 830 nm (b). Modulation frequency was 110 MHz.

3.4.3 Simulations of varying S_tO_2 and HbT in the brain

Figure 3.5 shows the results of simulating data with varying brain S_tO_2 in the neonate model and recovering μ_a (top row) and μ_s' (bottom row) with the slab model. There was an overall trend of increasing accuracy with increasing source-detector distance in recovering μ_a. There was a relatively large degree of underestimation of $\mu_{a,690}$ at low S_tO_2 where $\mu_{a,690}$ is relatively large. Scattering coefficients were severely underestimated. Figure 3.6 shows the results from calculating S_tO_2 and

Table 3.2: The minimum percent error (MIN), maximum percent error (MAX), and mean absolute percent error (MAPE) for simulations with varying S_tO_2 with fixed HbT.

	SD: 10-25 mm			SD: 15-30 mm			SD: 20-35 mm			SD: 25-40 mm		
	MIN	MAX	MAPE	MIN	MAX	MAPE	MIN	MAX	MAPE	MIN	MAX	MAPE
$\mu_{a,690}$	-19	34	14	-13	22	9	-6	22	9	2	32	16
$\mu_{a,830}$	-15	-9	12	-11	-7	9	-4	-1	2	9	12	10
$\mu'_{s,690}$	-47	-36	43	-50	-38	45	-60	-44	54	-46	-26	40
$\mu'_{s,830}$	-37	-36	36	-42	-41	41	-51	-50	51	-41	-38	40
S_tO_2	-9	21	9	-7	12	6	-6	11	5	-4	22	6
HbT	-14	-12	12	-10	-9	9	-3	-1	2	10	12	11

HbT from the recovered μ_a values in Fig. 5(a-d). There was an overall trend of increasing accuracy with increasing source-detector distance. A summary of the percent errors for simulations with varying S_tO_2 is shown in Table 3.2.

Figure 3.7 shows the results of simulating data with varying HbT in the neonate model and recovering μ_a (top row) and μ'_s (bottom row) via the methods in Section 3.3.3. Recovered μ_a values showed an overall trend of increasing accuracy with increasing source-detector distance, especially for high HbT values. Again, scattering coefficients were severely underestimated. Figure 3.8 shows the results from calculating S_tO_2 and HbT from the recovered μ_a values in Fig. 3.7(a-d). There was a slight trend of increasing accuracy with source-detector distance in recovered S_tO_2 values. There was an overall trend of increasing accuracy in recovered HbT values with increasing source-detector distance, especially at high HbT values. The percent errors for simulations with varying HbT is shown in Table 3.3.

Figure 3.9 shows selected simulations from Figs. 3.6-3.8 repeated at varying modulation frequency. Overall, modulation frequency had little effect on the recovery of μ_a, μ'_s (not shown), S_tO_2, or HbT. There were no apparent trends in accuracy with regards to selection of modulation frequency within a range of 50-200 MHz.

3.4.4 Effects of extra-axial fluid

Figure 3.10 shows the results of simulations with increased extra-axial fluid. Excess CSF caused very large errors in recovered μ_a values, eventually breaking the analysis methods when CSF was

Table 3.3: The minimum percent error (MIN), maximum percent error (MAX), and mean absolute percent error (MAPE) for simulations with varying HbT with fixed S_tO_2.

	SD: 10-25 mm			SD: 15-30 mm			SD: 20-35 mm			SD: 25-40 mm		
	MIN	MAX	MAPE	MIN	MAX	MAPE	MIN	MAX	MAPE	MIN	MAX	MAPE
$\mu_{a,690}$	-23	29	15	-15	21	9	-9	22	8	-8	34	13
$\mu_{a,830}$	-34	-2	22	-25	1	15	-17	5	8	-12	21	8
$\mu'_{s,690}$	-51	-41	48	-53	-40	48	-61	-45	55	-43	-21	36
$\mu'_{s,830}$	-47	-43	45	-48	-42	46	-58	-46	53	-44	-26	37
S_tO_2	-19	-11	13	-12	-8	9	-8	-6	7	-4	-3	4
HbT	-34	1	21	-25	4	15	-17	9	8	-11	28	10

too thick (dependent on source-detector distance). The errors in μ_a propagated large errors in recovered HbT values. The CSF caused similar effects on μ_a for 690 nm and 830 nm, which had minimal effects on recovered S_tO_2. This is consistent with expectations based on the discussion in Section 3.3.3. The first three source-detector distances (10-25 mm, 15-30 mm, 20-35 mm) showed a consistent pattern of underestimation of μ_a due to excess CSF, with shorter source-detector distance being more sensitive. The longest source-detector distance (25-40 mm) showed an unusual pattern, in which increasing CSF initially caused recovered μ_a values to increase before rapidly declining. We found this behavior be related to the specific anatomy of the head model, since this behavior was not reproducible on a regular geometry consisting of concentric spheres (data not shown). We also performed the simulations for 30%, 50%, and 90% S_tO_2, but the results were very similar and are not shown.

3.5 DISCUSSION

In this study, we simulated FD-NIRS measurements to assess the magnitude of errors in recovered S_tO_2 and HbT values using a semi-infinite, homogeneous medium model of the head. We characterized the influence of curvature on errors via simulations on spheres of varying radius. We also simulated data on a segmented structural MRI of a full term neonate in order to estimate the magnitude of errors in a realistic model of a neonate with no morphological abnormalities. Lastly, we investigated the effects of extra-axial fluid by increasing the thickness of CSF layer surrounding the

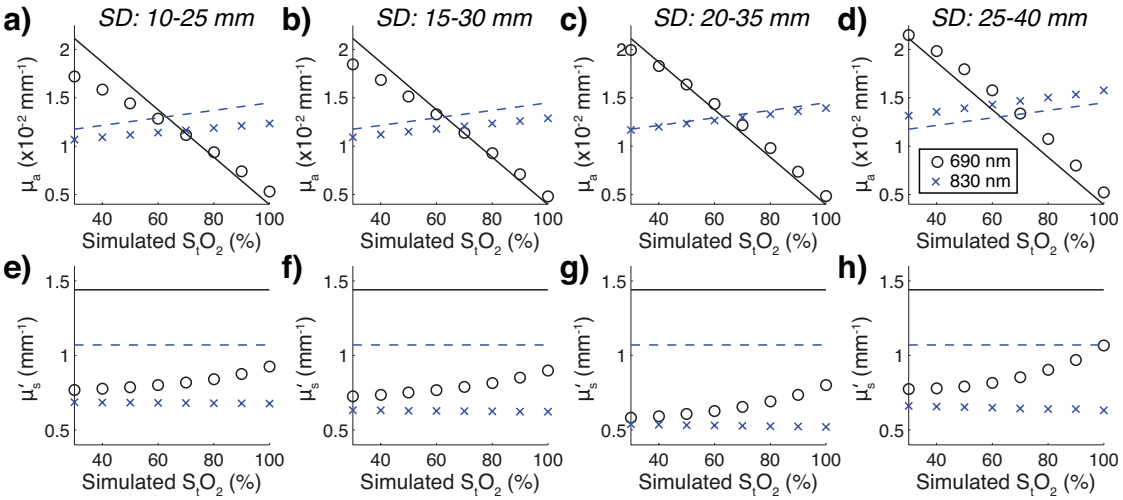

Figure 3.5: Recovered absorption (a-d) and scattering (e-h) coefficients for data simulated on a neonate head model for varying S_tO_2 with fixed HbT in the brain. The solid and dashed lines show the simulated values for 690 nm and 830 nm, respectively. Source-detector separation increases with each column from left to right. Modulation frequency was 100 MHz.

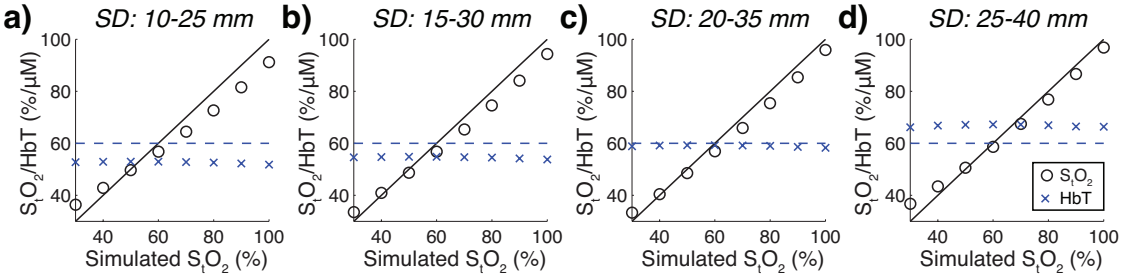

Figure 3.6: Recovered S_tO_2 (O's) and HbT (X's) values for data simulated on neonate head model for varying S_tO_2 with fixed HbT in the brain. The solid and dashed lines show the simulated values for S_tO_2 and HbT, respectively. Source-detector separation increases with each column from left to right. Modulation frequency was 100 MHz.

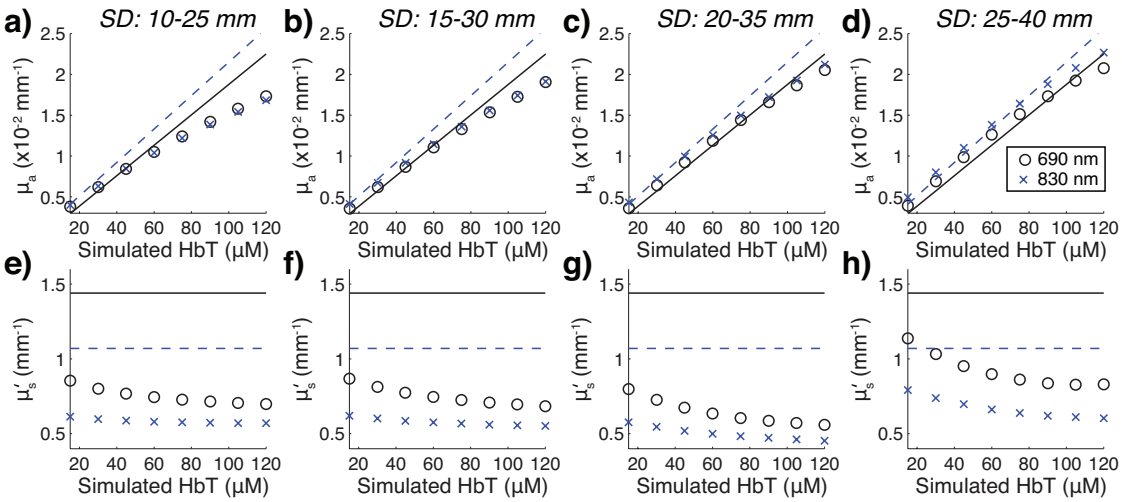

Figure 3.7: Recovered absorption (a-d) and scattering (e-h) coefficients for data simulated on a neonate head model for varying HbT with fixed S_tO_2 in the brain. The solid and dashed lines show the simulated values for 690 nm and 830 nm, respectively. Source-detector separation increases with each column from left to right. Modulation frequency was 100 MHz.

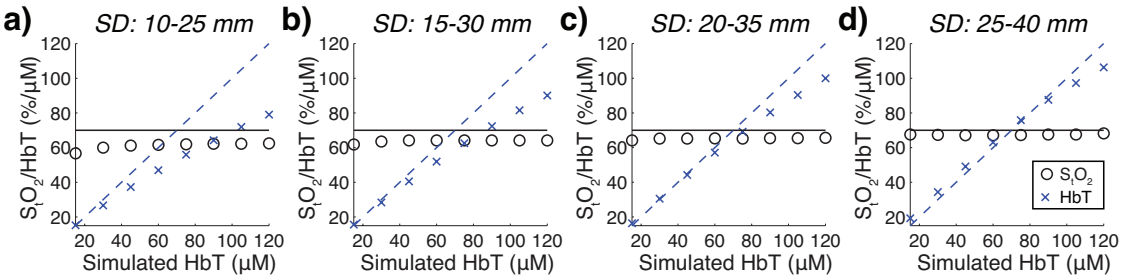

Figure 3.8: Recovered S_tO_2 (O's) and HbT (X's) values for data simulated on neonate head model for varying HbT with fixed S_tO_2 in the brain. The solid and dashed lines show the simulated values for S_tO_2 and HbT, respectively. Source-detector separation increases with each column from left to right. Modulation frequency was 100 MHz.

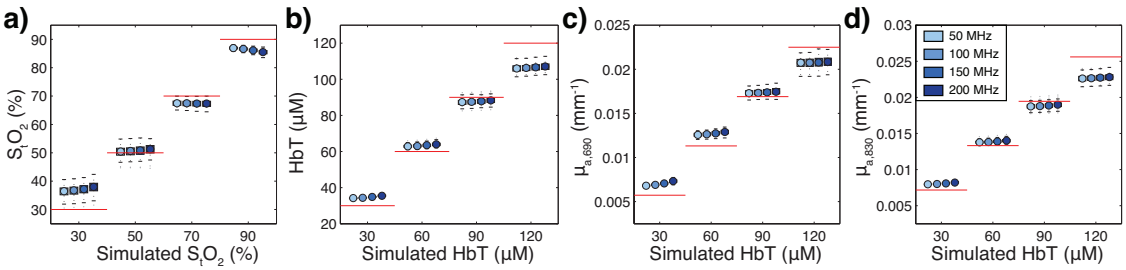

Figure 3.9: Selected simulations showing the effects of varying modulation frequency. (a) Recovered S_tO_2 for simulations with varying S_tO_2 with fixed HbT in the brain. (b) Recovered HbT for simulations with varying HbT with fixed S_tO_2 in the brain. (c) and (d) recovered μ_a values for 690 and 830 nm, respectively, for simulation of varying HbT with fixed S_tO_2 in the brain. The points were plotted as box plots showing the distribution of recovered values due to Monte Carlo noise. The red horizontal lines indicate the target value that was simulated. Source-detector separtion was 25-40 mm.

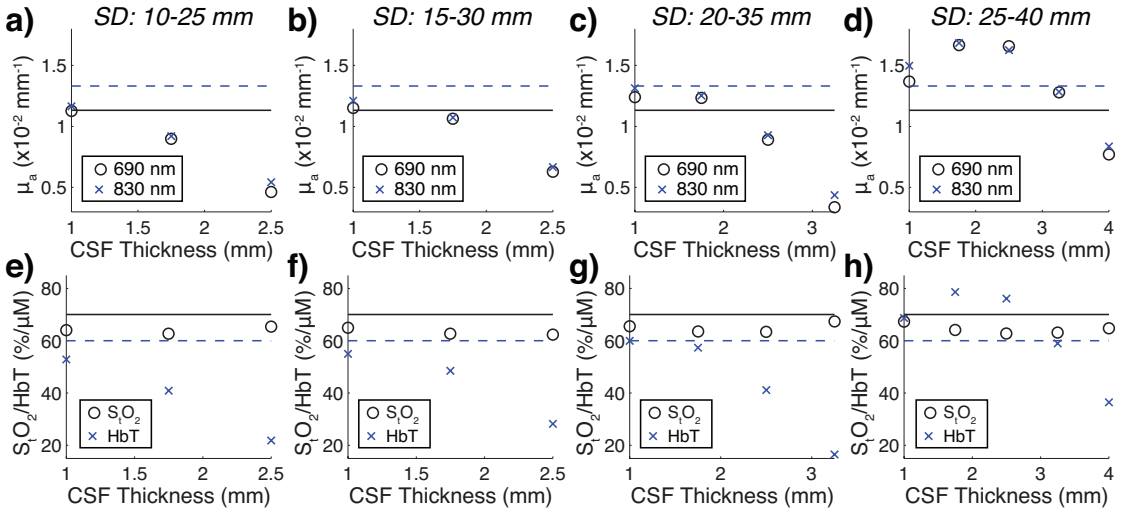

Figure 3.10: The effects of increased CSF on recovered μ_a (a-d) and S_tO_2/HbT (e-h). Source-detector separation increases with each column from left to right. Modulation frequency was 100 MHz.

brain and repeating the simulations. The results presented here help to understand the influence of model violations on the accuracy of recovered S_tO_2, HbT, and μ_a values and assess the validity of common analysis procedures for FD-NIRS data.

3.5.1 Effects of curvature

Curvature induced underestimation of μ_a, μ_s', and HbT. The effects were more severe with decreasing radius of curvature. Curvature had little effect on S_tO_2 estimates. There did not appear to be a strong trend with source-detector separation distance. For the neonate, head curvature can be a potentially significant source of error in recovering μ_a and HbT. For older children and adults, curvature is expected to be less influential.

3.5.2 Effects of source-detector distance

Normalized partial pathlength showed an increasing pathlength through the brain with increasing source-detector separation. The pathlength through superficial layers showed a decreasing trend with source-detector separation. Together these results support the use of longer source-detector distances if signal to noise ratio (SNR) is sufficient. Simulations in the neonate model generally showed an overall trend of increasing accuracy with increasing source-detector distance.

3.5.3 Modulation frequency

The analysis methods described in Section 3.3.3 are based on the diffusion approximation, which is expected to break down at modulation frequencies on the order of ∼1 GHz [20]. In practice, phase wrapping occurs at ∼250 MHz at a distance of 40 mm for the optical properties used in this study. Our results showed only minor differences in the recovered values for modulation frequencies ranging from 50-200 MHz, suggesting that selection of source-detector distance is more important than selection of modulation frequency.

3.5.4 Effects of extra-axial fluid

The presence of extra-axial fluid can cause very large errors in μ_a and HbT, especially at short source-detector distances. Small amounts of extra-axial fluid do not severely affect S_tO_2 estimates;

however, when there is too much CSF, the methods described in Section 3.3.3 will break down resulting in negative μ_a values, in which case estimates of S_tO_2 are no longer feasible.

3.5.5 Combined effects

From the results in Fig. 3.2, we expect curvature to influence underestimation of μ_a. Cerebrospinal fluid mostly influenced underestimation of μ_a, although complicated geometries seemed to produce varying results in some cases. The scalp and skull can influence overestimation or underestimation depending on whether the absorption coefficient values are larger or smaller than that of the brain. This raises the possibility of opposing influences compensating for one another when the relative strengths of their influences are balanced. In general, the strengths of the influences of curvature, extra-cerebral tissues, and CSF will vary with physiological state (i.e., optical properties of the brain relative to other layers), source-detector separation distance, and thickness of extra-axial CSF. We can compare the absorption values of the extra-cerebral tissues, such as the skull or scalp, to the absorption value of the brain at a particular S_tO_2 and HbT value to predict their influence on the errors; however, estimating the overall combined effect is not intuitive and requires systematic investigation, such as by numerical simulation.

3.5.6 Propagation of μ_a errors to S_tO_2 and HbT

Examination of Eqs. 3.9-3.11, as discussed in Section 3.3.3, gave some insight into the characteristics of errors in S_tO_2 and HbT. Because S_tO_2 is a ratio with μ_a values in both the numerator and dominator, it is robust to error influences that act similarly on all wavelengths, such as curvature and CSF. Conversely, the accuracy of HbT is related to the absolute accuracy of the recovered μ_a values regardless of similarity across wavelengths, since HbT is effectively a weighted sum of recovered μ_a values. These effects are illustrated effectively in Figs. 3.2, 3.3, and 3.10.

3.5.7 Typical errors in neonates

For neonates without morphological abnormalities, the mean absolute percent errors (MAPE) of recovered μ_a values were 12% and 7% for 690 nm and 830 nm, respectively. The MAPE for recovered S_tO_2 and HbT were 6% and 9%, respectively. Larger relative errors were noted (~20-30%), but were mostly observed at more extreme physiological values (i.e., very high/low S_tO_2 or HbT). These

results are comparable to the findings of Dehaes et. al. of 8-24% errors in recovered absorption coefficients in neonates [40]. While this level of error may be acceptable for some applications, multi-layered models may offer better accuracy when physiology significantly deviates from the normal values. For clinical populations with extra-axial fluid, advancement to more sophisticated models is necessary to obtain reliable measurements of absorption and hemoglobin.

3.5.8 Limitations

The main limitation of this study is the reliance on a compilation of optical properties in Table 3.1. Furthermore, optical properties vary from person to person, such as with skin pigmentation. Since we simulated data over a wide range of physiological states (i.e., optical properties), the general results presented should represent the typical range of expected errors. Another minor limitation of this study was the use of semi-automated segmentation, which likely produced some misclassification of voxels; however, manual inspection ensured overall quality.

4.0 LAYERED INVERSE MODELS FOR BASELINE PHYSIOLOGY ESTIMATION IN NEONATES

In chapter 3, we showed that the slab model was reasonably accurate for morphologically normal neonates; however, we also saw that excess CSF, which can occur in disease populations, caused very large errors. This chapter attempts to evaluate the performance on non-linear inverse models that incorporate structural information in order to improve estimation of S_tO_2 and HbT. In addition to potentially improving the accuracy of cerebral physiology measurements, this approach will be more flexible in dealing with morphological abnormalities, such as extra-axial fluid, when structural information can be accounted for in the inverse procedure.

4.1 ABSTRACT

Common data analysis procedures for frequency-domain near-infrared spectroscopy (FD-NIRS) use a semi-infinite, homogeneous model of the head. This assumption can introduces bias in estimates of oxygen saturation (S_tO_2) and total hemoglobin (HbT). The purpose of this study was to assess the feasibility of using multi-layered geometries for recovering S_tO_2 and HbT in neonates in order to improve estimation. We tested seven inverse models for recovering physiological parameters in neonates, including the semi-infinite, homogeneous slab model, concentric sphere models, and realistic anatomical models. Except for the slab model, the inverse procedure was implemented using finite element methods (FEM) for the forward computation. Using segmentations of structural magnetic resonance images from 26 neonates, we simulated FD-NIRS data using both finite element methods (diffusion approximation) and Monte Carlo methods (radiative transfer) for varying brain S_tO_2 and HbT. We then examined the recovered values from the seven candidate inverse models. The realistic anatomies, including an atlas and subject-specific anatomy showed potential

for improving recovery of S_tO_2 and HbT; however, we failed to realize these improvements when using more realistic simulations of data via MC methods. This may be due to errors introduced by the diffusion approximation in FEM computations.

4.2 INTRODUCTION

Near-infrared spectroscopy (NIRS) is a non-invasive method for monitoring optical absorption in the brain due to hemoglobin [36]. Measurements acquired at multiple wavelengths within the optical window can be used for the spectral estimation of both oxy-hemoglobin (HbO_2) and deoxy-hemoglobin (Hb). These quantities subsequently provide measurements of tissue oxygenation (S_tO_2) and total hemoglobin (HbT). Near-infrared spectroscopy is relatively portable, less expensive than many other modalities, such as magnetic resonance imaging (MRI) or positron emission tomography (PET), and is non-ionizing and non-restraining, making it an attractive technology for the development of bedside monitoring tools. Previous studies have shown promising results in detecting hypoxic-ischemic brain injuries [3, 4] and monitoring the brain during cardiac surgery [2].

Current clinical systems, which are based on continuous wave (CW-) light sources, have been useful for monitoring trends in physiology, but lack quantitative accuracy [38]. A potentially more promising approach is frequency-domain (FD-) NIRS, which uses an amplitude modulated light source that is modulated in intensity by a sinusoidal function in the range of $\sim$25-200 MHz. This technique measures both amplitude and phase of the modulated light, which improves absolute quantification of hemoglobin by providing information about the optical pathlength via the phase. Often, FD-NIRS data is analyzed using a semi-infinite, homogeneous model [39], because of the existence of an analytical solution to the light propagation, which simplifies estimation of optical properties from measurements. Previous studies have found that this approach introduces bias into the estimates optical properties and subsequent estimates of S_tO_2 and HbT [40, 35].

In this work, we used segmented structural MRI from neonates to simulate FD-NIRS measurements. We attempted to recover S_tO_2 and HbT values of the brain using several candidate inverse models in order to assess the accuracy of using multi-layered models for FD-NIRS data analysis. The candidate models included the (i) the analytical semi-infinite, homogeneous slab model, (ii) homogeneous sphere, (iii) two-layer concentric sphere, (iv) three-layer concentric sphere with a

fixed CSF-layer, (v) an atlas, and subject-specific anatomy using the (vi) contralateral and (vii) ipsilateral side of the head. The analytical slab model was chosen as a baseline for comparison. The concentric sphere models offer some modeling of curvature and layered structure, but simplify the implementation over an atlas or subject-specific anatomy in that probe-registration is eliminated and the geometries are easy to generate meshes for. The subject-specific anatomy model offer the most complex implementation, since individual MRI must be acquired, segmented, meshed, and registered to the probe geometry. We chose to use both the ipsilateral and contralateral sides of the head to assess the sensitivity to the specific anatomical variations and probe registration errors.

4.3 METHODS

4.3.1 Data Simulation

We segmented 26 neonate T2 structural MRI (Full Term, 0-123 days, median age = 10 days) into four layers: scalp, skull, cerebrospinal fluid (CSF), and brain. Brain and CSF segmentations were obtained via SPM8 software (Wellcome Trust Centre for Neuroimaging, London, UK) using a neonate atlas from the University of North Carolina [46] as a template. The segmented images were then used to simulate FD-NIRS data using the optical properties specified in Table 4.1. The scalp, skull, and CSF properties were fixed, while the optical properties of the brain were varies with S_tO_2 (30-100%) and HbT (10-100 μM). The segmentation were converted to tetrahedral meshes via the iso2mesh software package [48] for use in finite element method (FEM) computations.

We simulated the data in two different ways using two different software packages: (i) FEM via NIRFAST software [49] and (ii) Monte Carlo (MC) methods via Monte Carlo Extreme (MCX) software [25]. Simulating measurements via FEM (and recovering via FEM) allowed us to assess the inverse procedure using different geometries without considering the effects of the diffusion approximation errors, meshing/discretization errors, and stochastic noise. Simulating measurements via MC methods provides more accurate simulation of measurements, especially with respect to CSF which violates the assumptions of the diffusion approximation, but introduces modeling errors, meshing errors, and stochastic noise. Thus, by performing simulations using both methods we can isolated the effects of geometry and also assess the accuracy of the methods under more realistic assumptions. The NIRFAST package simulates FD measurements directly, while the MCX

Table 4.1: Optical properties of tissues; RI = refractive index.

	$\mu_{a,690}$ (mm^{-1})	$\mu_{a,830}$ (mm^{-1})	$\mu'_{s,690}$ (mm^{-1})	$\mu'_{s,830}$ (mm^{-1})	RI
Skin/Scalp	0.0206[a]	0.0122[a]	2.37[a]	1.81[a]	1.45[b]
Skull	0.0255[c]	0.0252[c]	2.35[c]	1.75[c]	1.45[b]
CSF	0.0004[d]	0.0026[d]	0.01[d]/0.3[e]	0.01[d]/0.3[e]	1.33[b]
Brain	0.0039-0.0285[f]	0.0051-0.0256[f]	1.44[b]	1.07[b]	1.45[b]

[a][41]; [b][14]; [c][42]; [d][32]; [e][50] for FEM computations; [f]Based on spectra from [43, 44]

software packages simulates photon propagation in the time domain. The time-domain signals were converted to FD measurements via discrete Fourier transform.

We used a linear probe consisting of 2 detector and 4 source positions, giving 8 unique distances that were evenly spaced between 20-40 mm. The probe was centered on the C3 and C4 positions in the 10/20 international system with the probe aligned in the anterior-posterior orientation. Each source position was simulated at 690 nm and 830 nm, which is a common choice of wavelengths. The modulation frequency was 110 MHz, which matches the Imagent ISS system FD-NIRS system.

4.3.2 Inverse Geometries

The simulated FD-NIRS data were fit to seven candidate inverse model geometries: (i) the analytical semi-infinite, homogeneous slab model, (ii) homogeneous sphere, (iii) two-layer concentric sphere, (iv) three-layer concentric sphere with a fixed CSF layer, (v) an atlas, and subject-specific anatomy using the (vi) contralateral and (vii) ipsilateral side of the head. The homogeneous slab model is described in [39], in which the optical properties are recovered from the slopes two linear regressions based on the amplitude and phase data. This model is commonly used for FD-NIRS because it is simple to implement and has an analytic expression. This model was considered as the baseline for performance comparison.

All of the other geometries required iterative non-linear regression procedure described below to fit the model. The concentric sphere models were chosen because they model the finite volume/curvature of the head and layered tissue structure and the implementation is simpler than anatomical models. All of the spherical geometries used a sphere of 60 mm radius. The homoge-

neous sphere consisted of a single "layer", which was taken to be the brain. The 2-layer sphere model consisted of an outer layer 7 mm thick, which was meant to model superficial tissues, and a brain layer in the center. The 3-layer sphere consisted of 7 mm outer layer for superficial tissues, a 2 mm CSF layer with fixed optical properties, and a brain layer in the center.

We chose an atlas model as the next level in complexity of implementation. This model includes general anatomical information and requires more effort to register the NIRS probe to the volume. The contralateral hemisphere model was chosen to add subject-specific anatomical information. The anatomy of the contralateral hemisphere and probe registration to the opposite hemisphere potentially introduce realistic errors due to segmentation, meshing, and probe registration. The ipsilateral hemisphere geometry was chosen to be a model of the best possible scenario, in which segmentation, meshing, and probe registration errors are minimized. The atlas and subject-specific anatomical models consisted of an outer layer that combining the scalp and skull, a CSF layer with fixed properties, and a brain layer that combined white matter and gray matter regions.

4.3.3 Inverse Procedure

The absorption coefficient can be described by

$$\mu_a = \sum_j \epsilon_j c_j \ , \tag{4.1}$$

where c_j is the concentration of chromophore j and ϵ_j is the molar extinction coefficient. The chromophores of interest for this work were HbO_2 and Hb. An additional fixed contribution to the absorption coefficient from 70% water content was also assumed. From Mie scattering theory, the reduced scattering coefficient was modeled as

$$\mu_s' = a \left(\frac{\lambda}{500 \text{ nm}} \right)^{-b} \ , \tag{4.2}$$

where λ is the wavelength in nm, and a and b are parameters. The parameter b was fixed at a value of 1.5. The value of a was considered a global parameter that was fit for the entire volume. The diffusion coefficient is given by

$$\kappa = \frac{1}{3(\mu_a + \mu_s')} \approx \frac{1}{3\mu_s'} \ . \tag{4.3}$$

Given the optical properties of the head, we can predict the measurement for channel m as

$$\hat{y}_m\big(\lambda_m, \mu_a(\boldsymbol{r}, \lambda_m), \kappa(\boldsymbol{r}, \lambda_m)\big) = f\big(\lambda_m, \mu_a(\boldsymbol{r}, \lambda_m), \kappa(\boldsymbol{r}, \lambda_m)\big) + s_r(\lambda_m) + i\ s_i(\lambda_m)\ , \tag{4.4}$$

where $\boldsymbol{r}$ is the position; f is the natural log of the measurement output from NIRFAST, in which the real part is log amplitude and the imaginary part is the phase; and s_r and s_i are intercept terms for log amplitude and phase, respectively. Using the chain rule, we can calculate the following derivatives:

$$\frac{\partial \hat{y}_m}{\partial c_j(\boldsymbol{r})} = \epsilon_j \frac{\partial f}{\partial \mu_a(\boldsymbol{r}, \lambda_m)} \tag{4.5}$$

$$\frac{\partial \hat{y}_m}{\partial a(\boldsymbol{r})} = -3\ \kappa^2(\boldsymbol{r}, \lambda_m)\ \left(\frac{\lambda_m}{500\ \text{nm}}\right)^{-b} \frac{\partial f}{\partial \kappa(\boldsymbol{r}, \lambda_m)} \tag{4.6}$$

$$\frac{\partial \hat{y}_m}{\partial s_r(\lambda_m)} = 1 \tag{4.7}$$

$$\frac{\partial \hat{y}_m}{\partial s_i(\lambda_m)} = 1\ , \tag{4.8}$$

where the derivatives with respect to μ_a and κ are calculated via the adjoint method in NIRFAST. Next, we define the following two vectors for the [log of] measurements $\boldsymbol{y}$ and the predicted measurements $F(\boldsymbol{x})$:

$$\boldsymbol{y} = \begin{bmatrix} \Re(y_1) & \dots & \Re(y_M) & \Im(y_1) & \dots & \Im(y_M) \end{bmatrix}^T \tag{4.9}$$

$$F(\boldsymbol{x}) = \begin{bmatrix} \Re(\hat{y}_1(\boldsymbol{x})) & \dots & \Re(\hat{y}_M(\boldsymbol{x})) & \Im(\hat{y}_1(\boldsymbol{x})) & \dots & \Im(\hat{y}_M(\boldsymbol{x})) \end{bmatrix}^T\ , \tag{4.10}$$

where the vector $\boldsymbol{x}$ is a collection of the model parameters, and $\Re(\cdot)$ and $\Im(\cdot)$ indicate the real and imaginary parts. For the one-layer model (homogeneous sphere), this contains HbO_2 concentration, Hb concentration, the global scattering term a, and four intercept terms for the two different wavelengths (7 total parameters). For the models with two-layers, $\boldsymbol{x}$ contains the same terms, except there are two HbO_2 and two Hb concentration values for each of the two layers (9 total parameters). The derivatives are organized appropriately in the Jacobian matrix, such that

$$J = \frac{\partial F(\boldsymbol{x})}{\partial \boldsymbol{x}}\ . \tag{4.11}$$

For each iteration we can update the parameters using the Levenberg-Marquardt update step [30]:

$$\Delta \boldsymbol{x} = (J^T W J + \alpha\ \text{diag}(J^T W J))^{-1} J^T W (\boldsymbol{y} - F(\boldsymbol{x}))\ , \tag{4.12}$$

where α is a regularization parameter that is increased if the step size is too large or the iteration fails to improve the model fit, and W is a weight matrix that was proportional to inverse of the covariance matrix of the measurements. In order to estimate an appropriate weight matrix, the

variance over multiple MC simulations was used. The cost function used to assess the model fit was

$$C(\boldsymbol{x}) = \frac{1}{2}(\boldsymbol{y} - F(\boldsymbol{x}))^T W(\boldsymbol{y} - F(\boldsymbol{x})) \ . \tag{4.13}$$

Convergence was defined by choosing a step size that was too small (<0.5% of $\boldsymbol{x}$, excluding intercepts), failing to improve the model fit for 5 iterations, or reaching a maximum of 30 iterations. Once convergence was reached, total hemoglobin concentration and oxygen saturation were calculated as

$$\mathrm{HbT} = \mathrm{HbO_2} + \mathrm{Hb} \tag{4.14}$$

$$\mathrm{S_tO_2} = \mathrm{HbO_2/HbT} \times 100\% \ . \tag{4.15}$$

4.3.4 Assessment of the inverse models

We used two metrics to assess variance and bias of inverse procedure using different geometries. To assess variance, we first calculated a robust estimate for the standard deviation across subjects using the median absolute deviation at each simulated value:

$$\sigma_{\mathrm{MAD},j} = 1.483 \ \mathrm{median}(|\hat{z} - \mathrm{median}(\hat{z})|) \ , \tag{4.16}$$

where $\sigma_{\mathrm{MAD},j}$ is the standard deviation of the j^{th} simulated value of either $\mathrm{S_tO_2}$ or HbT, $\hat{z}$ is a vector of estimated values across subjects, and median returns the median of the argument. Once the standard deviation was calculated for each simulated value, they were averaged across stimulated values:

$$\langle \sigma_{\mathrm{MAD}} \rangle = \frac{1}{N} \sum_{j=1}^{N} \sigma_{\mathrm{MAD},j} \ . \tag{4.17}$$

The standard error of this metric was estimated via bootstrap sampling. The bias at the j^{th} simulated value was estimated using the median estimator:

$$\mathrm{bias}_j = \mathrm{median}(\hat{z} - z) \ , \tag{4.18}$$

where z is the true simulated value and $\hat{z}$ is the estimated value for each subject. The mean of the absolute value of the bias across simulated values was then calculated as

$$\langle |\mathrm{bias}| \rangle = \frac{1}{N} \sum_{j=1}^{N} |\mathrm{bias}_j| \ . \tag{4.19}$$

Again, the standard error of these estimates were calculated by bootstrap sampling. These robust estimators were chosen so that the summary statistics would not be excessively influenced by a few outliers.

4.4 RESULTS

Figure 4.1 shows the relative pathlength of photons through each layer of concentric sphere models of varying radius and layer thickness. The three spheres correspond roughly to the anatomy of a neonate, child, and adult. The neonate shows a high proportion of the optical pathlength through the brain at typical source-detector distances for FD-NIRS (∼20-40 mm). We can see that the sensitivity to the brain quickly decreases as the superficial layers increase in thickness.

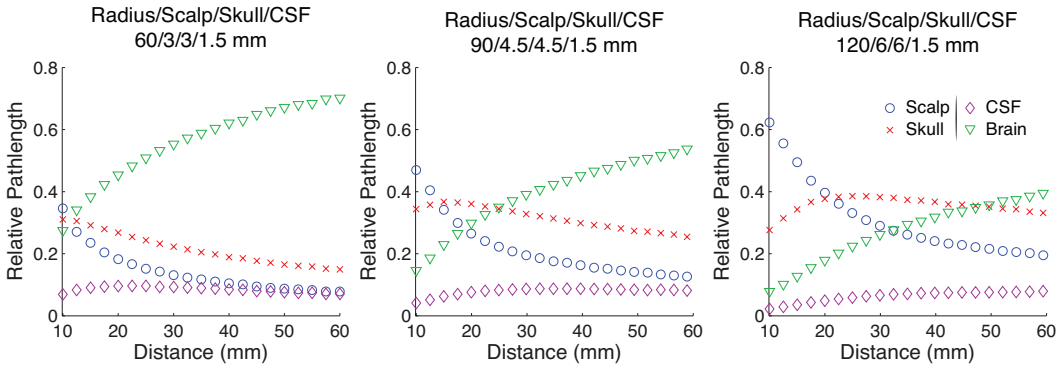

Figure 4.1: The relative pathlength through multi-layered concentric spheres of varying radius and layer thicknesses.

Figure 4.2 shows the recovered S_tO_2 values for NIRS data simulated with FEM. The slab model performed relatively well. The concentric sphere models, especially the 2-layered and 3-layered models performed poorly. This may be the result of over-fitting the geometry mismatch. The atlas, contralateral hemisphere, and ipsilateral hemisphere models all produced reasonable results with visually better agreement between recovered and simulated S_tO_2 as the inverse geometry more closely matched the subjects anatomy.

Figure 4.3 shows the recovered HbT values for NIRS data simulated with FEM. Once again, the slab model performed relatively well, and the 2-layered and 3-layered sphere models performed

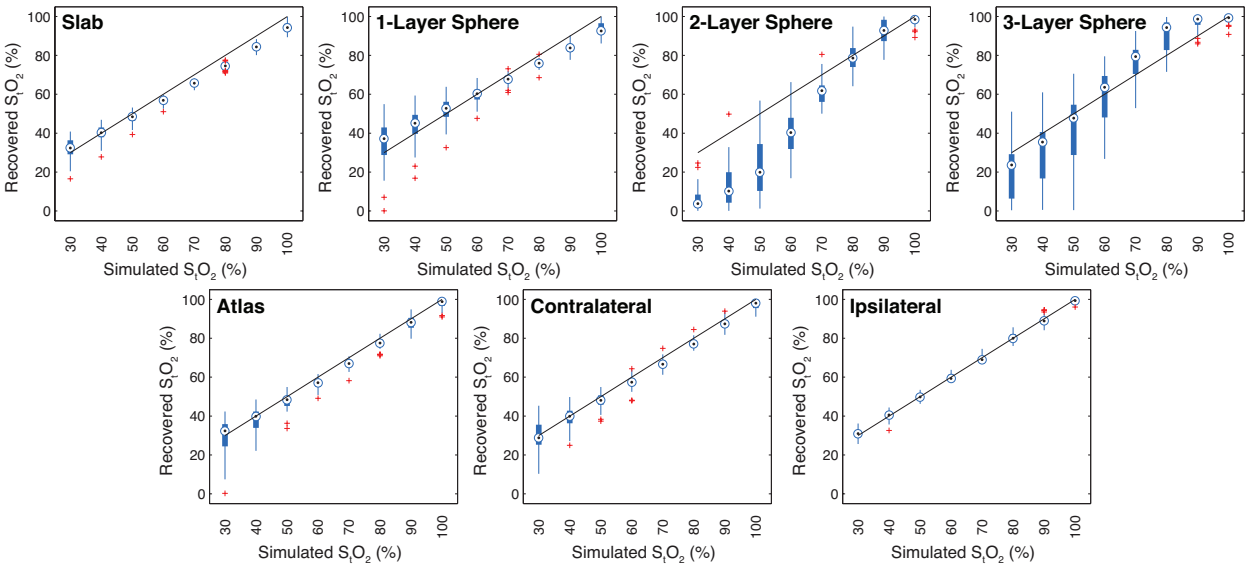

Figure 4.2: Box plots showing the distribution recovered S_tO_2 values for data simulated with FEM for all seven candidate inverse geometries.

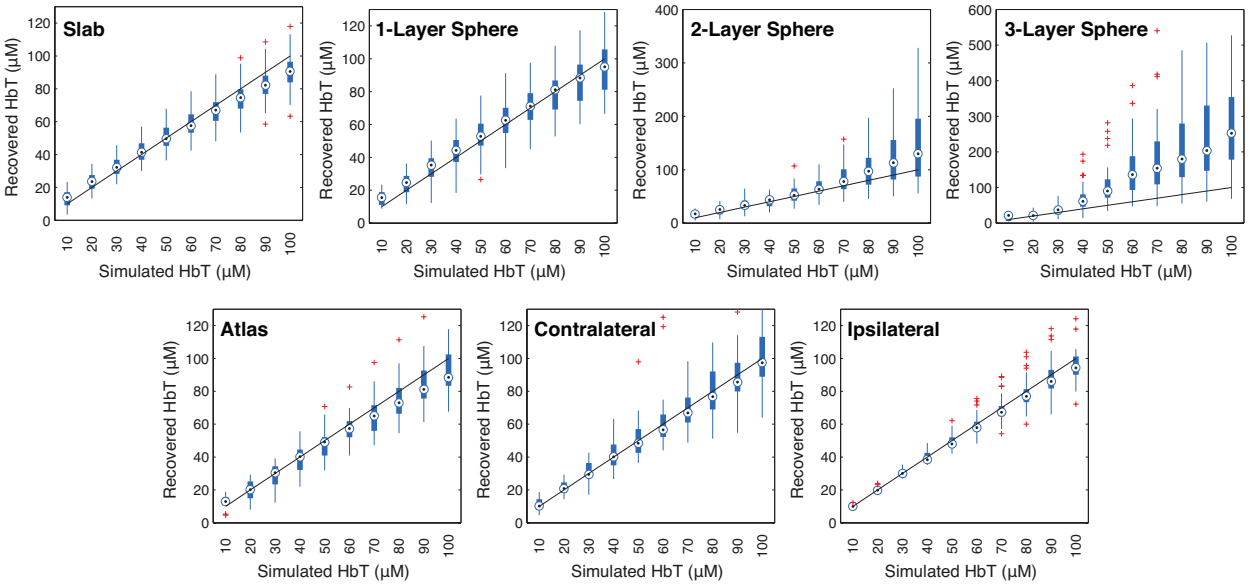

Figure 4.3: Box plots showing the distribution of recovered HbT values for data simulated with FEM for all seven candidate inverse geometries.

Table 4.2: Summary statistics for recovered S_tO_2 and HbT for data simulated with FEM.

	S_tO_2		HbT	
	$\langle \sigma_{\text{MAD}} \rangle$	$\langle$ |Bias| $\rangle$	$\langle \sigma_{\text{MAD}} \rangle$	$\langle$ |Bias| $\rangle$
Slab	2.6 ± 0.2	3.6 ± 0.2	7.9 ± 0.7	4.3 ± 0.5
1-Layer Sphere	4.5 ± 0.4	4.5 ± 0.4	10.5 ± 0.9	3.5 ± 0.6
2-Layer Sphere	7.9 ± 0.7	14.9 ± 0.8	25 ± 2	11 ± 2
3-Layer Sphere	9.2 ± 1.1	6.5 ± 0.9	61 ± 6	63 ± 6
Atlas	3.5 ± 0.4	2.0 ± 0.2	8.7 ± 0.7	4.0 ± 0.7
Contralateral	3.5 ± 0.4	2.2 ± 0.2	8.7 ± 0.9	2.6 ± 0.5
Ipsilateral	1.9 ± 0.2	0.7 ± 0.1	4.2 ± 0.5	2.2 ± 0.3

poorly. The atlas, contralateral hemisphere, and ipsilateral hemisphere models all produced reasonable results with visually better agreement between recovered and simulated S_tO_2 as the inverse geometry more closely matched the subjects anatomy.

Table 4.2 shows the summary statistics of the results shown in Figs. 4.2 and 4.3. The homogeneous sphere model produced poorer results than the slab model on nearly all metrics. The 2-layer and 3-layer concentric sphere models produced very poor results in all metrics. The atlas showed decreased bias in S_tO_2, but no other improvements over slab model. Both the contralateral and ipsilateral hemsiphere geometries showed decreased bias in both S_tO_2 and HbT; however, only the ipsilateral hemsiphere geometry showed decreased variance (in both S_tO_2 and HbT).

Figure 4.4 shows the recovered S_tO_2 values for NIRS data simulated with MCX. The slab model performed worse than with data simulated by FEM with more significant bias. The data show a distinct pattern of overestimation at low S_tO_2 and underestimation at high S_tO_2. This could potentially be a result of the more realistic simulation of light propagation through CSF. The concentric sphere models showed better results than with data simulated by FEM. It is possible that the additional sources of error (i.e., diffusion approximation errors, stochastic noise) acted as regularization that prevented overfitting of model geometry mismatch. However, the 2-layer and 3-layer sphere models visibly show high variance in recovered values.

Figure 4.4 shows the recovered HbT values for NIRS data simulated with MCX. All of the models show a similar pattern of under-estimation at high HbT. Again, the 2-layer and 3-layer sphere models show high variance in recovered values across subjects.

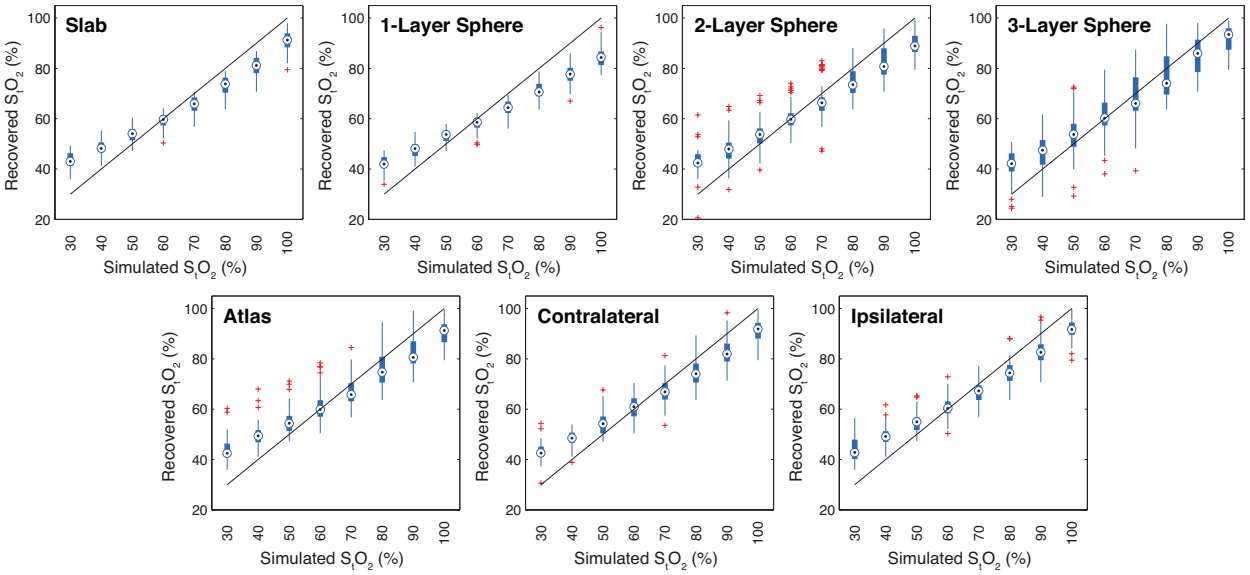

Figure 4.4: Box plots showing the distribution of recovered S_tO_2 values for data simulated with MC for all seven candidate inverse geometries.

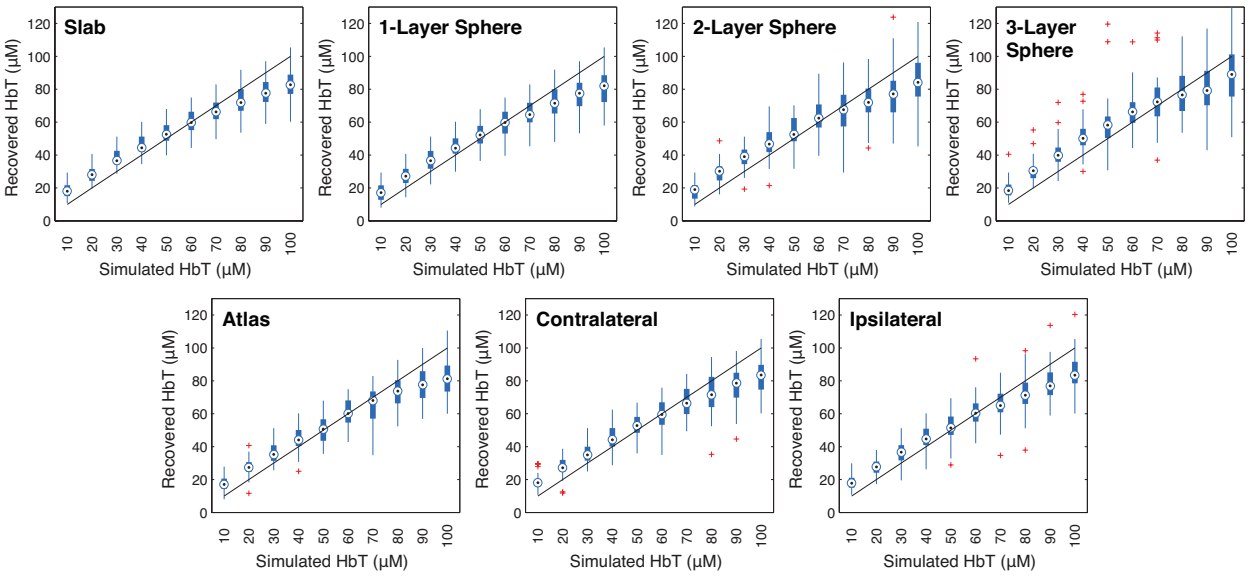

Figure 4.5: Box plots showing the distribution of recovered HbT values for data simulated with MC for all seven candidate inverse geometries.

Table 4.3: Summary statistics for recovered S_tO_2 and HbT for data simulated with MC.

	S_tO_2		HbT	
	$\langle\sigma_{\text{MAD}}\rangle$	$\langle$ |Bias| $\rangle$	$\langle\sigma_{\text{MAD}}\rangle$	$\langle$ |Bias| $\rangle$
Slab	3.5 ± 0.2	6.7 ± 0.3	7.1 ± 0.5	7.4 ± 0.4
1-Layer Sphere	3.2 ± 0.2	8.4 ± 0.2	8.3 ± 0.5	7.3 ± 0.5
2-Layer Sphere	4.8 ± 0.4	6.9 ± 0.3	9.7 ± 0.6	7.8 ± 0.6
3-Layer Sphere	6.9 ± 0.6	5.4 ± 0.5	10.4 ± 0.6	8.3 ± 0.7
Atlas	4.8 ± 0.3	6.9 ± 0.4	8.8 ± 0.5	6.8 ± 0.5
Contralateral	4.4 ± 0.4	6.4 ± 0.3	8.6 ± 0.6	6.9 ± 0.5
Ipsilateral	4.2 ± 0.3	6.5 ± 0.3	7.3 ± 0.5	7.3 ± 0.4

Table 4.3 shows the summary statistics of the results shown in Figs. 4.4 and 4.5. The homogeneous sphere model produced poorer results than the slab model on nearly all metrics. Only the 3-layered sphere model showed reduced bias in S_tO_2; however, the significantly increased variance in recovered HbT values is problematic in suggesting its implementation in practice.

4.5 DISCUSSION

In this study, we simulated FD-NIRS measurements from the anatomy of 26 neonates using both finite element methods and Monte Carlo methods for varying S_tO_2 and HbT in the brain. We then attempted to recover the S_tO_2 and HbT from the simulated data using seven candidate inverse geometries, including (i) semi-infinite, homogeneous slab, (ii) homogeneous sphere, (iii) 2-layer concentric sphere, (iv) 3-layer concentric sphere with the middle layer fixed to CSF, (v) an atlas, and using the subject specific anatomy from the contralateral (vi) and ipsilateral (vii) hemispheres. The first model used an analytical formula for light propagation, while the other models were implemented as iterative non-linear regressions using FEM to perform the forward calculations and the Levenberg-Marquardt algorithm to update the parameters.

By using data that were simulated with FEM, we were able to assume that segmentation errors, meshing errors, and modeling errors were minimized and look at the isolated effects of inverse model

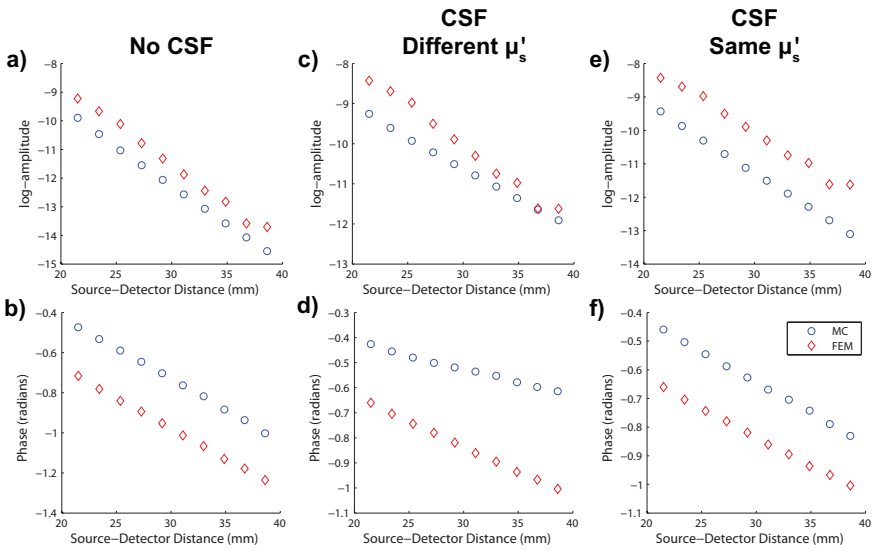

Figure 4.6: Comparison of simulated measurements from Monte Carlo and finite element methods on a concentric sphere model. For the left column (a-b), the sphere was homogeneous. In the center column (c-d), a CSF layer was inserted at a depth of 7 mm, in which the scattering coefficient for MC/FEM was 0.01/0.3 mm^{-1}. In the right column (e-f), the scattering coefficient of CSF for the MC simulation was increased to match that of the FEM data (0.3 mm^{-1}).

geometry. Recovery on the atlas, contralateral hemisphere, and ipsilateral hemisphere all showed improvements in at least some metrics. The ipsilateral hemisphere model may be viewed as the best that can be achieved when light propagation is modeled correctly and errors from segmentation, meshing, and probe registration are minimized. On the other hand, the contralateral hemisphere may be a more realistic model of recovery on subject specific anatomy, since the contralateral hemisphere may be analogous to having segmentation/meshing errors and probe registration errors. In any case, incorporating anatomical information into the recovery process may reduce bias in estimated values.

All of the FEM based inverse geometries failed to realize any improvements over the slab model on data simulated with MC methods. The data simulated with MC methods contained additional sources of errors from converting the segmentation to FEM mesh for the inverse procedure and differences in the modeling of light propagation through CSF, which does not adhere to the assumptions of the diffusion approximation. The visible difference in the recovered values for data

simulated with FEM (diffusion) and MC (radiative transfer) suggests that the more pertinent issue might be with CSF modeling.

In order to confirm this result, we performed post-hoc simulations using both MC and FEM of data on spherical model (60 mm radius) that was either homogeneous or contained a 2 mm CSF layer inserted at 7 mm depth. Except for the CSF region, the rest of the medium had optical properties that match the brain at 70% S_tO_2 and 60 μM HbT. The results are shown in Fig. 4.6. When there was no CSF in the medium, the MC and FEM simulations agree up to an intercept. When CSF was inserted into the medium, MC and FEM showed clear disagreements. When the scattering coefficient in the MC was increased to match the value used in FEM, the two methods more closely agree again. In the FEM, μ_s' must be increased to ensure that the model is numerically stable. It is clear that at least part of the error is due to the artificial increase in scattering coefficient. The FEM is based on a first order expansion of the radiative transfer equation. This expansion results in the assumption that $\mu_s' \gg \mu_a$, which does not hold for CSF. Using a higher order expansion in the FEM calculations can potentially remove this restriction and fix issues with CSF modeling.

In conclusion, we have found simple concentric sphere models to be insufficient for modeling the structure of the head in neonates in the context of separating absorption of the brain from the superficial layers. More realistic geometries, such as using an appropriate atlas or subject specific anatomy, may improve recovery of S_tO_2 and HbT; however, we failed to realize these benefits when simulating data using MC methods. We hypothesize that this is related to the modeling of CSF in FEM, and that better modeling of CSF will improve results.

5.0 REDUCTION OF SYSTEMIC PHYSIOLOGY AND MOTION EFFECTS ON EVOKED HEMODYNAMICS DETECTION

This chapter shifts the focus from baseline physiology estimation to functional brain imaging. The work focuses on two goals: (i) investigate the effects of NIRS specific noise sources, such as the contributions to the NIRS signal from systemic physiology and motion, on common ordinary least-squares estimation procedures and (ii) to mitigate the effects of these noise sources with the development of a new algorithm for estimation of the general linear model. The work presented in this chapter has been published in Biomedical Optics Express [51], and is available online at http://www.opticsinfobase.org/boe/abstract.cfm?uri=boe-4-8-1366 ().

5.1 ABSTRACT

Systemic physiology and motion-induced artifacts represent two major sources of confounding noise in functional near infrared spectroscopy (fNIRS) imaging that can reduce the performance of analyses and inflate false positive rates (i.e., type I errors) of detecting evoked hemodynamic responses. In this work, we demonstrated a general algorithm for solving the general linear model (GLM) for both deconvolution (finite impulse response) and canonical regression models based on designing optimal pre-whitening filters using autoregressive models and employing iteratively reweighted least squares. We evaluated the performance of the new method by performing receiver operating characteristic (ROC) analyses using synthetic data, in which serial correlations, motion artifacts, and evoked responses were controlled via simulations, as well as using experimental data from children (3-5 years old) as a source baseline physiological noise and motion artifacts. The new method outperformed ordinary least squares (OLS) with no motion correction, wavelet based mo-

tion correction, or spline interpolation based motion correction in the presence of physiological and motion related noise. In the experimental data, false positive rates were as high as 37% when the estimated p-value was 0.05 for the OLS methods. The false positive rate was reduced to 5-9% with the proposed method. Overall, the method improves control of type I errors and increases performance when motion artifacts are present.

5.2 INTRODUCTION

Functional near infrared spectroscopy (fNIRS) is a non-invasive brain imaging technique that is based on the spectroscopic measurement of the optical absorption of cerebral blood [36]. Evoked changes in tissue hemoglobin concentrations are detected by an array of light sources and detectors on the scalp that monitor changes in optical absorption and scattering. Both oxy-hemoglobin (HbO_2) and deoxy-hemoglobin (Hb) concentration changes can be estimated from the modified Beer-Lambert law [16] using absorption measurements taken at multiple wavelengths of light within the optical window (650-850 nm). In comparison to other cerebral vascular imaging methods such as functional magnetic resonance imaging (fMRI) or positron emission tomography (PET), fNIRS imaging is considerably lower cost and more portable. Because it is non-ionizing and non-confining, fNIRS is particularly well suited for non-invasive studies in children or infants. In addition, the portability of fNIRS and its ability to record brain signals during moderate subject movement has allowed its use during various tasks such as walking [7, 8], balance [9, 10, 11], or social interaction [12], which otherwise could not be imaged by conventional fMRI.

Functional NIRS imaging is accomplished through a set of spatially arranged optical sources and detectors (optodes), which are often coupled through fiber optics between a head cap worn by the participant and the fNIRS instrument. Although fNIRS can be used to image brain activity during participant movement, fNIRS is prone to artifacts introduced by slippage of these optodes and headcap on the surface of the scalp. These artifacts are particularly common in studies involving children or infants where the fNIRS cap is more loosely fastened on the head to increase participant tolerance of the method. A great deal of effort has been spent by researchers in developing better methods for identification and removal of motion artifacts, including principal component analysis [34], spline interpolation [52], wavelet transform [53], and Kalman filtering [54] based algorithms. These methods were compared by Cooper et. al. [55], in which spline interpolation and wavelet

based filtering gave the best results for two different performance metrics. As a note, these methods are applied in pre-processing of the fNIRS data and in general have some level of subjective tuning involved in the implementation of the algorithm. In addition to motion artifacts, fNIRS signals are also contaminated by superficial and systemic physiological signals such as cardiac, respiratory, and blood pressure oscillations. Because fNIRS signals are measured from sensors placed on the surface of the scalp, these measurements have a high sensitivity to superficial changes in optical absorption. These slow background oscillations contribute to serially correlated noise in fNIRS measurements. This effect is increased by the high sampling rate of fNIRS instruments (∼10 Hz or more) that is substantially faster than the underlying physiological signals.

Motion artifacts and serial correlations due to physiology violate common statistical assumptions of the independence of repeated measurements over time. Subsequently, these sources of noise can contribute to inaccurate estimation of type I errors. In this work, we describe an iterative algorithm that utilizes an autoregressive model based pre-whitening filter and robust regression to reduce the effects of physiological and motion-induced sources of noise, respectively. We demonstrated that this algorithm has better performance than ordinary least squares with no motion correction, wavelet based motion correction [53], or spline interpolation based motion correction [52] in the presence of physiological noise and motion artifacts for both deconvolution (e.g., HOMER [34]) and canonical (e.g., SPM-NIRS [56]) based regression models. Our proposed algorithm is demonstrated for both synthetic and experimental data containing motion artifacts. In addition, we tested both short (event-related design) and long (block design) duration tasks as well as varying magnitudes of hemoglobin concentration changes (contrast to noise ratios).

5.3 METHODS

5.3.1 Theory

The simplest model of the observed fNIRS signal is an evoked response with a normally distributed error term as given by

$$y_t = h_t + \epsilon_t \tag{5.1a}$$

$$\epsilon_t \sim \mathcal{N}(0, \sigma^2) \ , \tag{5.1b}$$

where y_t is the observed signal; h_t is the evoked hemodynamic response; ϵ_t is the noise at time t;

and σ^2 is the variance of ϵ_t. The additive noise term in the fNIRS signal is often contaminated with a high degree of physiological noise, which is sampled at the high temporal resolution of fNIRS instruments leading to serially correlated error terms. In other words, slow physiological oscillations are sampled rapidly causing nearby time points in the fNIRS signal to be highly correlated. The presence of these errors can greatly affect the false positive rate (e.g., type I error) of the model and lead to inaccurate interpretations of the data. In standard linear regression methods, serially correlated errors are often dealt with by pre-whitening based on an autoregressive (AR) model of the error terms. A first-order model (AR(1)) of the error terms is

$$\epsilon_t = \rho_1 \ \epsilon_{t-1} + \nu_t \tag{5.2a}$$

$$\nu_t \sim \mathcal{N}(0, \sigma^2) \ , \tag{5.2b}$$

where the the error term at the current time point (t) depends on the error term from the previous sample point ($t-1$). Estimating the coefficients of the AR model and designing a filter that is applied to both sides of the equation can remove the correlation between subsequent time points. For the AR(1) model, a simple filter can be constructed as $f = [1 \quad -\rho_1]^T$ and applied to equation 5.2a to produce

$$f * y_t = (y_t - \rho_1 y_{t-1}) = (h_t - \rho_1 h_{t-1}) + \nu_t \ , \tag{5.3}$$

where the correlated error terms have been transformed by subtraction, leaving only the white noise term ($\nu_t = \epsilon_t - \rho_1 \epsilon_{t-1}$). This transformation of the data (y) and model (h) using an AR(1) model of the residual error terms is the Cochrane-Orcutt method [57], which has been used in several studies [58, 59, 60] to remove serial correlations in fNIRS analysis. This method can easily be generalized to any AR model order [61] as follows:

$$\epsilon_t = \rho_1 \epsilon_{t-1} + \rho_2 \epsilon_{t-2} + \ \ldots \ + \rho_P \epsilon_{t-P} + \nu_t \tag{5.4a}$$

$$f = [1 \quad -\rho_1 \quad -\rho_2 \quad \ldots \quad -\rho_P]^T \tag{5.4b}$$

$$(f * y_t) = (f * h_t) + \nu_t \ . \tag{5.4c}$$

In practice, the AR coefficients can be estimated by fitting an AR model to the residual errors (ϵ_t) themselves. The optimal AR model order should be sufficient to remove serially correlated errors without overfitting. The model order can be chosen objectively by minimizing an information criterion function. For example, the Bayesian information criterion (BIC) [62] function is

$$BIC(P) = -2 \ LL + P \ \ln(n) \ , \tag{5.5}$$

where P is the model order; LL is the log-likelihood of the model fit; and n is the number of time points.

In the context of fNIRS brain imaging, a linear model of the evoked response [63] can be written as

$$y = X\beta + \epsilon \ , \tag{5.6}$$

where X is the design matrix, and β is the estimate of the magnitude of brain activity. In the case of a finite impulse response (FIR) model, X is given by the convolution matrix of a series of delta functions describing the timing of the stimulus onsets [34]. The coefficients (β) then describe the magnitude of the evoked hemodynamic response at each time point. The FIR model is equivalent to block averaging in the case of long inter-stimulus intervals or deconvolution in the case of closely spaced inter-stimulus intervals [64]. Note that boxcar basis functions describing the whole duration of the task can alternatively be used in FIR models and are typically one option of basis function in fMRI analysis; however, we chose not to investigate this option. For canonical linear models (e.g., the statistical parametric modeling approach; SPM-NIRS [56]), X is given by the convolution of the stimulus blocks with a canonical hemodynamic response. In this case, a limited number of coefficients (β) are used to allow statistical testing of differences in brain activity (e.g., the amplitude of β) between different task conditions. In both cases, additional regressors such as the time course of systemic physiology or motion terms can also be included in the design matrix to model nuisance terms (e.g., [65]). Regardless of whether an FIR or canonical design matrix is assumed, the values of β (e.g., brain activity) can be estimated by the inversion of X in Eq. 5.6. The Gauss-Markov equation for the unbiased ordinary least squares (OLS) estimator is

$$\beta = (X^T X)^{-1} X^T y \tag{5.7a}$$

$$\mathrm{cov}(\beta) = \sigma^2 (X^T X)^{-1} \ , \tag{5.7b}$$

where $\mathrm{cov}(\beta)$ is the covariance matrix of β; σ^2 is the variance of the residual (ϵ); and the superscript T denotes the transpose. The linear model (Eq. 5.6) can be corrected for serially correlated errors by pre-whitening with the filter f generated via Eq. 5.4b giving the expression

$$Fy = FX\beta + F\epsilon \ , \tag{5.8}$$

where F is the convolution matrix of f and performs column-wise filtering of the measurements

in y and of the regressors in X, leading to whitened residuals ($F\epsilon$). The least squares solution to this model is

$$\beta = (X^T F^T F X)^{-1} X^T F^T F y \tag{5.9a}$$

$$\text{cov}(\beta) = \sigma^2 (X^T F^T F X)^{-1} \ . \tag{5.9b}$$

As a practical note, the matrix F is approximately the size of the vector y in both dimensions. This is often too large to form explicitly; however, the matrix F is sparse with only entries of the filter coefficients on the diagonals, which can be implemented as a sparse matrix. A more efficient implementation is to employ digital filtering methods as discussed in section 5.3.2.

The methods above can correct for serial correlations due to physiology; however, motion artifacts also affect the error terms by producing outliers to a normal distribution. In this work, we propose to use iteratively reweighted least squares [66] to deal with outliers caused by motion. In this approach, the influence of each time point is weighted based on the value of the residual by a weighting function, such as Tukey's bisquare function [67] given by

$$w(r) = \begin{cases} \left(1 - \left(\frac{r}{\sigma\kappa}\right)^2\right)^2 & |\frac{r}{\sigma}| < \kappa \\ 0 & |\frac{r}{\sigma}| \geq \kappa \ , \end{cases} \tag{5.10}$$

where κ is the tuning parameter with a default value of 4.685 that preserves 95% statistical efficiency in the case of normally distributed residuals (i.e., no outliers). Adjusting the tuning parameter based on statistical efficiency gives an objective criteria for determining the tuning parameter. For example, the tuning parameter could be decreased to the point of maintaining 85% statistical efficiency if more robustness against outliers is desired. The weighted least squares (WLS) solution is

$$\beta = (X^T F^T W F X)^{-1} X^T F^T W F y \tag{5.11}$$

where W is diagonal matrix of weights calculated from the filtered residuals as follows:

$$[W_{ii}] = w\left([Fy - FX\beta]_i\right) \ . \tag{5.12}$$

Regression is done iteratively, updating the weight matrix W with each iteration until a convergence criterion is reached. As a practical note, robust regression is implemented as part of the statistics toolbox in Matlab (Mathworks R2012b, Natick MA) as the function "robustfit". The iteratively reweighted least squares estimator has an asymptotic covariance matrix given by

$$\text{cov}(\beta) = \sigma^2 \ \frac{E[\psi^2(F\epsilon/\sigma)]}{E[\psi'(F\epsilon/\sigma)]^2} (X^T F^T F X)^{-1} \ , \tag{5.13}$$

where E denotes expection, and ψ is the influence function [68], which can be specified as $\psi(r) = r\ w(r)$.

After regression, the null hypothesis that the hemodynamic response was zero (e.g., $\beta = 0$) over a given time window or set of regressors can be tested by defining a contrast vector (c) and calculating the t-statistic given by the expression

$$t = \frac{c^T \beta}{\sqrt{c^T \mathrm{cov}(\beta) c}} \ . \tag{5.14}$$

In the case of an FIR (deconvolution or block averaging) model, the contrast vector might be of value 1 for some predefined window of time (e.g., over the expected peak of the response) and 0 otherwise. In the case of the canonical design matrix, the contrast vector would be 1 for the column of the design matrix representing the regressor (task condition) of interest. A contrast vector can also be defined using positive and negative terms to test differences between two conditions.

5.3.2 Summary of algorithm

For each fNIRS channel:

1. Initialize β via an OLS fit (Eq. 5.7a).
2. Fit the residual $(y - X\beta)$ to an AR(P) model where P minimizes BIC (Eq. 5.5).
3. Generate the whitening filter f via Eq. 5.4b.
4. Apply the whitening filter to the data y and column-wise to the design matrix X.
5. Perform iteratively reweighted least squares (IRLS).
   a. Solve for β by WLS (Eq. 5.11a).
   b. Recalculate weight matrix W via Eq. 5.12.
   c. Repeat step 5a-b until changes in β are sufficiently small (e.g., $< 1\%$ change).
6. Repeat steps 2-5 until changes in β are sufficiently small (e.g., $< 1\%$ change).

Note that it is much more computationally efficient to perform the filtering in step 4 via a digital filtering algorithm, such as the "filter" function in Matlab, rather than explicitly forming the convolution matrix F. The filtered data and design matrix can then be passed to any software implementation of IRLS, such as the "robustfit" function in Matlab.

There are many approaches to estimating the AR model coefficients. The current default in Matlab is to minimize the squared prediction errors of the forward and reversed signals. Because motion artifacts are likely to influence the results, we modified this approach to a weighted least

squares method, in which the weighted squared prediction errors of the forward and reversed signal were minimized. This was performed as follows: (1) find the ordinary least squares solution, (2) calculate weights from the Tukey's bisquare function of the residual (i.e., Eq. 5.10), and (3) solve the weighted least squares problem. This approach was computationally efficient enough to perform a direct search of the AR model order that minimizes BIC. The entire algorithm ran in ∼3 s for the canonical regression model and ∼20 s for the deconvolution model, which required a much larger design matrix to invert, for one subject's data (24 channels, ∼1500 data points/channel) on a single core of a 2.9 GHz Intel Xeon E5-2690 CPU.

5.3.3 Simulated data

In order to test the performance of our proposed method under controlled noise structures, we first applied the method to synthetic data, in which noise, motion artifacts, and evoked response were simulated. We simulated serially correlated noise via tools in Matlab's Econometrics toolbox with an AR(5) model resulting in a signal with standard deviation of 0.05 μM, which was comparable to the real data set discussed in the next section. The AR model order of 5 used for simulated data was close to the median optimal model order of 6 for the experimental data. The AR coefficients were taken as the median values across subjects from an AR(5) model fit to the experimental data. Two sets of AR coefficients were used in the simulations based on AR(5) model fits to the HbO_2 and Hb channels, respectively. Half of the data were simulated using the HbO_2 AR coefficients, and half of the data were simulated using the Hb AR coefficients.

Simulations were performed with and without simulated motion artifacts. Data that were simulated with motion artifacts contained either 5-10 spike artifacts or 1-3 shift artifacts at random times. The spike artifacts were modeled with a Laplace distribution function given by

$$f(t) = A \exp\left(-\frac{|t - t_0|}{b}\right) , \tag{5.15}$$

with random peak amplitude, A, of 0.25-1μM and random scale parameter, b, of 0-1.5 s. Shift artifacts were modeled as a random positive or negative change in DC value of 0.125-0.5 μM with a linear transition lasting between 0.25-1.5 s. All random parameters described above were drawn from uniform distributions. In order to quantify the performance of the various regression methods, a known simulated evoked response was added to a subset (50%) of the channels. After regression, a receiver operating characteristic (ROC) analysis was performed to quantify the true positive rate (sensitivity) as a function of false positive rate (1-specificity). We simulated both a short

duration task consisting of 15 trials of 1s stimuli every 20s and a long duration task of 10 trials of 10s stimuli every 30 s. Evoked responses ranging from 0.01-0.10 μM in peak amplitude were generated by convolving the stimulus design with the canonical hemodynamic response function and added to the simulated noise. Evoked responses were added at half magnitude to simulated deoxy-hemoglobin channels ($\Delta[\mathrm{Hb}] = \Delta[\mathrm{HbO_2}]/2$). We simulated >100,000 random channels of data at each magnitude of evoked response with exactly half containing an evoked response.

5.3.4 Experimental data

In addition to the completely synthetic dataset, we used experimental "resting state" data from a study involving 22 normal, healthy children (3-5 years old) as a source of real physiological noise and motion artifacts. All subjects provided written parental informed consent, and this data was collected as part of a larger study of functional brain activity [69]. Each "resting state" scan lasted approximately three minutes and was acquired while the children watched a short video on the computer (Disney films). Although this is not true resting state, there were no specific cued tasks during the scan, thus serving as an effective estimate of background physiology for the purpose of this study. The experimental data were acquired at 690 nm and 830 nm wavelengths at a sampling rate of 4Hz with a probe consisting of 24 source-detector measurements over the prefrontal cortex. The optical density changes were converted to oxy- and deoxy-hemoglobin prior to input into the analysis method via the modified Beer-Lambert law. No other preprocessing was performed.

In order to test the performance of the various regression methods, a known simulated evoked response was added to the experimental "resting state" data on a subset of the channels (50%), and an ROC analysis was performed. Evoked responses were generated using the event-related (1 s on, 19 s off, 15 trials) and block design (10 s on, 20 s off, 10 trials) paradigms. Each channel of data was concatenated with itself in order to accommodate the length of the experimental designs (300s). We simulated evoked responses with amplitudes ranging from 0.01-0.1 μM on the oxy-hemoglobin channels. Evoked responses were added at half amplitude to the deoxy-hemoglobin channels. For each of the 22 subjects, we simulated 200 trial data sets (>100,000 channels), in which exactly half (chosen randomly) of the source-detector pairs contained an added evoked response in order to perform ROC analysis.

5.3.5 Analysis methods

We tested the performance of the proposed AR(P)-IRLS algorithm as well as OLS with and without AR(1) pre-whitening. Additionally, we tested wavelet based motion correction [53] followed by OLS regression (Wavelet-OLS below) and spline interpolation based motion correction [52] followed by OLS regression (Spline-OLS below) in order to validate the performance of the proposed method's ability to correct motion artifacts. The wavelet based motion correction was implemented using matlab function "hmrMotionCorrectWavelet" that is included in the HOMER2 software package (www.nmr.mgh.harvard.edu/DOT/resources/software.html) using an interquartile range of 1.5, as suggested in the function's documentation. The spline based motion correction was implemented using the functions "hmrMotionCorrectSpline" and "hmrMotionArtifactByChannel" in HOMER2. The parameters for this method were set to AMPThresh = 0.5, tMotion = 0.5s and tMask = 2s following reference [55]. The optimal parameter for SDThresh varied from 12-20 in reference [55] depending on the subject, thus we set SDThresh = 16. Receiver operating chararcteristic (ROC) curves were generated for each of the tested methods by varying the estimated p-value threshold for activation from 0 to 1 and calculating the true positive rate (sensitivity) and false positive rate (1-specificity). Partial area under the ROC curve ($AUC_{0.05}$) was used as a metric for performance, in which the true positive rate vs false positive rate curve is integrated up to a false positive rate of 0.05. In this case, a random estimator would result in $AUC_{0.05} = 0.00125$, and a perfect estimator would result in $AUC_{0.05} = 0.05$. Partial AUC is potentially a better indicator of overall performance than AUC, which integrates the entire curve, since the threshold for statistical significance is often set to 0.05 or less. Plots of false positive rate as a function of estimated p-value were generated and examined to evaluate control of type I errors (false positive rate). We estimated standard errors of $AUC_{0.05}$ via bootstrap resampling of the data 1,000 times with replacement and calculating the mean and standard deviation of 1,000 estimates of $AUC_{0.05}$.

5.4 RESULTS

The AR model based pre-whitening filters removed serially correlated errors in the optical data. In Fig. 5.1(a), an illustrative example of a simulated fNIRS signal with a few spike artifacts and a shift artifact is shown. Figure 5.1(b) shows the same data after pre-whitening with an AR(2) model

(determined optimal by BIC) generated from Eq. 5.4(b). Figure 5.1(c) shows the autocorrelation function of the original (Fig. 5.1(a)) and whitened (Fig. 5.1(b)) signals, in which the whitened signal showed significantly reduced signal autocorrelations. After filtering, the simulated artifacts were visually identifiable as outliers in the whitened signal. These time points are subsequently given little or zero weight during the iteratively reweighted least squares regression. Similarly, an illustrative example of an experimental fNIRS signal is shown in Fig. 5.1(d). After filtering with an AR(2) model (determined optimal by BIC), the whitened signal (Fig. 5.1(e)) showed significantly reduced autocorrelations (Fig. 5.1(f)). For the experimental data in this study, the lower quartile, median, and upper quartile of the AR model order chosen to minimize BIC were 5, 7, and 9 for HbO_2 channels and 3, 5, and 8 for Hb channels. In order to briefly test the model order dependence on sampling rate, we downsampled (without filtering) the experimental data to 4/5 Hz, 1Hz, 4/3 Hz, and 2 Hz. We observed that the median optimal model order increased with increasing sampling rate.

Figure 5.2 shows example hemodynamic response functions recovered via deconvolution analysis for the block task (a-c) and event task (d-f). These examples used the experimental data as a baseline signal with a simulated evoked response of 0.04 μM amplitude. The first column (Fig. 5.2(a,d)) shows examples when hemodynamic response function produced by OLS appears to be free of artifacts. In this case, the hemodynamic response functions produced by all methods appeared to be of high quality. The middle column (Fig. 5.2(b,e)) shows examples when the hemodynamic response recovered by OLS appeared to be mildly contaminated by motion artifacts. In this case, Wavelet-OLS and AR(P)-IRLS completely removed the suspected artifacts, while Spline-OLS provided partial attenuation of the artifacts. The last column (Fig. 5.2(c,f)) shows examples, in which the hemodynamic response recovered by OLS was severely corrupted by artifacts and/or noise. Wavelet-OLS and AR(P)-IRLS showed significant improvement in the visual appearance of the recovered hemodynamic response, while Spline-OLS failed to improve the results visually.

Figure 5.3 shows the results of ROC analysis of the deconvolution model performance for the block task (Fig. 5.3(a)) and event tasks (Fig. 5.3(b)). The data is shown for simulated evoked responses of 0.04 μM amplitude. In the case of synthetic data (AR(5) process) with no simulated motion artifacts (AR/None), the performance was similar for all methods tested with AR(1)-OLS and AR(P)-IRLS showing small, but statistically significant increases in $AUC_{0.05}$ over OLS for both the block and event task. In the case of synthetic data with simulated spike artifacts(AR/Spike),

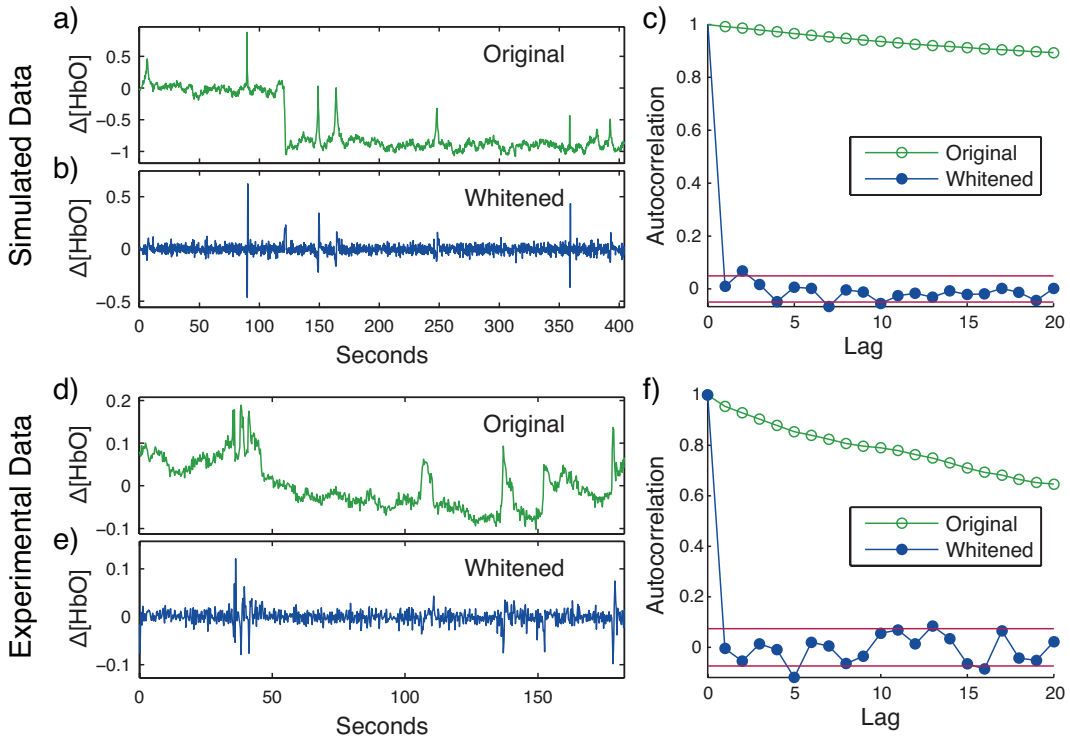

Figure 5.1: A simulated fNIRS signal generated from an AR(5) process with simulated motion artifacts is shown in (a). After generating an optimal pre-whitening filter via fitting an AR(2) model, the whitened signal (b) has significantly reduced autocorrelations (c). An experimental fNIRS signal is shown in (d). After generating an optimal pre-whitening filter via fitting an AR(2) model, the whitened signal (e) has significantly reduced autocorrelations (d).

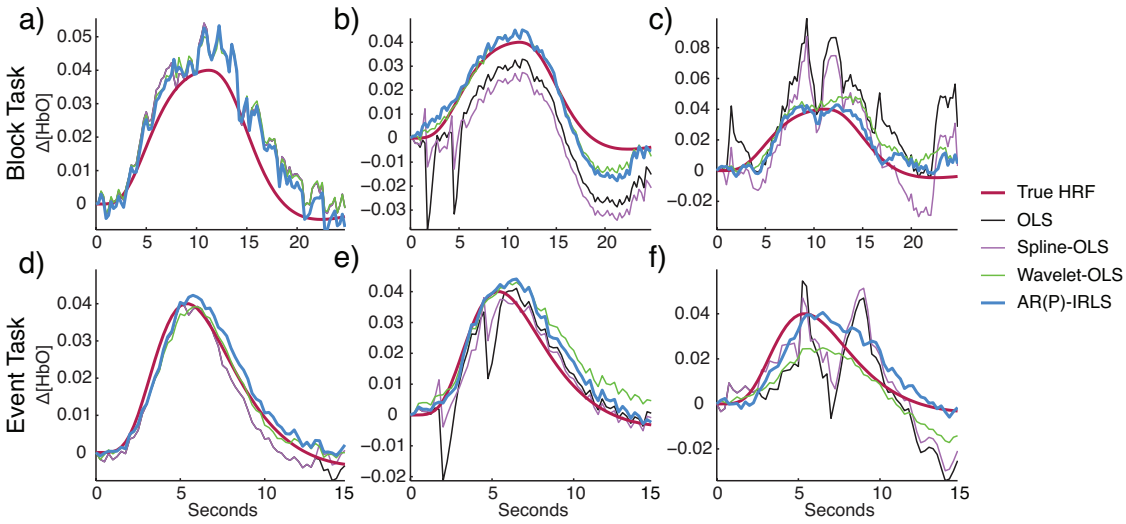

Figure 5.2: Examples of recovered hemodynamic response functions for simulated block design (a-c) and event-related (d-f) design using the experimental data as baseline physiology/noise.

AR(P)-IRLS gave the best performance, followed by Wavelet-OLS. The AR(1)-OLS results also showed a small, but statistically significant increase in $AUC_{0.05}$ over OLS for both the block and event task. For synthetic data with simulated shift artifacts (AR/Shift), AR(P)-IRLS showed a much larger performance over the other methods for both block and event tasks. The Spline-OLS method showed a small, but statistically significant increase in $AUC_{0.05}$ over OLS for both the block and event task. The AR(1)-OLS showed a statistically significant increase in performance over OLS for the event task, but not the block task. For experimental data, only AR(P)-IRLS showed a significant increase in performance over OLS.

Figure 5.4 illustrates the type I error control of OLS, AR(1)-OLS, and AR(P)-IRLS for the same data as Fig. 5.3. The type I errors for Wavelet-OLS and Spline-OLS were similar to OLS and are not shown. For all cases, OLS showed severely inflated type I errors, with false positive rates of 33-43% when the p-value was estimated to be 0.05. In other words, false positive rates were 7-8 times higher than predicted. Prewhitening with an AR(1) filter (AR(1)-OLS) significantly reduced type I errors; however, false positive rates were still slightly higher than predicted for the experimental data, in which false positive rates were 17% and 11% for the block and event task, respectively, when the p-value was estimated to be 0.05. The AR(P)-IRLS method provided excellent type I error

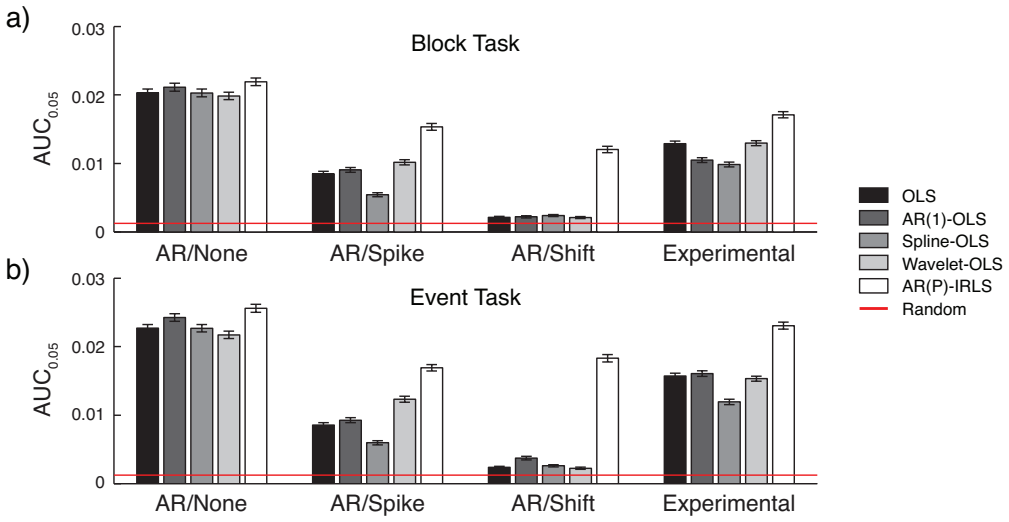

Figure 5.3: Partial AUC ($AUC_{0.05}$) for detection of evoked responses with a deconvolution/FIR model for simulated block (a) and event (b) tasks using an AR model as baseline signal with no artifacts (AR/None), spike artifacts (AR/Spike), or shift artifacts (AR/Shift) or with experimental data as a baseline signal containing motion artifacts. Error bars indicate 99% confidence interval.

control for the synthetic data with no artifacts and the experimental data for both the block and event task. For synthetic data with simulated spike or shift artifacts, AR(P)-IRLS overestimated type I errors.

Figure 5.5 shows the results of ROC analysis of the canonical regression model performance for the block task (Fig. 5.5(a)) and event tasks (Fig. 5.5(b)). The data is shown for simulated evoked responses of 0.04 μM amplitude. In the case of synthetic data with no simulated motion artifacts (AR/None), the performance was similar for all methods tested. In the case of synthetic data with simulated spike artifacts(AR/Spike), AR(P)-IRLS gave the best performance, followed by Wavelet-OLS. For synthetic data with simulated shift artifacts (AR/Shift), AR(P)-IRLS showed a large increase in performance over the other methods for both the block and event task, while AR(1)-OLS showed a small increase in performance for the block task and a moderate increase in performance for the event task. For the experimental data, AR(1)-OLS increased performance over OLS for the event task, but decreased performance for the block task. The AR(P)-IRLS method showed a moderate increase in performance over OLS for both the block and event task.

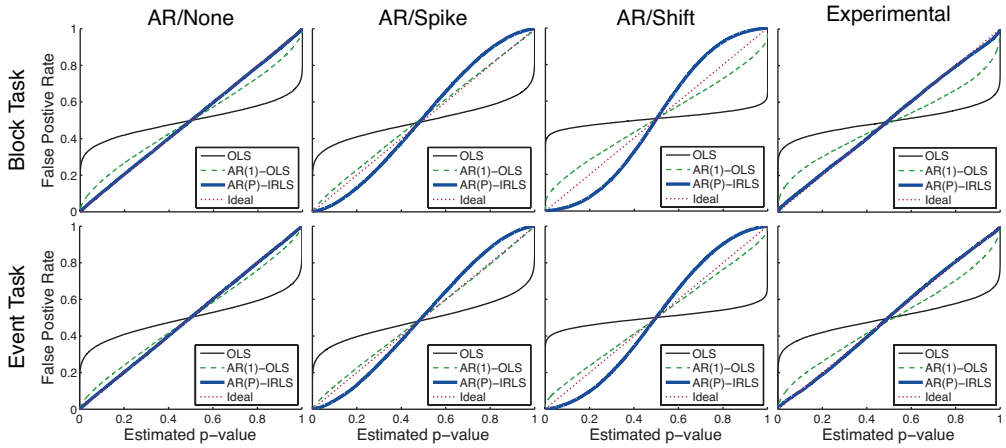

Figure 5.4: False positive rate of detection as a function of estimated p-value (i.e., estimated false positive rate) with the deconvolution/FIR model for simulated block (top row) and event (bottom row) tasks using a simulated AR model as baseline signal with no artifacts (AR/None), spike artifacts (AR/Spike), or shift artifacts (AR/Shift) or with experimental data as a baseline signal containing motion artifacts.

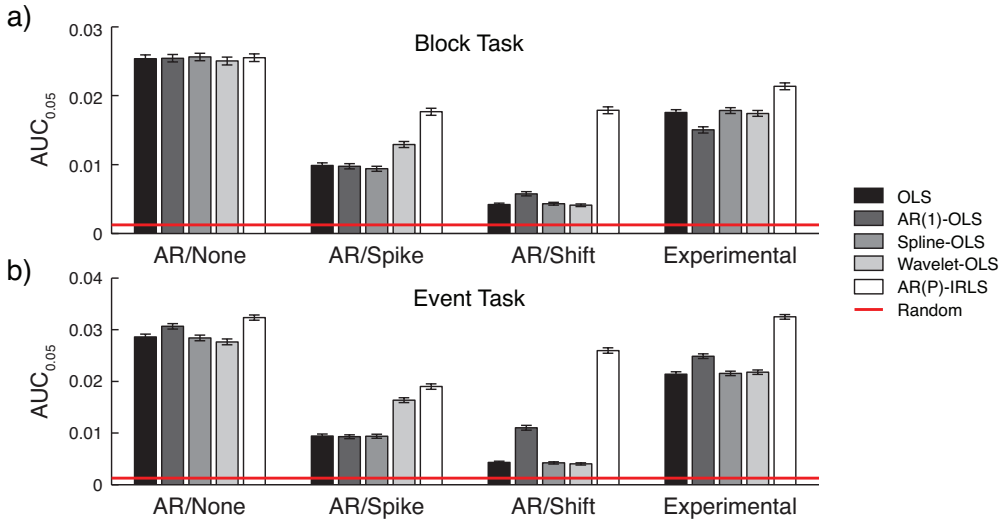

Figure 5.5: Partial AUC for detection of evoked responses with the canonical regression model for simulated block (a) and event (b) tasks using a simulated AR model as baseline signal with no artifacts (AR/None), spike artifacts (AR/spike), or shift artifacts (AR/shift) or with experimental data as a baseline signal containing motion artifacts. Error bars indicate 99% confidence interval.

Figure 5.6 illustrates the type I error control of OLS, AR(1)-OLS, and AR(P)-IRLS for the same data as Fig. 5.5. The type I errors for Wavelet-OLS and Spline-OLS were similar to OLS and are not shown. For all cases, OLS showed severely inflated type I errors, with false positive rates of 32-38% when the p-value was estimated to be 0.05. Prewhitening with an AR(1) filter (AR(1)-OLS) significantly reduced type I error estimation. The AR(P)-IRLS method provided slightly better type I error estimation than AR(1)-OLS for the synthetic data with no artifacts or with spike artifacts. For the case of synthetic data with shift artifacts, the AR(P)-IRLS method overestimated type I errors. For the experimental data, AR(1)-OLS and AR(P)-IRLS performed similarly in terms of type I error estimation.

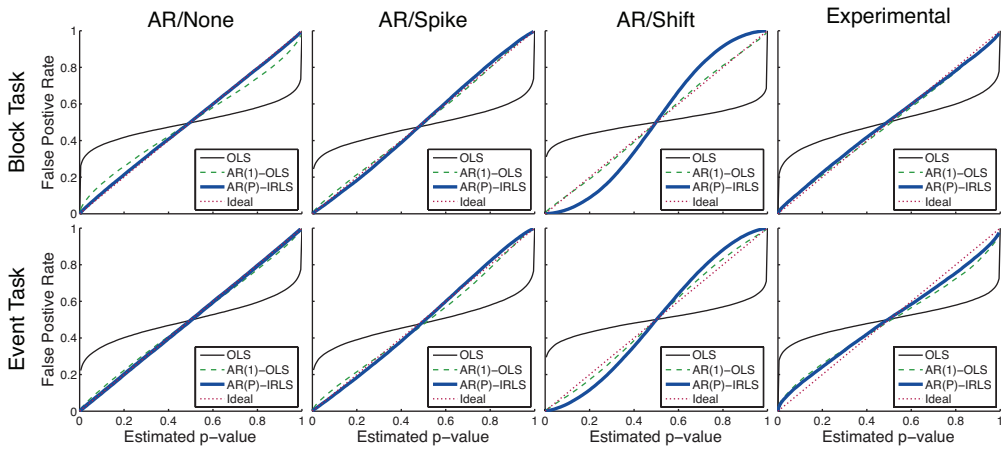

Figure 5.6: False positive rate of detection as a function of estimated p-value (i.e., estimated false positive rate) with the canonical regression model for simulated block (top row) and event (bottom row) tasks using a simulated AR model as baseline signal with no artifacts (AR/None), spike artifacts (AR/spike), or shift artifacts (AR/shift) or with experimental data as a baseline signal containing motion artifacts.

The results shown in Figs. 5.3-5.6 were for one magnitude of evoked response ($\Delta[HbO_2]$ = 0.04 μM, $\Delta[Hb] = 0.02\mu M$). We tested a range of evoked response magnitudes ($\Delta[HbO_2]$ = 0.01-0.10 μM). In general, the false positive rates were not dependent on the magnitude of the evoked response, but on the underlying noise structure. The gain in performance ($AUC_{0.05}$) by using AR(P)-IRLS over OLS was dependent on the amplitude of the evoked response, or more specifically the contrast to noise ratio (CNR), in which all methods approach random performance ($AUC_{0.05}$ = 0.00125) as CNR decreases and ideal performance ($AUC_{0.05} = 0.05$) as CNR increases. In general,

correcting for motion artifacts will offer the most benefits in the middle range of CNR. The CNR of a typical NIRS experiment will vary greatly by experimental paradigm, number of trials, and design and location of the probe; however, for all of the simulations tested in this work, the $AUC_{0.05}$ for AR(P)-IRLS was greater than or equal to $AUC_{0.05}$ of OLS.

5.5 DISCUSSION

In this study, we demonstrated a general algorithm for solving the GLM in the context of deconvolution (FIR) and canonical regression models for fNIRS that combines two well established statistical methods: AR model based data transformations (filtering) and iteratively reweighted least squares. These techniques were combined in a simple, computationally efficient algorithm to correct for two major sources of confounding noise in fNIRS analyses: serial correlations caused by systemic physiology and large outliers caused by motion artifacts, respectively. Furthermore, we rigorously tested the algorithm by performing ROC analysis using synthetic data, in which serial correlations, motion artifacts, and evoked responses could be controlled via simulations. Finally, we validated our simulation results by using experimental data as a source of real baseline physiological noise and motion artifacts.

Although this approach to pre-whitening via an AR model based transformation is common practice in linear regression, this exact approach is not widely used in neuroscience applications. In fMRI analysis (which typically deals with data sets on the order of 64x64x30 = 122,880 voxels) the estimation of an AR model for each voxel is not practical due to the high computational time required. For example, in the fMRI analysis program SPM8 [63] a global estimate of an AR(1) model is included in the parameterization of the covariance matrix in the context of restricted maximum likelihood (ReML) rather than fitting each voxel independently. In fMRI analysis, this approximation is justified because the time between subsequent measurements is much longer ($\sim$2-3 s) than fNIRS, such that serial correlations are less of a concern. In the case of fNIRS data, which has both higher sample rates and lower number of time series measurements, these approximations are no longer appropriate.

The use of simulated AR noise with simulated artifacts allowed us to control the type, number, and amplitude of motion artifacts. The simulated artifacts were relatively large compared to experimental data and provided a good test of the AR(P)-IRLS method's ability to correct for motion

artifacts. The AR(P)-IRLS method outperformed spline interpolation based motion correction [52] and wavelet based motion correction [53] methods when motion artifacts were present. Despite showing visual improvements in the recovered hemodynamic response functions, such as in Fig. 5.2, Wavelet-OLS and Spline-OLS did not offer any statistical advantage in the ROC analysis with the experimental data. It is possible that the parameters used for these methods were not optimal for the experimental data set in this study. Further ROC analyses should be performed for data collected under a wide range of experimental conditions and subject populations to validate and generalize the comparison of these methods.

In simulations without artifacts the algorithm did not negatively affect the analyses. The practical implication of this is that the algorithm can be applied to every data set without making a subjective judgment about whether artifact correction is needed or not. The method will improve performance when data is contaminated by motion and preserve normal performance when data are free of artifacts. Overall, our results suggest that application of robust regression methods after pre-whitening represents a reliable method for correction of motion artifacts.

An AR(1) model of the errors was insufficient for controlling type I errors in some cases. This effect is likely to be a greater issue at higher sampling rates than in this study (>4Hz). Using an adaptive AR model order for pre-whitening is simple to implement and computationally efficient enough to be added to standard fNIRS analysis methods to improve type I error control.

For the deconvolution model, AR(P)-IRLS method provided accurate estimation of false positive rates for the synthetic data with no artifacts and the experimental data, while overestimating type I errors for synthetic data with simulated spike or shift artifacts. For the canonical regression model AR(P)-IRLS method provided accurate estimation of false positive rates for the synthetic data with no artifacts or spike artifacts and the experimental data, while overestimating type I errors for synthetic data with shift artifacts. While it is potentially better to overestimate than underestimate type I errors, this may lead to reduced sensitivity near the threshold of statistical significance (estimated p-value < 0.05). This overestimation is possibly related to violation of stationariy (assumed by AR models) caused by severe motion artifacts, especially shift artifacts, or to the breakdown of the asymptotic covariance estimate in Eq. 5.13. This issue did not appear to be a problem for the simulations using experimental data with real motion artifacts, in which the estimated p-values were relatively accurate. The statistics may potentially be improved if shift artifacts can be removed or identified during preprocessing.

5.6 CONCLUSIONS

In conclusion, we have developed a general algorithm for both the deconvolution (FIR) and canonical regression analysis models that is robust to two major sources of noise in fNIRS: systemic physiological signals and motion artifacts. The algorithm preserves the performance of standard OLS methods when data are free of motion artifacts, thus freeing the user from making a subjective choice about artifact correction. Lastly, the algorithm contains a single tuning parameter for the weighting function used in IRLS that can be set objectively.

6.0 ROBUST ADAPTIVE ESTIMATION OF EVOKED HEMODYNAMICS

The work in chapter 5 made significant progress in mitigating the effects of systemic physiology and motion on the estimation of evoked brain activity and control over false positives; however, the algorithm presented in chapter 5 is not suitable for real-time data analysis. This chapter extends the same concepts of prewhitening and robust regression to mitigate the effects of systemic phyiology and motion artifacts in order to modify the Kalman estimator. The resulting algorithm is suitable for adaptive estimation in real-time.

6.1 ABSTRACT

Two majors sources of noise in functional near-infrared spectroscopy (fNIRS) are systemic physiology and motion artifacts. These sources of noise manifest as serial correlations and outliers, respectively, which can inflate false positive rates and reduce sensitivity of detecting evoked hemodynamic activity. In previous work, we showed that these sources of noise can be mitigated via application of autoregressive (AR) model based pre-whitening followed by the application of iterative re-weighted least squares (IRLS). In this work, we extend these ideas to modifications of the linear Kalman filter to develop an algorithm for adaptive estimation that is robust to systemic physiology and motion artifacts and can be applied in real-time. We evaluated the performance of the proposed method via simulations of evoked hemodynamics that were added to real resting-state data, which provided realistic fNIRS noise. Lastly, we applied the method post-hoc to a choice reaction time (CRT) task data set. The method showed very similar performance to the analogous offline method, in which both methods show better control over false positive and higher sensitivity to detection of brain activity that ordinary least squares (OLS) methods.

6.2 INTRODUCTION

Near-infrared spectroscopy (NIRS) is a non-invasive technique that can monitor changes in the optical absorption of cerebral blood to detect evoked brain activity [36]. Measurements are made by an array of light sources and detectors that are coupled to the scalp through fiber optics between a head cap worn by the subject and the NIRS instrument. Spatially overlapping measurements that are made at multiple wavelengths within the optical window (650-900 nm) can allow for spectroscopic estimation of both oxy-hemoglobin (HbO_2) and deoxy-hemoglobin (Hb) via the modified Beer-Lambert law [16]. The nature of the evoked changes in NIRS have been shown to be related to the blood oxygen level dependent (BOLD) signal of functional magnetic resonance imaging (fMRI) [34]. Compared to fMRI, functional NIRS (fNIRS) offers lower spatial resolution, but much higher temporal resolution (>10 Hz). This characteristic makes fNIRS suitable for studying the temporal characteristics of the hemodynamic signal. Furthermore, fNIRS is non-restraining, making it suitable for infants and small children and for various tasks, such as walking [7, 8], balance [9, 10, 11], and social interaction [12], where fMRI is not practical.

Two major sources of confounding noise that affect the analysis and interpretation of fNIRS signals are serially correlated errors due to systemic physiology, such as cardiac, respiratory, and low frequency Mayer waves (related to blood pressure auto-regulation), and motion artifacts due to the movement or slippage of the head cap. Both of these sources of noise violate assumptions of the general linear model (GLM) and can contribute to inaccurate control of type I error (false positives) and reduced performance of the GLM estimator. In a previous publication, we have shown that the effects of these sources of noise on the regression model can be dealt with by incorporating autoregressive (AR) based filtering and robust regression methods in an iterative offline algorithm [51]. The algorithm is simple conceptually and was shown to be robust to the effects of motion and systemic physiology.

Adaptive methods offer advantages over static offline methods in that they can be used for processing in real time, in which the parameters of the model are updated as data is acquired. Potential applications of real-time imaging include the development of brain machine interfaces [70, 71], monitoring attentional states (e.g., [72]), providing bedside feedback in clinic (e.g., [73]), and the investigation of neurofeedback [74].

In this study we extended the ideas of [51] to develop an adaptive algorithm based on the linear Kalman filter. We validated the method by performing receiver operating characteristics

(ROC) analysis on simulations using simulated evoked hemodynamics added to real resting-state NIRS data. The resting-state NIRS data acted as real noise with contributions from physiology, motion, and instrument noise. Lastly, we applied the proposed method post-hoc to a choice reaction time (CRT) task dataset. Overall, the algorithm offers adaptive estimation of fNIRS data that is suitable for real-time application and is robust to serial correlations from physiology and outliers from motion.

6.3 METHODS

6.3.1 The AR-IRLS Approach

A common approach to analyzing fNIRS data implements a general linear model (GLM) given by

$$y = X\beta + \epsilon \ , \tag{6.1}$$

where y is a vector containing the preprocessed fNIRS time-series measurement; X is the design matrix with each column containing a regressor; β is a vector of parameters to be estimated; and ϵ is the residual error. The contents of design matrix X will vary depending on the desired model to be estimated. One approach that is commonly used is to first create a stimulus matrix with blocks (of value 1) marking the presence of a task. The stimulus matrix is convolved with a canonical hemodynamic response function to provide a predicted hemodynamic signal for each stimulus. The magnitude of the response to each stimulus condition is then given by the estimated coefficients β. Another approach uses a finite impulse response (FIR) basis set, in which the onset of a task and a predetermined number of lags are marked by delta functions. The resulting coefficients in β give the hemodynamic response function.

As written, the error term ϵ in Eq. 6.1 typically contains physiological "noise" and potentially motion artifacts, making a standard ordinary least-squares estimator inappropriate due to the presence of serial correlations and outliers. In [51], this model is modified by prewhitening with a linear filter F, represented as a matrix notation as

$$Fy = FX\beta + F\epsilon \ , \tag{6.2}$$

where F is a convolution matrix that simply performs column-wise FIR filtering based on an auto-regressive (AR) model of the error terms. The new residual errors $F\epsilon$ are decorrelated, but still

contain outliers due to motion. To deal with motion artifacts, Eq. 6.2 is solved via iterative reweighted least squares estimation [66], which employs a weighted least squares solution given by

$$\beta = (X^T F^T W F X)^{-1} X^T F^T W F y \ , \tag{6.3}$$

where W is a diagonal matrix containing weights determined by an appropriate weighting function, such as Tukey's bisquare function [67]. The AR-IRLS algorithm is initialized with an OLS fit of the model. Each iteration of the algorithm then proceeds as follows: (i) estimate an AR model based on residual error, (ii) calculate the whitened data vector Fy and design matrix FX, and (iii) perform iterative reweighted least squares (IRLS) on the whitened data and design matrix.

The weight matrix can be factored applied to Eq. 6.2 giving a weighted model,

$$\sqrt{W} F y = \sqrt{W} F X \beta + \sqrt{W} F \epsilon \ , \tag{6.4}$$

in which the square root denotes an element-wise square root applied to the weights on the diagonal of W. The estimation to Eq. 6.4 gives exactly the solution shown in Eq. 6.3, and this model is used for formulating the adaptive estimator in the following section.

6.3.2 Linear Kalman Filter

The linear Kalman filter [75] is a recursive linear estimator that solves the following model:

$$\beta\{t\} = A\{t\}\beta\{t-1\} + B\{t\}u\{t\} + q\{t\} \tag{6.5}$$

$$q\{t\} \sim N(0, Q\{t\}) \tag{6.6}$$

$$y\{t\} = X\{t\}\beta\{t\} + r\{t\} \tag{6.7}$$

$$r\{t\} \sim N(0, R\{t\}) \tag{6.8}$$

where $\beta\{t\}$ describes the "state" of the system; $A\{t\}$ is the state transition matrix; $B\{t\}$ is the control input matrix; $u\{t\}$ is the control input vector; $q\{t\}$ is the process noise with covariance $Q\{t\}$; $y\{t\}$ contains observed measurements; $X\{t\}$ is the observation matrix; $r\{t\}$ is the measurement noise with covariance $R\{t\}$. The quantities $A\{t\}$, $B\{t\}$, $u\{t\}$, $X\{t\}$, and $y\{t\}$ are known quantities, while $\beta\{t\}$ is estimated.

The estimation procedure is typically broken into two steps: (i) the prediction step and (ii) the update step. The prediction step is given by

$$\beta\{t|t-1\} = A\{t\}\beta\{t-1|t-1\} + B\{t\}u\{t\} \tag{6.9}$$

$$C\{t|t-1\} = C\{t-1|t-1\} + Q\{t\} \tag{6.10}$$

where C is the covariance matrix of β. Here the notation $\{t|t-1\}$ denotes the quantity at time t given the measurements up to time $t-1$. The process noise covariance $Q\{t\}$ is generally set *a priori*. The prediction or residual error is given by

$$r\{t\} = y\{t\} - X\{t\}\beta\{t|t-1\} \ . \tag{6.11}$$

The update step of the linear Kalman filter is given by

$$S = X\{t\}C\{t|t-1\}X^T\{t\} + R\{t\} \tag{6.12}$$

$$K = C\{t|t-1\}X^T\{t\}S^{-1} \tag{6.13}$$

$$C\{t|t\} = C\{t|t-1\} - KX\{t\}C\{t|t-1\} \tag{6.14}$$

$$\beta\{t|t\} = \beta\{t|t-1\} + Kr\{t\} \ , \tag{6.15}$$

which gives the updated "states" ($\beta\{t|t\}$) and covariance matrix ($C\{t|t\}$) given the new observations $y\{t\}$. The residual covariance matrix $R\{t\}$ can be set *a priori* if the noise characteristics are well known, or as is done in this work, estimated recursively.

6.3.3 Proposed Adaptive Algorithm

So far we have only discussed the Kalman filter in general terms. In this work, we investigated the case where β contains the coefficients of regressors in the design matrix $X\{t\}$. As such, $A\{t\}$ is an identity matrix, and $B\{t\}$ and $u\{t\}$ are eliminated. This gives

$$\beta\{t\} = \beta\{t-1\} + q\{t\} \tag{6.16}$$

$$q\{t\} \sim N(0, Q\{t\}) \tag{6.17}$$

$$y\{t\} = X\{t\}\beta\{t\} + r\{t\} \tag{6.18}$$

$$r\{t\} \sim N(0, R\{t\}) \ , \tag{6.19}$$

in which $Q\{t\}$ is effectively a tuning parameter that is set beforehand. In the case that $Q\{t\} = 0$ the Kalman filter equations reduce to recursive least squares estimation. The residual variance $R\{t\}$ is handled by modeling $r\{t\}$ as an AR process:

$$r\{t\} = \sum_{i=1}^{P} \alpha_i\{t\} \ r\{t-i\} \ + u\{t\} \tag{6.20}$$

$$u\{t\} \sim N(0, \sigma_u^2) \ , \tag{6.21}$$

in which α_i are the AR coefficients and $u\{t\}$ is normally distributed white noise. The measurements and design matrix are thusly whitened by

$$y_f\{t\} = y\{t\} - \sum_{i=1}^{P} \alpha_i\{t\} y\{t-i\} \tag{6.22}$$

$$X_f\{t\} = X\{t\} - \sum_{i=1}^{P} \alpha_i\{t\} X\{t-i\} \ , \tag{6.23}$$

which is effectively convolution with an FIR filter. Note that we have introduced an a assumption that β varies sufficiently slowly over P time steps, such that Eq. 6.23 is valid. This assumption is justifiable given the relatively slow dynamics of hemodynamic signals. The AR coefficients are estimated using a separate Kalman filter which takes the model prediction error $r\{t\}$ as observations and uses the previous P residual errors ($r\{t-1\}$ to $r\{t-P\}$) as the entries to $X\{t\}$.

The whitened model gives the following whitened prediction error:

$$u\{t\} = y_f\{t\} - X_f\{t\}\beta\{t|t-1\} \ , \tag{6.24}$$

which is used to calculate a weight value for the new data point. The weighting function used in this work is given by

$$w(u) = \begin{cases} 1 - \left(\frac{u}{\sigma\kappa}\right)^2 & |\frac{u}{\sigma}| < \kappa \\ 0 & |\frac{u}{\sigma}| \geq \kappa \ , \end{cases} \tag{6.25}$$

which is simply the square root of Tukey's bisquare function [67]. The tuning constant κ is typically set to 4.685, and σ is the standard deviation of the input u. We chose to estimate the standard deviation of the whitened model error using a recursive mean absolute deviation estimator given by

$$\sigma_u\{t\} = \frac{t-1}{t}\sigma_u\{t-1\} + \frac{1.253}{t}|u\{t\}| \ , \tag{6.26}$$

in which 1.253 is a constant relating the standard deviation to the mean absolute deviation. Thus, the final weighted and whitened prediction error and model at time t are given by

$$u_w\{t\} = w(u\{t\})\ u\{t\} \tag{6.27}$$

$$X_w\{t\} = w(u\{t\})\ X_f\{t\}\ , \tag{6.28}$$

which are fed into the update step of the Kalman filter equations giving

$$S = X_w\{t\}C\{t|t-1\}X_w^T\{t\} + \sigma_u^2\{t\} \tag{6.29}$$

$$K = C\{t|t-1\}X_w^T\{t\}S^{-1} \tag{6.30}$$

$$C\{t|t\} = C\{t|t-1\} - KX_w\{t\}C\{t|t-1\} \tag{6.31}$$

$$\beta\{t|t\} = \beta\{t|t-1\} + Ku_w\{t\}\ . \tag{6.32}$$

The entire algorithm is shown schematically in Fig. 6.1, which illustrates the relation between the two Kalman filters used for estimating the hemodynamic and AR models, respectively.

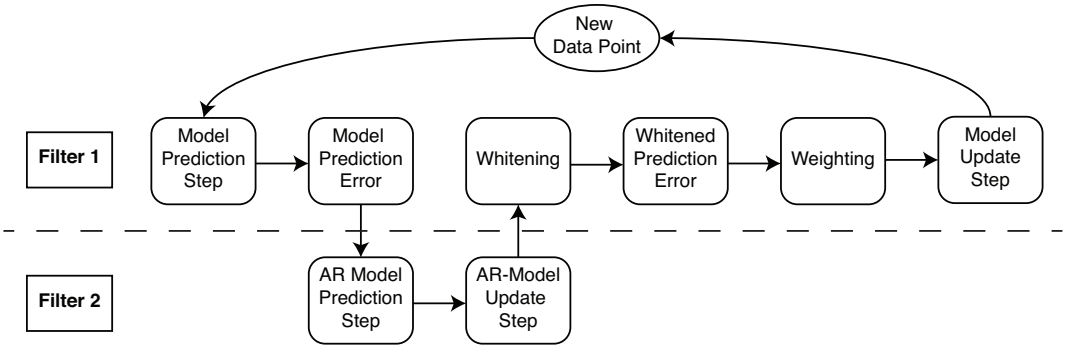

Figure 6.1: Schematic of the adaptive estimator illustrating the low of information between two linear Kalman filters. Filter 1 estimates the model and passes the prediction error to Filter 2, which estimates an AR model and passes AR coefficients to Filter 1.

6.3.4 Simulation and ROC Analysis

A resting state fNIRS data set that was acquired as part of a larger study in adults (age 18-50, N = 34) was used for simulation and evaluation of the proposed method's performance. For each subject, 5 min of resting state data were acquired at 10 Hz sampling frequency. The probe consisted of 35 source-detector pairs acquired at 690 nm and 830 nm (70 channels of data) over the motor

and somatosensory cortices. The data were converted to ΔHbO_2 and ΔHb via the modified Beer-Lambert law and low signal to noise ratio (SNR) channels were discarded. No other preprocessing was performed.

Simulations were performed by adding a simulated evoked response to the real "noise" from the resting state data. An evoked response was simulated for a task consisting of a single event every 15 s for 20 trials. A block stimulus vector was generated for this task and convolved with a canonical hemodynamic response function (HRF) and scaled based on contrast to noise ratio (CNR). We performed simulations at CNR levels of 0.5, 1.0, and 2.0, in which CNR was defined as the peak magnitude of the response divided by the standard deviation of the whitened resting state data. For each set of simulations, data were generated as follows: (i) choose a random channel of resting state data from the pool of all HbO_2 and Hb channels; (ii) add a random delay time before the start of the task periods; (iii) add a simulated evoked response to resting state data if desired; (iv) pass data and design matrix to estimators for assessment of estimated values and statistics. An equal number of simulations were performed on channels with an without adding an evoked response, such that exactly half of all simulations contained a simulated evoked response.

As benchmarks for comparison, the simulated data were also analyzed with two static offline methods: AR-IRLS [51] and OLS with AR(1) prewhitening. Comparison with OLS allowed for testing of performance gains over typical OLS-based estimators and comparison with AR-IRLS allowed for investigation of convergence with the analogous offline method. To evaluate the performance of the estimators, receiver operating characteristic curves (ROC) were generated using the t-statistic output of the estimators, in which true positive rate (TPR) is plotted vs false positive rate (FPR) as a function the t-statistic threshold for "detection" of an evoked hemodynamic response. In addition, we compared estimated p-values ($\hat{p}$) with actual false positive rates (FPR). Lastly, we looked at sensitivity, specificity, and FPR when using $\hat{p} < 0.05$ as the threshold for significance for activation. The simulations were repeated for CNR values of 0.5, 1.0, and 2.0. For estimation with the proposed adaptive method, the process noise covariance $Q\{t\}$ was set to zero and an AR(30) model was used.

6.3.5 Application to Experimental Data

We applied the proposed method to experimental data (N = 6, age 25-47) involving a choice reaction time (CRT) task with and without sway referencing as a final demonstration of the proposed

method. The task involved an arrow presented on either the left or right side of a screen that could point in the left or right direction. Subjects were given two response buttons for the left and right hands and were asked to press the button corresponding to the direction of the arrow. The paradigm included 10 blocks of 15 s of CRT task followed by 15 s of no task. During the task blocks, new arrows were presented with random direction and location immediately after responding to the previous stimulus until 15 s had elapsed. Each subject performed the task once while standing on a solid platform and once while sway referencing.

The NIRS data were acquired at 20 Hz on a Techen CW6 system using an 16 channel (8×690 nm and 8×830 nm), bilateral probe covering the frontal regions. The data were then analyzed post-hoc using the proposed adaptive method and the offline AR-IRLS method for comparison.

6.4 RESULTS

6.4.1 Simulation Results

An example of the simulated data (CNR = 1.0) is shown in Fig. 6.2(a), which contains several visible motion artifacts. Figure 6.2(b) shows the weights given to each time point. When there are sharp changes in the time-series data due to motion, the weight decrease accordingly. Figure 6.2(c) shows the predicted hemodynamic response (solid green line), which closely matches the simulated response (dashed red line). Figure 6.2(d) shows the evolution of the t-statistic, which appropriately increases as more data is acquired.

Figures 6.3(a)-6.3(e) show the ROC curves at different snapshots in time, and Figures 6.3(f)-6.3(j) show FPR as a function of $\hat{p}$. The proposed adaptive method shows similar performance to the analogous offline AR-IRLS method. Both of these methods show performance improvements over the OLS method. Figures 6.4(a)-6.4(c) show the sensitivity, specificity, and FPR using $\hat{p} < 0.05$ as a threshold for detection of an evoked response. Again the proposed adaptive method shows similar performance to the analogous AR-IRLS method for offline processing, and both methods show better sensitivity, specificity, and control over false positives.

Table 6.1 shows the sensitivity, specificity, and FPR using $\hat{p} < 0.05$ as a threshold for detection for repeated simulations at CNR values of 0.5, 1.0 and 2.0. As to be expected, specificity and FPR

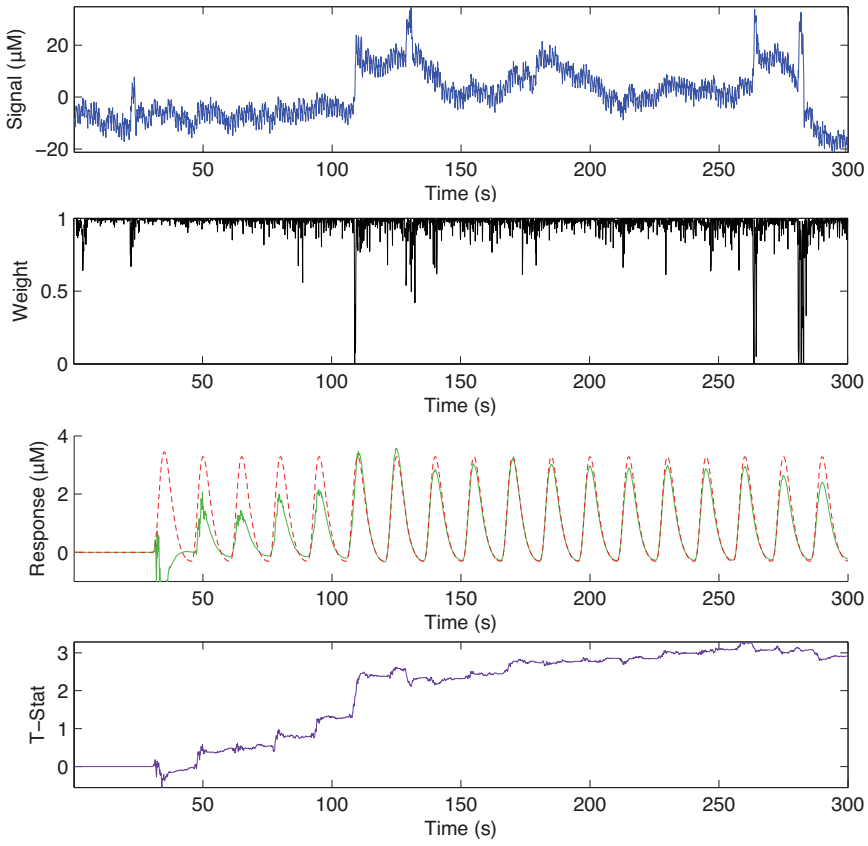

Figure 6.2: (a) An example of simulated fNIRS data from resting-state data and synthetic hemodynamic response. (b) Weights calculated by the algorithm. Artifactual time points are down weighted. (c) The predicted evoked response (solid green) is shown over the simulated evoked response (dashed red). (d) Evolution of the t-statistic over time.

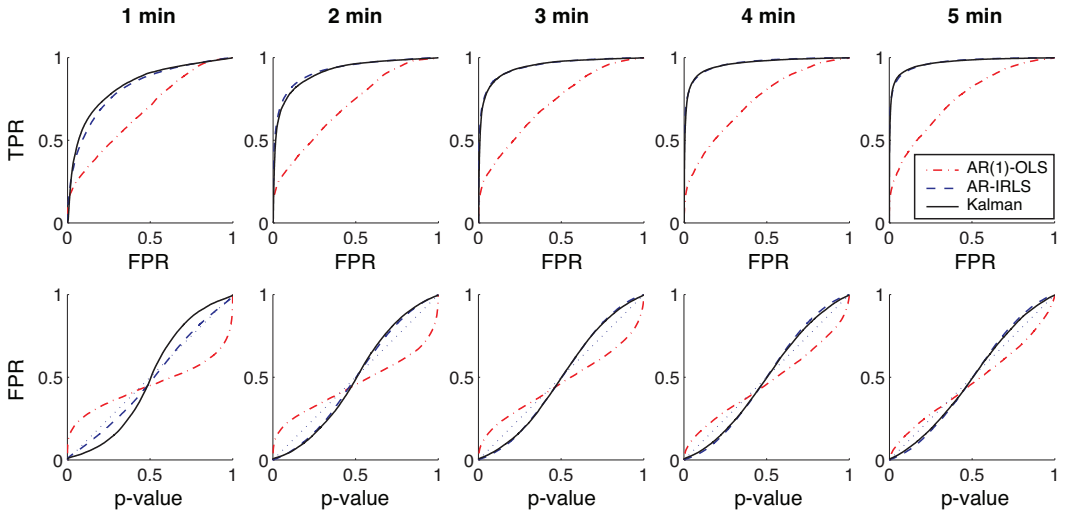

Figure 6.3: Receiver operating characteristic (ROC) curves are shown for 1, 2, 3, 4, and 5 min of data. The proposed adaptive method converges rapidly to the analogous offline AR-IRLS method.

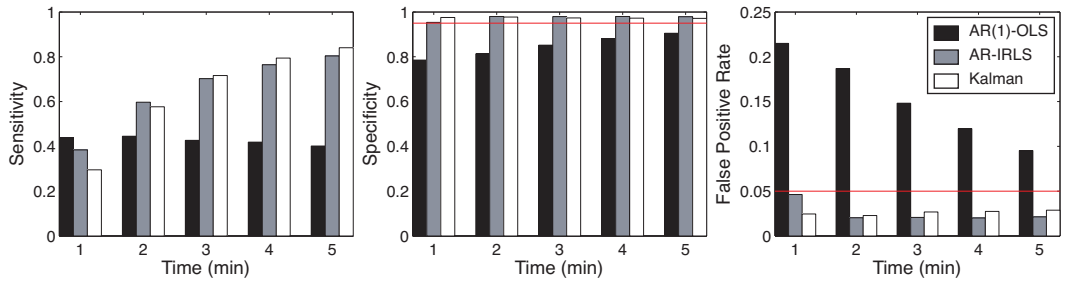

Figure 6.4: Sensitivity (a), specificity (b), and false positive rate (c) are shown for simulated data using $\hat{p} < 0.05$ as the threshold for activation.

were independent of CNR and only depend on the noise characteristics of the data. Higher CNR led to higher sensitivity to detection, especially at early time points in the data (e.g., at 1 min).

Table 6.1: Sensitivity, specificity, and false positive rate are shown for varying contrast to noise ratio (CNR) for the proposed algorithm using $\hat{p} < 0.05$ as the threshold for activation.

Time	1 min	2 min	3 min	4 min	5 min
			Sensitivity		
CNR = 0.5	10.8%	28.4%	40.1%	49.3%	56.0%
CNR = 1.0	29.5%	57.7%	71.6%	79.4%	84.0%
CNR = 2.0	57.9%	82.6%	91.7%	95.1%	96.5%
			Specificity		
CNR = 0.5	97.6%	97.9%	97.4%	97.3%	97.2%
CNR = 1.0	97.6%	97.7%	97.3%	97.3%	97.1%
CNR = 2.0	97.5%	97.7%	97.3%	97.3%	97.2%
			False Positive Rate		
CNR = 0.5	2.4%	2.1%	2.6%	2.7%	2.8%
CNR = 1.0	2.5%	2.3%	2.7%	2.7%	2.9%
CNR = 2.0	2.5%	2.3%	2.7%	2.7%	2.8%

6.4.2 Experimental Results

Figure 6.5 shows an example of the channel-wise t-statistic evolution over time for HbO_2 for a single subject. In addition the channel-wise statistics for the offline AR-IRLS are shown. The t-statistics showed relatively quick convergence, with not much visible difference between the estimates at 2 min and 5 min. The online channel-wise t-statistics at the end of the scan (5 min) were visibly similar to the results obtained from AR-IRLS.

Figure 6.6 shows a scatter plot of all channel-wise t-statistics at the end of scan from all subjects for HbO_2 for the proposed method vs. AR-IRLS. In addition, a total least squares regression line is shown. The proposed online method shows good agreement with the analogous offline method, although a few points show a large deviation from the trend. It is unclear what the explanation is for this result, other than the obvious differences in the estimation procedures. The slope of the regression line suggests there are no systematic differences between the two estimators.

Figure 6.7 shows the results for group level analysis using the subject level results from the proposed online method as well as the offline AR-IRLS method. Both methods show similar patterns of activation for HbO_2, in which activation was primarily seen on the right frontal region for the CRT task under both the fixed platform and sway referencing conditions. This is consistent lesion studies showing the right dorsolateral prefrontal cortex to affect performance in Stroop tasks

[76] and with fMRI findings showing bilateral activation in the frontal areas [77]. There was no statistically significant differences detected for performing the task while sway referencing that might have been expected from dual task interference.

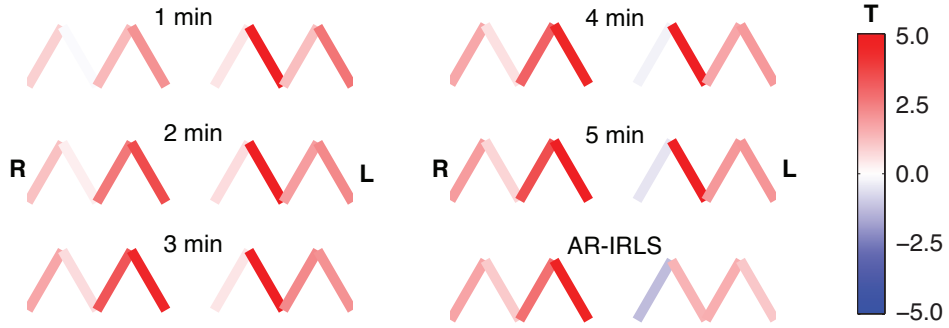

Figure 6.5: T-statistic evolution for HbO_2 for an example subject at 1 min intervals and T-statistics from offline analysis via AR-IRLS (bottom). R = right; L = left; T = T-statistic.

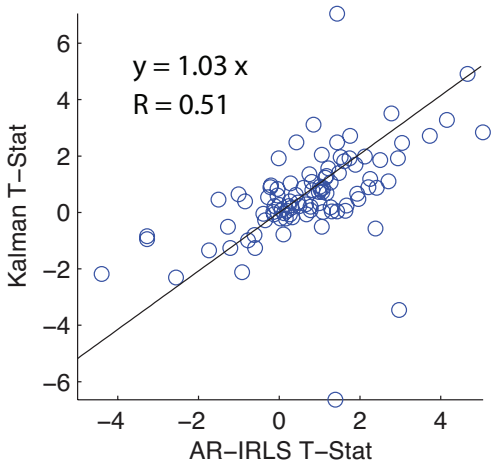

Figure 6.6: Comparison of T-statistics for offline (AR-IRLS) and online analysis methods across all channels of HbO_2 for all subjects using the full time-series data.

6.5 DISCUSSION

In this study, we have developed methods for adaptive estimation of the GLM based on using two Kalman filters: one to estimate the model and one to estimate an AR model of the residual

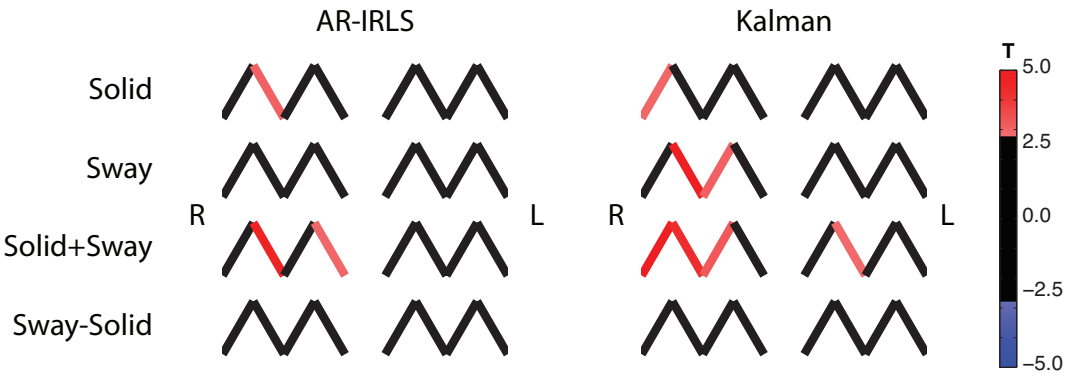

Figure 6.7: Group level statistics for HbO_2 using subject level statistics from the offline (AR-IRLS) and online analysis methods. Black lines indicate failure to reject the null hypothesis at $p < 0.05$ (uncorrected).

error. Before the update step of the first Kalman filter, the model is whitened based on the AR coefficients of the second Kalman filter and weighted by a weighting function. This mitigates the effects of serial correlations and outliers on the estimator. The proposed method was compared to an analogous offline algorithm that implements the same concepts. The proposed online method showed very similar performance to the analogous AR-IRLS method for offline processing. Lastly, we demonstrated the method on an experimental data set, in which the online and offline methods showed good agreement.

One significant difference between the online and offline algorithms is that the AR-IRLS method employs a model selection step using Bayesian information criteria (BIC) [62] to choose an optimal AR model order. However, our simulation results show that choosing an appropriate model order beforehand did not significantly degrade the performance. If model selection is desired, one can simply keep a recursive estimate of a handful of AR models and calcululate their BIC as

$$\mathrm{BIC}(P) = -t \ln\left(\sigma_r^2(P)\right) + P \ln(t) \ , \tag{6.33}$$

where P is the model order, and $\sigma_r^2(P)$ is a recursive estimate of the residual prediction error from the Kalman filter estimating an AR(P) model. For example, if the sampling frequency is 10 Hz, one could keep estimates of $P = \{1, 5, 10, 20, 30\}$ and choose the model with the lowest BIC to perform the pre-whitening at each time point.

In this work, we only tested the case where the process noise Q was set to zero in order to demonstrate the methods and compare to the analogous offline algorithm. In the case where $Q = 0$ the Kalman filter acts like an iterative least squares estimate, in which the new model estimate can be interpreted as an improved estimate of a static model. However, the Kalman filter framework allows for time-varying "states" when Q is non-zero. This may be useful for investigating inter-trial variance or for applications where the evoked response is expected to be modulated, such as by learning or habituation. One issue with attempting to model time-varying parameters is determining an appropriate process noise. If process noise is too large, the Kalman filter will overfit noise in the time-series, and if the process noise is too small, it may not capture all of the characteristics of the temporal changes in the model states. Care must be exercised in setting a non-zero process noise. Future studies should investigate objective methods for setting the process noise.

In conclusion, we developed a new method for adaptive estimation of the GLM based that is robust to motion artifacts and systemic physiology. The new method showed similar performance to the offline AR-IRLS algorithm. The method shows better performance than OLS type methods in both sensitivity and type I error control. Finally, since the method is adaptive, it is suitable for real-time analysis of fNIRS data.

7.0 CONCLUSIONS

The aim of this thesis was to develop methods for NIRS data analysis that mitigates major confounding factors in recovery of cerebral physiology and hemodynamics. Baseline physiology estimation suffers from rapidly decreasing sensitivity as a function of depth. This leads to to difficulty in separation of physiological parameters, such as oxygen saturation and hemoglobin content, from that of the superficial layers. Measurements over time suffer from high contributions of systemic physiological signals, such as cardiac, respiratory, and blood pressure waves. Furthermore, as measurements are made over an extended period of time, the subjects inevitably introduce artifacts to the time-series data when moving. These sources of "noise" degrade the performance of analyses and reduce the sensitivity of NIRS.

The most common analysis method for FD-NIRS assumes that the head is a semi-infinite, homogeneous structure. In chapter 3, we showed that this model is somewhat biased, even for a morphologically normal neonate. The attemps to used layered models to perform the recovery of S_tO_2 and HbT in chapter 4 showed some promising results suggesting that bias can be reduced by using an atlas or acquiring subject-specific anatomical information; however, the study in chapter 4 also showed that when more realistic computation of light propagation were used, the advantages of incorporating anatomical information were lost. This is possibly related to the treatment of CSF, which does not adhere to the assumptions of the diffusion approximation. Future work should confirm this hypothesis and attempt to mitigate the issue using more accurate forward model computations, either by solving the issues with stochastic noise in Monte Carlo methods or incorporating higher order spherical harmonics terms into the finite element methods.

The inverse problem in FD-NIRS in inherently ill-conditioned due to the high sensitivity of the superficial layer and high attenuation of light before it reaches the brain. Future studies can also work to improve the conditioning of this problem by optimizing the measurement procedure. In this work, we only used two wavelengths, but it is possible to make measurements at more wavelengths.

Furthermore, modulation frequency and the number of source-detector distances can also be varied. Incorporation of priors or various regularization techniques may also yield improved results. Lastly, we tested these methods in neonates, in which NIRS has substantially greater sensitivity to the brain than in adults due to thinner scalp and skull layers. Extension of FD-NIRS measurements for adults will be a challenging problem for future studies.

The methods in chapters 5 and 6 resulted in signicant improvements in the sensitivity of NIRS to detect brain activity and control false positives in the analysis of functional NIRS studies. The method is based on the simple principle of pre-whitening the time-series based on an autoregressive model of the errors. This conveniently turned motion artifacts into sharp outliers in an otherwise uncorrelated, normally distributed residual, which were easy to account for with robust regression methods. The methods are based on sound principles and relativley hands-off for the user, which avoids subjective input by the researcher in adjusting tuning parameters. In chapter 5, we saw that in the cases where motion caused a shift in the mean of the signal caused systematic underestimation t-statistics. Furthermore, slow non-oscillatory drifts in the signal also break the stationarity assumptions of autoregressive models. Future work should investigate the best way to fix these issues.

Although the methods developed in chapters 5 and 6 correct for serial correlations due to systemic physiology, there is an implicit assumption that the physiology is independent of the task. For example, a task that incorporated walking, stopping, walking, stopping, etc. can induce physiological changes that are correlated with the task. On one hand, measurement of systemic effects and the development of filtering/regression methods to remove these effects are an open area of current research in the field. On the other hand, even with a measurement of systemic physiology, when the task is correlated to physiology, this represents an issue with collinearity (i.e., the inversion is ill-conditioned) that might be better dealt with by better experimental design. This is another interesting area for future methods development research.

The work presented in chapter 6 on the development of adaptive methods based on the linear Kalman filter only investigated the case when the states are stationary. While this is certainly useful for many applications, the methods were developed in a general Kalman filter framework that allows for non-stationary states. This many be useful for developing analysis methods for offline analyis that investigate time-varying hemodynamics. For example, the investigation of single-trial variability or evoked hemodynamics that are modulated by learning effects may be two simple applications for future studies.

APPENDIX

INTERSLICE MAGNETIZATION TRANSFER EFFECTS FOR MTR IMAGING OF THE HUMAN BRAIN

This work was completed during my graduate studies before joining the lab of Dr. Huppert. Thus, it is unrelated to the main topic of the disseratation, but is included here as part of my graduate work.

A.1 ABSTRACT

We present a new method for magnetization transfer (MT) ratio imaging in the brain that requires no separate saturation pulse. Interslice MT effects that are inherent to multi-slice balanced steady-state free precession (bSSFP) imaging were controlled via an interslice delay time to generate MT-weighted (0 s delay) and reference images (5-8 s delay) for MT ratio (MTR) imaging of the brain. The effects of varying flip angle and phase encoding (PE) order were investigated experimentally in normal, healthy subjects. Values of up to ∼50% and ∼40% were observed for white and gray matter MTR. Centric PE showed larger MTR, higher SNR, and better contrast between white and gray matter than linear PE. Simulations of a two-pool model of MT agreed well with *in vivo* MTR values. Simulations were also used to investigate the effects of varying acquisition parameters, and the effects of varying flip angle, PE steps, and interslice delay are discussed. Lastly, we demonstrated reduced banding with a non-balanced SSFP-FID sequence and showed preliminary results of interslice MTR imaging of meningioma.

A.2 INTRODUCTION

Protons that are bound to macromolecules can exchange magnetization with free water protons leading to magnetization transfer (MT) phenomena [78]. Macromolecular protons cannot be observed directly with magnetic resonance imaging (MRI) because of fast transverse relaxation (T_2 $\sim$ 10 μs); however, macromolecular protons can be preferentially saturated by off-resonance (with respect to free water) radio frequency (RF) irradiation, since the absorption spectrum of macromolecular protons is much broader than that of free water. Exchange between the two pools of protons can transfer an observable decrease in magnetization to the free water pool. The percent signal decrease due to MT is called the magnetization transfer ratio (MTR). Changes in MTR can often give information about the macromolecules involved in generating the MT effects. One of the major applications of MTR imaging has been the evaluation of white matter (WM) integrity in multiple sclerosis [79], in which myelin content has been found to be significantly correlated with MTR [80]. Other applications include imaging articular cartilage of the knee [81, 82, 83], intervertebral disc degeneration [84], and characterization of brain tumors [85, 86].

Interslice MT effects that are inherent to sequential multi-slice acquisitions [87, 88, 89, 90] have been used to generate contrast for MT asymmetry imaging without a separate saturation pulse in the alternate ascending/descending directional navigation (ALADDIN) pulse sequence [91]. The same approach may be used for MTR imaging with an additional acquisition of reference images without MT weighting. The purpose of this work was to demonstrate the feasibility of MTR imaging in the brain using interslice MT effects to generate MT contrast and to investigate the characteristics of interslice MTR image acquisition with multi-slice balanced steady state free precession (bSSFP) imaging.

In this study, we validated the source of image contrast using a 10% agarose phantom (high MT effects) and saline phantom (no MT effects) and by comparing *in vivo* MTR images of the brain acquired with the proposed interslice method to MTR images acquired with conventional presaturation pulses. We compared *in vivo* MTR values for gray matter (GM) and WM at varying flip angle and phase encoding (PE) order with predictions from numerical simulations of the two-pool model using tissue parameters from the literature. Simulations were also used to investigate the effects of varying the number of PE steps, flip angle, and interslice delay as well as the accumulation of MT effects over multiple slices. Lastly, we demonstrate reduced banding with non-balanced SSFP and applied the proposed interslice MTR imaging method to a meningioma patient. Overall, the

technique offers an efficient method for MTR acquisition without the need for a separate saturation pulse.

A.3 METHODS

A.3.1 Theory

In 2D sequences, slice-selection is achieved by applying a linear gradient perpendicular to the slice plane causing the Larmor precession frequency to vary as a function of position. Excitation of a slice of interest is achieved by adjusting RF-pulse frequency to the Larmor frequency of the desired plane. The slice of interest receives on-resonance excitation; however, the rest of the volume receives off-resonance irradiation. During acquisition of one slice, excitation pulses are effectively a series of off-resonance saturation pulses to future slices (Fig. A1). The off-resonance frequency received by neighboring slices is given by

$$\delta_n = -BW \cdot \left(1 + \frac{GAP}{THK}\right) \cdot n \cdot sign(GRAD) \cdot ORD \ , \tag{.1}$$

where BW is the bandwidth of the RF-pulse, GAP is the interslice gap; THK is the slice thickness; n is the slice index with positive indices indicating slices superior to the acquisition slice, and negative indices indicating slices inferior to the acquisition slice; $sign(GRAD)$ is the sign of the gradient; ORD is +1 if ascending slice order and -1 if descending slice order. The off-resonance irradiation received by neighboring slices can saturate macromolecular protons leading to interslice MT effects. This idea is illustrated in Fig. A1.

Interslice MT effects can be enhanced as a mechanism for generating contrast by the use of bSSFP acquisition, in which high flip angle and short repetition time (TR) lead to high saturation of the macromolecular pool. The interslice gap is set to a high value (e.g. 140% the slice thickness) to avoid crosstalk caused by overlapping slice profiles and so that interleaving two acquisitions gives a full set of images at typical gap size (e.g. 20% the slice thickness) [91]. For imaging in the brain, descending slice order is preferred to ascending slice order, in order to suppress signal contributions from blood perfusion. Because MT effects can accumulate over multiple slices, a few extra "dummy" slices must be collected in the MT-weighted image sets to ensure homogeneous MT contrast across slices. These slices can be positioned outside the imaging volume of interest (e.g., above the head) and discarded during reconstruction. Reference images without MT-weighting

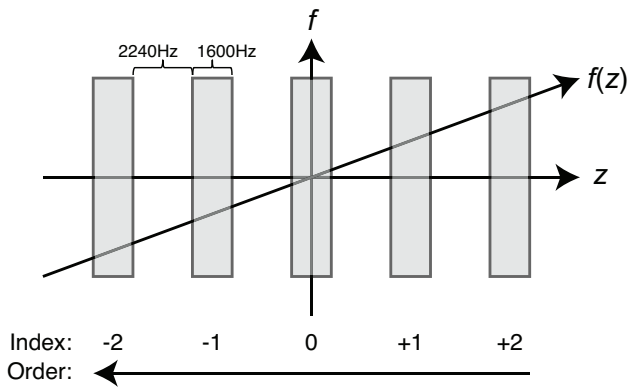

Figure A1: Illustration of interslice MT effects. The application of a gradient varies the Larmor frequency $f(z)$ linearly in space (z). During excitation, the slice of interest (slice 0) receives on resonance excitation. With a positive gradient polarity and descending slice order (shown above), the next slice to be acquired (slice -1) receives off-resonance irradiation at a frequency offsets of 3840 Hz.

can be acquired by adding an interslice delay sufficient for T_1 recovery. The MTR value, which measures the percent signal decrease, can be calculated pixel by pixel as follows:

$$MTR = (I_{Ref} - I_{MT})/I_{Ref} \times 100\% \ , \tag{.2}$$

where I_{MT} and I_{Ref} are the signal intensities of corresponding pixels in the MT-weighted and reference images, respectively.

The modified two-pool model [92] can be used to quantitatively model MT effects generated by sequential 2D bSSFP acquisitions. In this model, a free liquid pool (subscript f) exchanges longitudinal magnetization with a restricted macromolecular pool (subscript r). Using an RF-pulse given by

$$\boldsymbol{B_1}(t) = b_1(t)\cos\left((\omega_{RF} - \omega_{0,f})\ t\right)\hat{\boldsymbol{x}} + b_1(t)\sin\left((\omega_{RF} - \omega_{0,f})\ t\right)\hat{\boldsymbol{y}} \ , \tag{.3}$$

where ω_{RF} is the angular frequency of the RF pulse, $\omega_{0,f}$ is the angular frequency at free water resonace, and $b_1(t)$ is the magnitude of the RF pulse, the two pool model can be described

mathematically in a frame rotating at $\omega_{0,f}$ using the Bloch equations with additional terms for exchange of longitudinal magnetization between the proton pools:

$$\frac{dM_{x,f}}{dt} = \gamma b_1(t)\ M_{z,f}\ \sin\left((\omega_{RF} - \omega_{0,f})\ t\right) - \frac{M_{x,f}}{T_{2,f}} \tag{.4}$$

$$\frac{dM_{y,f}}{dt} = \gamma b_1(t)\ M_{z,f}\ \cos\left((\omega_{RF} - \omega_{0,f})\ t\right) - \frac{M_{y,f}}{T_{2,f}} \tag{.5}$$

$$\begin{aligned}\frac{dM_{z,f}}{dt} = &-\gamma b_1(t)\ M_{x,f}\ \sin\left((\omega_{RF} - \omega_{0,f})\ t\right) \\ &-\gamma b_1(t)\ M_{y,f}\ \cos\left((\omega_{RF} - \omega_{0,f})\ t\right) \\ &-\frac{M_{z,f} - M_{0,f}}{T_{1,f}} - M_{z,f}\ F\ k_r + M_{z,r}\ k_r\end{aligned} \tag{.6}$$

$$\frac{dM_{z,r}}{dt} = -\frac{M_{z,r} - M_{0,r}}{T_{1,r}} + M_{z,f}\ F\ k_r - M_{z,r}\ k_r - M_{z,r}\ W(t)\ , \tag{.7}$$

with z denoting the longitudinal component, and x and y denoting transverse components of magnetization. The longitudinal and transverse magnetization decay constants are given by T_1 and T_2, respectively. The ratio of the fully-relaxed longitudinal magnetizations gives the ratio of pool sizes ($F = M_{0,r}/M_{0,f}$), and k_r is the pseudo-first-order exchange rate constant. The saturation rate of the restricted pool is proportional to the square of the RF-pulse amplitude and to the absorption lineshape, $G(\omega)$:

$$W(t) = \pi\ \gamma^2\ b_1^2(t)\ G(\omega_{RF})\ . \tag{.8}$$

A super-Lorentzian lineshape has been found to model tissues well [93] and is defined by the following integral:

$$G(\omega) = T_{2,r}\sqrt{\frac{2}{\pi}}\int_0^1 \frac{1}{|3u^2 - 1|}\ \exp\left(-2\left(\frac{(\omega - \omega_{0,r})\ T_{2,r}}{3u^2 - 1}\right)^2\right) du\ , \tag{.9}$$

where the term $\omega_{0,r}$ is the peak of the absorption spectrum of the macromolecular pool, which can account for MT asymmetry when $\omega_{0,r} \neq \omega_{0,f}$ [94]. For this study, MT asymmetry was not considered ($\omega_{0,r} = \omega_{0,f}$). On-resonance MT effects [95] were simulated for WM and GM by setting $G(0) = 1.4 \times 10^{-5}\ \mathrm{s}^{-1}$ according to Gloor, Scheffler, and Bieri [96].

A.3.2 Ethical considerations

All imaging experiments were approved by the Institutional Review Boards at the University of Pittsburgh and Seoul National University and written informed consent was obtained from all participants.

A.3.3 Instrumentation and Software

The experiments were performed on Siemens 3T Trio systems (Siemens Medical Solutions, Erlangen, Germany), and a 12-element head matrix coil was used for reception with body coil transmission for all data acquisitions. All simulations and analyses were performed with Matlab (Mathworks, Natick, MA).

A.3.4 Image Reconstruction

Baseline images were reconstructed by the MR scanners. Dummy slices in the MT-weighted images were discarded prior to MTR calculation. The number of MTR slices was equal to the the number of reference image slices for all acquisitions described below. Calculation of MTR images consisted of creating either a whole head or brain mask and calculating MTR pixel by pixel inside the masked region according to Eq. .2. Brain masks were created from segmentations generated using SPM8 software (Wellcome Trust Centre for Neuroimaging, London, UK), whereas whole head masks were generated simply by thresholding based on intensity.

A.3.5 Simulations

Computer simulations were performed using the parameters summarized in Table A1 for GM and WM. We considered six prior slices of off-resonance saturation for MT-weighting (e.g., 23040 Hz, 19200 Hz, 15360 Hz, 11520 Hz, 7680 Hz, 3840 Hz). For reference image signal, the acquisition slice was simulated with no prior slices of off-resonance saturation (i.e., full T_1 recovery from prior slices), except when specifically investigating the effects of varying interslice delay. We modeled excitation with a Gaussian windowed sinc pulse. Other simulation parameters were taken to match acquisition parameters, such as flip angle, number of PE steps, TR, and RF duration. The set of differential equations .4-.7 were solved using the 4th/5th order Runge-Kutta algorithm. For analysis, we calculated MTR values using the magnitude of the transverse magnetization at the center line of k-space for MT-weighted and reference signal simulations. In addition to comparing simulations with *in vivo* data, we used simulations to investigate the dependence of MT contrast on the number of preceding slices for varying flip angles and number of PE steps. Lastly, we

investigated the effects of varying the interslice delay from 0-8 s by simulating reference image acquisition with 6 prior slices of off-resonance irradiation with a specified delay time between each slice.

Table A1: Two-Pool MT Parameters at 3T

	$T_{1,f}$	$T_{2,f}$	$T_{1,f}$	$T_{2,f}$	k_r	F
White Matter	1.1 s	85 ms*	1 s	13 μs	23 s^{-1}	0.14
Gray Matter	1.8 s	99 ms	1 s	9 μs	40 s^{-1}	0.05

*Measured in this study. All other values from Stanisz et. al. [97].

A.3.6 Phantom Imaging

A cylindrical 10% agarose phantom with a diameter of 140 mm and height of 180 mm was imaged for initial assessment of interslice MTR imaging. Additionally, a cylindrical saline phantom with a diameter of 120 mm and height of 195 mm was imaged with the same acquisition parameters as a negative control. The MTR images were reconstructed from baseline bSSFP images according to Eq. .2. Centric PE order was used for acquisition. Other acquisition parameters were as follows: slice order = descending; slice-select gradient polarity = positive; readout gradient polarity = positive; TR/TE = 4.56/2.28 ms; matrix size = 256 × 256; field of view = 256 × 256 mm^2; flip angle = 50°; slice thickness = 4 mm; interslice gap = 5.6 mm (0.8 mm after interleaving); scan direction = axial; PE direction = anterior-posterior; dummy PE steps = 30; phase oversampling = 50%; number of averages = 1; RF-pulse BW = 1600 Hz; acquisition BW = 501 Hz/pixel; number of slices = 19 and 18 for each interleaved MT-weighted image set (including dummy slices) and 25 for reference images; interslice delay = 0 s for MT-weighted images and 6 s for reference images.

A.3.7 Comparison of Interslice and Presaturation MT Effects

For three normal, healthy subjects (age 21-40), MTR images were acquired using the proposed interslice method and using conventional presaturation pulses with an identical bSSFP readout (single slice; no interslice MT effects), in order to confirm the source of image contrast *in vivo*. Three different off-resonance irradiation frequencies were used for the presaturation pulses corresponding to the offset frequencies of the first (3200 Hz), second (6400 Hz), and third prior (9600 Hz)

slices of the interslice method. The average RF-power off-resonance irradition of the two methods were equivalent (94 μT). The following parameters of the bSSFP readout were the same for both acquistion methods: TR/TE = 4.15/2.08 ms; matrix size = 128 × 128; field of view = 220 × 220 mm^2; flip angle = 60°; slice thickness = 5 mm; phase partial Fourier = 6/8; scan direction = axial; PE direction = right-left; initial dummy PE steps = 30; centric PE order; phase oversampling = 0%; RF-pulse BW = 1333 Hz; and acquisition BW = 592 Hz/pixel.

The interslice MTR images were acquired with descending slice order and positive slice-select gradient. The rest of the imaging parameters for the proposed interslice method were as follows: gap = 7 mm; number of average = 1; number of slices = 19 (including dummy slices) for MT-weighted images and 13 for reference images; interslice delay = 0 s for MT-weighted images and 5 s for reference images; nominal scan time of 10 s for MT-weighted images and scan time of ∼1.1 min for reference images. The off-resonance irradiation condition of the interslice method was: pulse width = 1.2 ms; inter-pulse interval = 4.15 ms (∼29% duty cycle); and average RF power = 0.94 μT.

For the images acquired with presaturation, both MT-weighted and reference images were acquired with number of slices = 1, number of averages = 1, and a sufficient acquisition delay time of 5 s to get rid of any residual signals prior to each measurement. A pulse train of 75 Gaussian pulses were used for off-resonance irradiation with the following saturation condition: flip angle = 578.4°; pulse width = 20 ms; inter-pulse interval = 40 ms (50% duty cycle); total saturation duration = 3 s; average RF power = 0.94 μT (equivalent to interslice method above); off-resonance irradiation frequencies = +3200 Hz, +6400 Hz, and +9600 Hz.

Regions of interest (ROI) for the data were created manually for WM. Mean MTR values were computed for the WM ROI for each subject, and the results were averaged across subjects. Signal to noise ratio (SNR) was estimated from the difference image ($I_{Ref} - I_{MT}$) as the mean of the signal in the WM ROI divided by the standard deviation of a large region in the difference image containing only noise.

A.3.8 Effects of Varying Flip Angle and Phase Encoding Order

For six normal, healthy subjects (age 24-39), MTR images were reconstructed from baseline bSSFP images acquired at varying flip angles from 15° to 90° in 15° intervals with descending slice order and positive slice-select gradient. Additional scan parameters were as follows: TR/TE = 4.11/2.06

ms; matrix size = 128 × 128; field of view = 230 × 230 mm^2; slice thickness = 5 mm; interslice gap = 7 mm; scan direction = axial; PE direction = anterior-posterior; initial dummy PE steps = 10/30 for linear/centric PE order; phase oversampling = 50%; number of averages = 1; RF-pulse BW = 1067 Hz; acquisition BW = 673 Hz/pixel; number of slices = 15 for MT-weighted images (including dummy slices) and 7 for reference images; interslice delay = 0 s for MT-weighted images and 8 s for reference images. Scan time for MT-weighted images was 13 s and scan time for reference images was ∼1 min. Lastly, we measured the observed T_2 value of the center slice using a multi-contrast spin echo sequence with echo times varying from 30 ms to 300 ms in 30 ms intervals.

Regions of interests for the data were created by automatic segmentation of GM and WM via SPM8 software. Segmentation results were checked manually to ensure quality. Mean MTR values were computed for the WM and GM ROIs as a function of flip angle for each subject, and the results were averaged across subjects. Signal to noise ratio was estimated from the difference image ($I_{Ref} - I_{MT}$) as the mean of the signal in the combined WM and GM ROI divided by the standard deviation of a large region in the difference image containing only noise.

A.3.9 Comparison of bSSFP and SSFP-FID

For five normal, healthy subjects (ages 24-49), MTR images were acquired for near full brain coverage using a bSSFP sequence. Two of the subjects were also imaged with a SSFP-FID sequence. Common acquisition parameters for both sequences were as follows: slice order = descending; slice-select gradient polarity = positive; readout gradient polarity = positive; matrix size = 256 × 256; field of view = 256 × 256 mm^2; flip angle = 50°; slice thickness = 3 mm; interslice gap = 4.2 mm (0.6 mm after interleaving); scan direction = axial; PE direction = anterior-posterior; dummy PE steps = 30; phase oversampling = 50%; number of averages = 1; RF-pulse BW = 1600 Hz; acquisition BW = 501 Hz/pixel; number of slices = 19 and 18 for each interleaved MT-weighted image set (including dummy slices) and 25 for reference images; interslice delay = 0 s for MT-weighted images and 6 s for reference images. For the bSSFP sequence, TR/TE = 4.56/2.28 ms and total scan time = 4.36 min (1.17 min for MT-weighted images and 3.18 min for reference images). For the SSFP-FID sequence, TR/TE = 4.31/2.21 ms and total scan time = 4.24 min (1.10 min for MT-weighted images and 3.14 min for reference images).

For each subject ROIs were created manually for WM. Mean MTR and SNR for the WM ROI were estimated for each subject, and the results were averaged across subjects. The MTR and SNR values were compared for the bSSFP and SSFP-FID sequences.

A.3.10 Interslice MTR Imaging of Meningioma

For a meningioma patient, MTR images were acquired with full brain coverage using acquisition parameters: PE order = centric; slice order = descending; slice-select gradient polarity = positive; readout gradient polarity = positive; TR/TE = 4.15/2.08 ms; matrix size = 128 × 128; field of view = 220 × 220 mm^2; flip angle = 60°; slice thickness = 5 mm; interslice gap = 7 mm; scan direction = axial; PE direction = right-left; initial dummy PE steps = 30; phase oversampling = 0%; phase partial Fourier = 6/8; number of averages = 1; RF-pulse BW = 1333 Hz; acquisition BW = 592 Hz/pixel; number of slices = 18 and 19 for each interleaved MT-weighted image set (including dummy slices) and 19 for reference images; interslice delay = 0 s for MT-weighted images and 5 s for reference images. The total scan time was 2.1 min (0.4 min for MT-weighted images and 1.7 min for reference images).

For comparison with the proposed method, T_2-weighted images were acquired using a Turbo Spin Echo (TSE) sequence with imaging parameters: number of slices = 25; TR = 6000 ms; TE = 93 ms; echo train length = 18; matrix size = 640 × 520; field of view = 220 × 178 mm^2; number of acquisitions = 1; slice thickness = 5 mm; flip angle = 120°; and scan time = ∼1.2 min.

A.4 RESULTS

A.4.1 Phantom Imaging

Figure A2 shows the resulting MTR images of the 10% agarose phantom and saline phantom. The MTR images of the agarose phantom (left) showed relatively homogeneous MTR values with the exception of dark spots caused by air bubbles trapped in the phantom. The saline phantom (right), which was expected to have no MT effects, was free from extraneous signals (note the scale difference between the two images). Together, the agar and control phantom images strongly support MT effects as the source of image contrast.

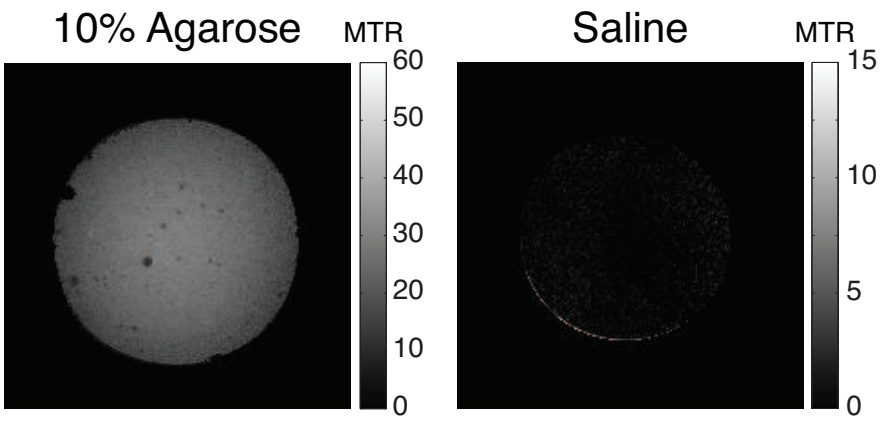

Figure A2: MTR images of a 10% agarose phantom (left) and saline phantom (right).

A.4.2 Comparison of Interslice and Presaturation MT Effects

Figure A3 shows the representative MTR images using the interslice method and using conventional presaturation with a bSSFP readout for different offset irradiation frequencies corresponding to the offset frequencies of the first, second, and third prior slices of the interslice method. Visually, the signals in WM were higher than GM for all MTR images (Fig. A3a). The MTR images acquired with presaturation showed decreasing MTR and SNR for increasing offset irradiation frequencies. The average SNR and MTR values from the proposed interslice method were similar to those with presaturation at an offset irradiation frequency corresponding to the first prior slice of the interslice method (Fig. A3b-c), indicating that contribution of the first prior slice is dominant in the interslice MTR method and that the saturation efficiency of the interslice method is comparable to conventional method.

A.4.3 Effects of Varying Flip Angle and Phase Encoding Order

Figure A4 shows the center slice images for varying flip angle and for linear and centric PE from a representative subject. Centric PE images showed better GM and WM contrast, suggesting that relaxation effects influenced image contrast with linear PE.

Figures A5a and A5b show the results of ROI analysis along with two-pool model simulations of the acquisition protocol. Overall, MTR and SNR values increased with flip angle within the

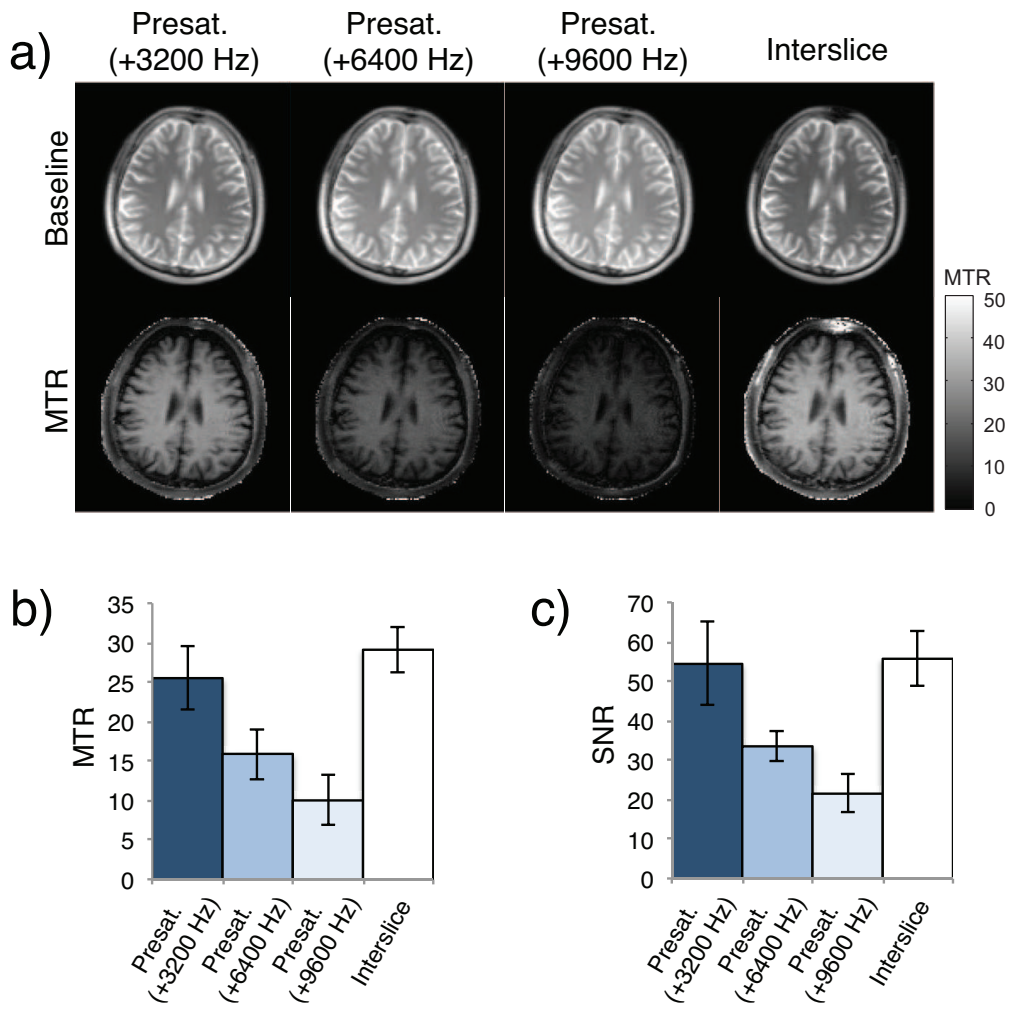

Figure A3: Comparison of MTR images generated with interslice MT effects and with presaturation. Offset irradiation frequencies of the presaturation pulses corresponded to the offeset frequencies of the first (+3200 Hz), second (+6400 Hz), and third (+9600 Hz) prior slices of the interslice method. Average RF-power of saturation was equivalent in both methods. Baseline and MTR images (a) from a representative subject are shown. Both MTR (b) and SNR (c) were calculated for white matter. Error bars show the 95% confidence interval of the group average.

tested range. Centric PE images showed higher MTR values and substantially higher SNR than linear PE images (Figure A5c). Simulated MTR values using tissue parameters from the literature agreed well with the *in vivo* values. Substitution of the observed T_2 value of 85 ms (from fitting the T_2 map to a single-exponential function) for the literature value (69 ms [18]) produced simulated MTR values in closer agreement with *in vivo* results.

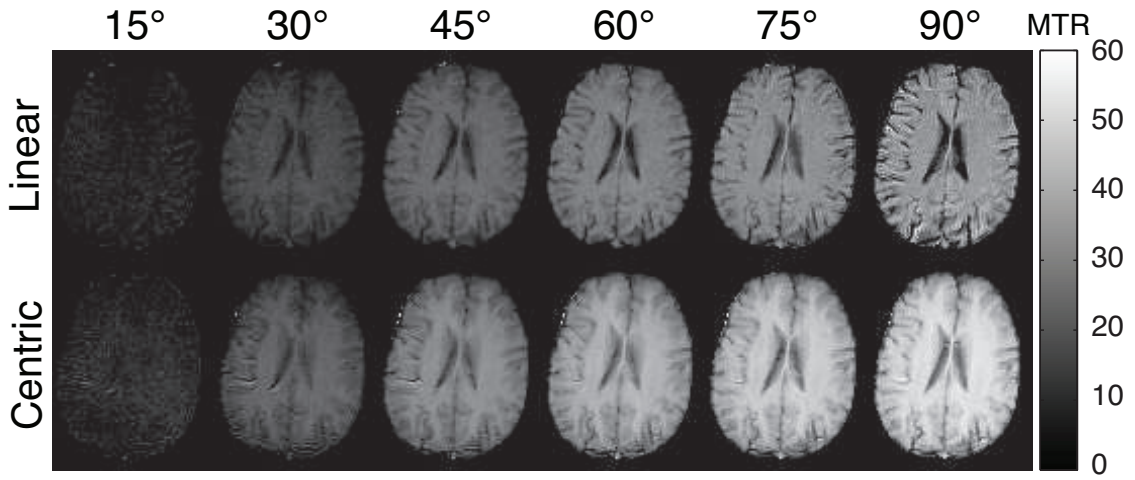

Figure A4: Center slices of MTR images from a representative subject are shown for varying flip angles and for linear phase encoding (top) and centric phase encoding (bottom).

A.4.4 Accumulation of MT Effects from Prior Slices

Figure A6 shows simulations of the longitudinal magnetization ($M_{z,f}$) for WM and GM for varying number of PE steps (RF-pulses) per slice, and two different flip angles. In agreement with the results in Fig. A3, the majority of saturation was generated by the first prior slice; however, a few dummy slices are needed to account for the contributions of earlier (2nd, 3rd, etc.) prior slices to reach a steady value of longitudinal magnetization across slices. More dummy slices are needed for lower flip angles and for lower number of PE steps per slice. The value of magnetization reached depended on the number of PE steps per slice and appeared to asymptotically approach true steady-state MT effects (i.e., the state that would be achieved after an infinite chain of saturation pulses at off-resonance frequency δ_{-1}). For 128 PE steps, 5-6 dummy slices should be included to reach steady MT effects. For 256 or more PE steps, 3-4 dummy slices appeared to be sufficient.

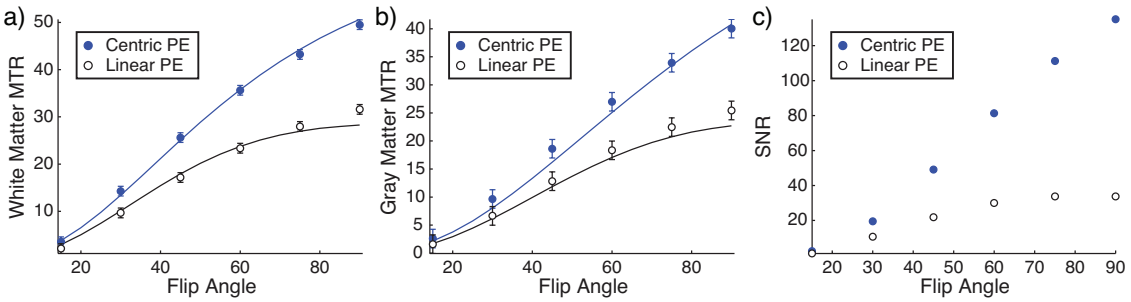

Figure A5: Mean MTR values across subjects from regions of interest for white (a) and gray matter (b). Predicted values from simulating the two-pool model (solid lines) with parameters from the literature show close agreement with the *in vivo* values. Centric phase encoding shows substantially better SNR (c) than linear phase encoding. Error bars show the 95% confidence interval of the group average.

Including more dummy slices than needed would have minimal impact on scan time (∼1-3 s per dummy slice).

A.4.5 Effects of Varying Interslice Delay

Figure A7 shows simulations with varying interslice delay time for acquisition of reference images. In general, the MTR asymptotically increased with interslice delay time at rate that is dependent on the T_1 value of the tissue, with longer T_1 values requiring a longer interslice delay to recover. An interslice delay time of 3-4 s (rather than 8 s) for acquisition of reference images would still maintain most of the MT contrast, indicating that the scan time for the acquisition of reference images could be reduced accordingly (3-5 s per slice).

A.4.6 Comparison of bSSFP and SSFP-FID

Figure A8 shows representative images using the interslice MTR imaging method with bSSFP and SSFP-FID sequences. The SSFP-FID sequence is a non-balanced SSFP sequence that is less sensitive to banding artifacts in regions of high susceptibility. Regions near the sinuses in slices 3-5 were corrupted by banding artifacts with the bSSFP, but no artifacts were present in the same

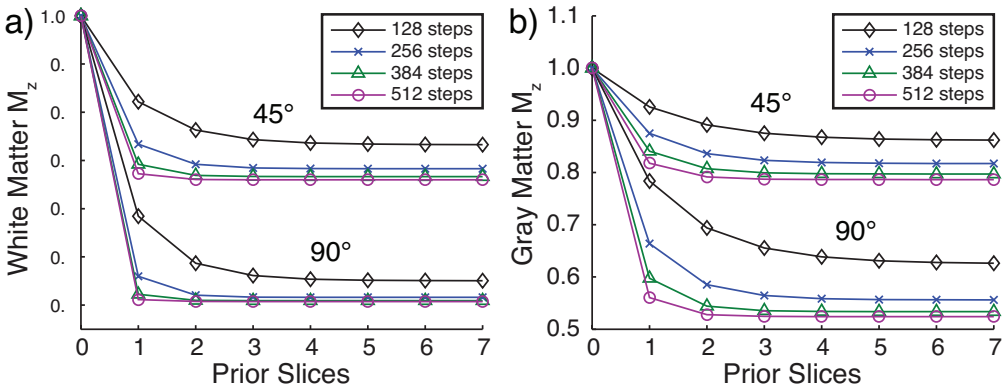

Figure A6: **Saturation of the longitudinal magnetization accumulates over multiple prior slices with the majority of saturation due to the first prior slice.** For white (a) and gray (b) matter, simulations show the longitudinal magnetization as a function of the number of prior slices for varying number of phase encoding steps per slice and for varying flip angles.

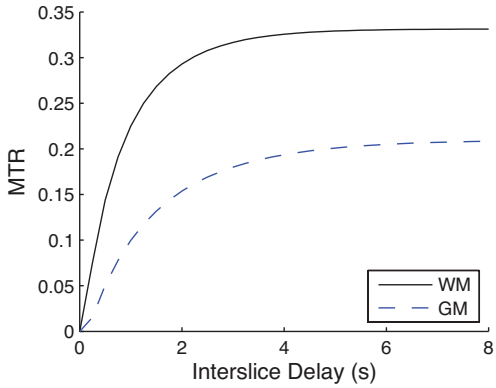

Figure A7: Simulated MTR values for white (solid line) and gray matter (dashed line) for varying interslice delay time for reference image acquisition. Simulations were performed using sequence parameters that matched the bSSFP acquision for images in Fig. A8.

slices acquired with the SSFP-FID sequence. The mean MTR values of WM were 32% and 33% for bSSFP and SSFP-FID, respectively. The SNR in WM was 19.5 and 15.2 for bSSFP and SSFP-FID respectively. Overall, the SSFP-FID sequence eliminated banding artifacts, but reduced SNR by 22%.

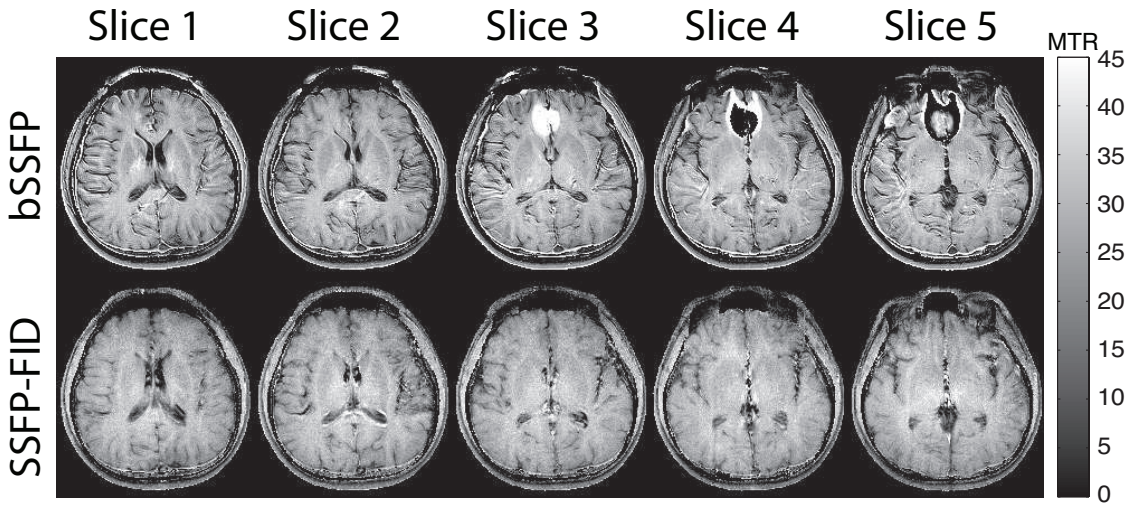

Figure A8: Comparison of interslice MTR imaging with bSSFP and SSFP-FID sequences. The SSFP-FID sequence significantly reduced banding artifacts in slices 3-5, but SNR was 22% lower than with bSSFP.

A.4.7 Interslice MTR Imaging of Meningioma

Figure A9 shows the MTR images acquired over the brain tumor region. The T_2 images showed higher signal in the tumor region compared to normal tissue. The MTR images from the interslice method showed distinct signal characteristics in the brain tumor regions, different from the T_2 images.

A.5 DISCUSSION

In this study, we demonstrated the feasibility of using interslice MT effects to generate contrast for MTR imaging. Furthermore, we validated the source of contrast as MT with phantoms and by

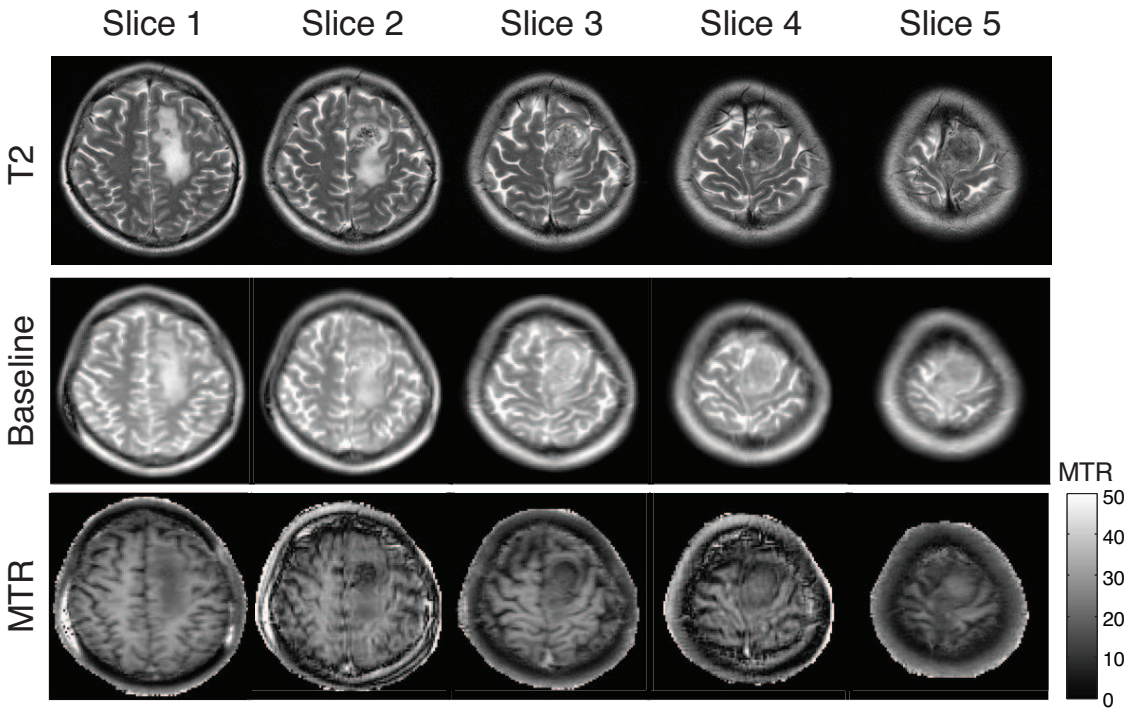

Figure A9: Interslice MTR images of a brain tumor (meningioma). Distinct signal characteristics in the MTR images were visible in the brain tumor regions.

comparing interslice MT effects with contrast generated from conventional presaturation pulses. We investigated effects of varying flip angle, number of PE steps, number of prior slices, and interslice delay. We showed that banding artifacts could be reduced by using a non-balanced SSFP sequence with no modifications to the acquisition strategy. Finally, we demonstrated the proposed method in a meningioma subject, in which the interslice MTR images showed distinct contrast.

A.5.1 Interslice MTR Signal Characteristics

In the interslice method, data are acquired during the transient period of bSSFP acquisition. The magnetization state at the start of acquisition of the imaging slice (partially saturated for MT-weighted, relaxed for reference images) will move towards the steady state of the bSSFP readout, determined by the dynamics of bSSFP with contributions from on-resonance MT effects. This explains why lower MTR values were seen with linear PE. With a sufficiently large number of TRs before the acquisition of the center of k-space, no contrast is expected between the MT-weighted and reference image acquisitions. Centric PE mitigates this issue by capturing the MT contrast at the beginning of the acquisition in the low spatial frequencies. Despite this limitation, we have validated the image contrast as MT effects in phantoms (Fig. A2), shown that the contrast was predictable based on quantitative models of MT (Fig. A5), and generates distinct contrast in preliminary imaging of a meningioma subject (Fig. A9).

The results in Fig. A3 showed that the contributions from the second and third prior slices were minor compared to the first prior slice. The contributions are futher reduced in the interslice method due to nominal delay times of ∼0.65 s and ∼1.3 s for the second and third prior slices, respectively, in contrast to the first prior slice which has a nominal delay time of 0 s.

A.5.2 Potential Applications

The results from imaging of the meningioma patient showed that MTR images can be acquired in a relatively short period (e.g. ∼2.1 min) over the whole brain region using the proposed interslice method. Assessment of brain tumor tissue is difficult, and the distinct MTR contrast as shown in Fig. A9 may reflect unique metabolic information of the tumor region.

The interslice MTR method may offer some advantage in terms of SAR compared to other methods, such as gradient echo methods, which rely on a separate pulse for saturation, or on-resonance MTR imaging [98, 99], which relies on a short RF-pulse duration to generate MT effects.

The SAR levels for the images acquired in Fig. A8 ranged from 37-56% of the scanner limit during acquisition of MT-weighted images with a 1 ms RF-pulse; however, we have shown that high MTR values can be achieved with a longer 1.5 ms RF-pulse (Fig. A5). Since SAR levels have a quadratic dependence on RF-pulse amplitude, the interslice MTR method may be optimized for low SAR applications or high field applications by increasing the RF-pulse duration.

In the ALADDIN sequence, sequential multi-slice bSSFP acquisitions with alternating slice order and slice-select gradient polarity, as well as alternating readout gradient polarity [100] are used for interslice MT asymmetry [91] and perfusion imaging [101]. The ALADDIN sequence can be modified by adding acquisition of a set of reference images to calculate MTR images. This would allow for simultaneous acquisition of four different image contrasts: baseline, perfusion, MT asymmetry, and MTR images.

The MTR is considered a semi-quantitative measurement, since the value is dependent on scan parameters. In quantitative MT imaging, the two-pool model is fit to multiple MT-weighted acquisitions, in which parameters such as bound pool fraction (F) and magnetization exchange rate (k_r) may offer better insight into tissue characteristics. Agreement of the data and two-pool model simulations in this study suggest the possibility for developing quantitative MT methods using interslice MT effects. Saturation power and off-resonance frequency can be controlled simultaneously by changing excitation pulse duration, which is inversely proportional to off-resonance frequency δ and inversely proportional to the square of saturation power (W). The technique shows potential as a novel method for fast quantitative MT, since a full set of MT-weighted images can be collected in less than 1 min.

A.5.3 Comparison with On-resonsance MTR Imaging with SSFP

Another SSFP based method for MTR has previously been developed using the difference in on-resonance MT effects of long and short RF-pulse duration acquisitions [98, 99]. Thus, it is worth briefly comparing the proposed method to the on-resonance MTR method. The off-resonance signal responses of bSSFP are periodic as a function of the off-resonance frequencies and the TR of the bSSFP sequence. The on-resonance MTR method is based on the assumption that both MT-weighted (short RF-pulse) and reference (long RF-pulse) images are acquired on the pass-band region of the bSSFP off-resonance responses. This assumption seems reasonable for normal brain regions; however, the assumption may not hold under pathological conditions, such as brain

tumors or hemorrhages that can cause high susceptibility effects. Because of using different TR values between MT-weighted and MT free imaging, the on-resonance MTR method also shows significantly reduced MTR in relatively short T2 components, as demonstrated 40% reduction of MTR in 4% agar phantom with T_1 = 1960 ms and T_2 = 43 ms [99]. In contrast, the interslice MTR method uses the same scan parameters for acquisition of MT-weighted and references with only the addition of an interslice delay time, which does not affect off-resonance responses of bSSFP and also provides high MTR values in relatively short T_2 components as demonstrated in the 10% agar phantom with T_1 = 1.7 s and T_2 = 36 ms (Fig. A2). The interslice method may potentially offer more reliable MTR measurements in brain lesions.

In terms of sensitivity, the 3D on-resonance MTR method can provide higher SNR because of volumetric averaging effects. The proposed interslice method may be implemented in 3D as multiple overlapping thin slab acquisition, which can improve spatial resolution and SNR and requires further evaluation. Also, the availability of higher flip angle and longer data sampling time due to no restrictions on RF duration and TR in the interslice MTR method can further improves its MTR (as shown in Figs. A4 and A5) and SNR (lower acquisition BW), respectively. These factors of the interslice method can partly compensate for the volumetric averaging effects of the on-resonance MTR method.

In terms of scan time, both the interslice and on-resonance MTR methods require covering the region of interest using bSSFP acquisitions twice (MT-weighting and MT-free). If the TR of the interslice method (e.g. 4 ms) is the same as the average of the short and long TRs of the on-resonance method (e.g. 3 ms and 5 ms [102]), the time for actual data acquisition will be similar between the two methods, except for the interslice delay required by the interslice method. Data from a single subject (Fig. A10) showed preliminary evidence that good MTR maps can be acquired with near whole brain coverage with very short interslice delay times (0.7-2.0 s), which makes the total scan time of the interslice method (1-1.5 min) about 50% longer than the on-resonance method, depending on in-plane matrix size. Note that while a short interslice delay does not provide completely MT-free reference images, the long TR (5 ms) acquisiton for the on-resonance method also does not provide completely MT-free conditons. Scan time and SNR are related to each other and thus should be systematically evaluated together, but this is beyond the scope of the current study.

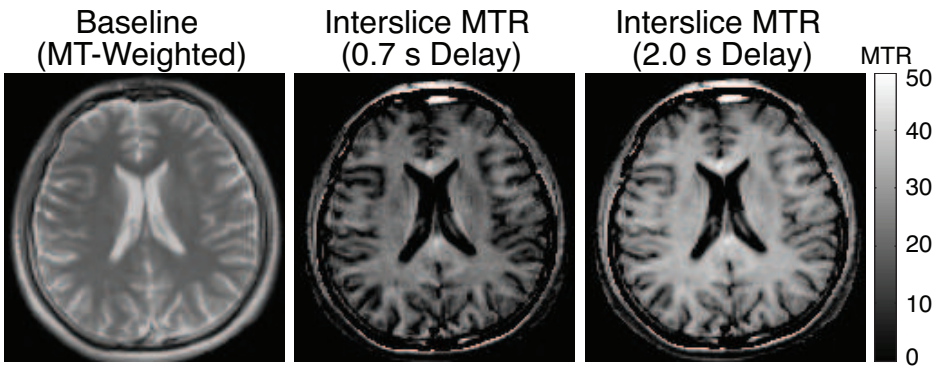

Figure A10: Interslice MTR images with short interslice delay times. Matrix size = 128 × 128, FA = 60°, TR/TE = 4.15/2.08 ms, RF-pulse duration = 1.24 ms, slice thickness = 5 mm, number of slices = 24 (excluding 6 dummy slices), total scan time = 56 s (0.7 s delay) and 87 (2.0 s delay). Two scans (each with 12 number of slices excluding 3 dummy slices) were spatially interleaved, in order to provide near whole brain coverage with no gap.

A.6 CONCLUSIONS

We demonstrated the feasibility of MTR imaging using interslice MT effects generated from sequential multi-slice bSSFP acquisition. The technique provides a method for MTR imaging without additional saturation pulses. Centric PE provided higher MTR values, higher SNR, and better image contrast. Linear PE images showed image contrast influenced by relaxation effects. Simulation of the two-pool model with parameters from the literature agreed well with *in vivo* data and provided a useful tool for investigating the characteristics of interslice MT effects. The new technique could provide MTR images covering the whole brain of a tumor patient within a clinically feasible scan time of ∼2 min (or less with sequence optimization). Potential unique applications include optimization for low SAR imaging and simultaneous MTR, MT asymmetry, and perfusion imaging. Further work is needed to systematically compare the proposed method with on-resonance MTR method and evaluate clinical usefulness of the proposed method.

BIBLIOGRAPHY

[1] Marie-Christine Taillefer and Andre Y Denault. Cerebral near-infrared spectroscopy in adult heart surgery: systematic review of its clinical efficacy. *Canadian Journal of Anesthesia*, 52(1):79–87, 2005.

[2] Marco Ranucci, Giuseppe IsgrO, Teresa De La Torre, Federica Romitti, Daniela Conti, and Concetta Carlucci. Near-infrared spectroscopy correlates with continuous superior vena cava oxygen saturation in pediatric cardiac surgery patients. *Pediatric Anesthesia*, 18(12):1163–1169, 2008.

[3] JS Wyatt, DT Delpy, M Cope, Susan Wray, and EOR Reynolds. Quantification of cerebral oxygenation and haemodynamics in sick newborn infants by near infrared spectrophotometry. *The Lancet*, 328(8515):1063–1066, 1986.

[4] Judith H Meek, Clare E Elwell, David C McCormick, A David Edwards, Janice P Townsend, Ann L Stewart, and John S Wyatt. Abnormal cerebral haemodynamics in perinatally asphyxiated neonates related to outcome. *Archives of Disease in Childhood-Fetal and Neonatal Edition*, 81(2):F110–F115, 1999.

[5] Lan Gao, Rame Taha, Dominique Gauvin, Lamia B Othmen, Yang Wang, and Gilbert Blaise. Postoperative cognitive dysfunction after cardiac surgery. *CHEST Journal*, 128(5):3664–3670, 2005.

[6] Ming-Chi Lai and San-Nan Yang. Perinatal hypoxic-ischemic encephalopathy. *BioMed Research International*, 2011, 2010.

[7] I Miyai, H C Tanabe, I Sase, H Eda, I Oda, I Konishi, Y Tsunazawa, T Suzuki, T Yanagida, and K Kubota. Cortical mapping of gait in humans: a near-infrared spectroscopic topography study. *Neuroimage*, 14(5):1186–1192, Nov 2001.

[8] M Suzuki, I Miyai, T Ono, and K Kubota. Activities in the frontal cortex and gait performance are modulated by preparation. an fnirs study. *Neuroimage*, 39(2):600–607, Jan 2008.

[9] H Karim, S I Fuhrman, P Sparto, J Furman, and T Huppert. Functional brain imaging of multi-sensory vestibular processing during computerized dynamic posturography using near-infrared spectroscopy. *Neuroimage*, 74:318–325, Jul 2013.

[10] H Karim, B Schmidt, D Dart, N Beluk, and T Huppert. Functional near-infrared spectroscopy (fnirs) of brain function during active balancing using a video game system. *Gait Posture*, 35(3):367–372, Mar 2012.

[11] H T Karim, S I Fuhrman, J M Furman, and T J Huppert. Neuroimaging to detect cortical projection of vestibular response to caloric stimulation in young and older adults using functional near-infrared spectroscopy (fnirs). *Neuroimage*, 76C:1–10, Mar 2013.

[12] X Cui, D M Bryant, and A L Reiss. Nirs-based hyperscanning reveals increased interpersonal coherence in superior frontal cortex during cooperation. *Neuroimage*, 59(3):2430–2437, Feb 2012.

[13] Mark Cope. The application of near infrared spectroscopy to non invasive monitoring of cerebral oxygenation in the newborn infant. *Department of Medical Physics and Bioengineering*, page 342, 1991.

[14] Steven L Jacques. Optical properties of biological tissues: a review. *Physics in medicine and biology*, 58(11):R37, 2013.

[15] Lihong Wang, Steven L Jacques, and Liqiong Zheng. Mcml - monte carlo modeling of light transport in multi-layered tissues. *Computer methods and programs in biomedicine*, 47(2):131–146, 1995.

[16] M Cope, D T Delpy, E O Reynolds, S Wray, J Wyatt, and P van der Zee. Methods of quantitating cerebral near infrared spectroscopy data. *Adv. Exp. Med. Biol.*, 222:183–189, 1988.

[17] Alessandro Torricelli, Davide Contini, Antonio Pifferi, Matteo Caffini, Rebecca Re, Lucia Zucchelli, and Lorenzo Spinelli. Time domain functional nirs imaging for human brain mapping. *Neuroimage*, 85:28–50, 2014.

[18] Jorge Ripoll. Derivation of the scalar radiative transfer equation from energy conservation of maxwells equations in the far field. *JOSA A*, 28(8):1765–1775, 2011.

[19] Sergio Fantini and Maria Angela Franceschini. Frequency-domain techniques for tissue spectroscopy and imaging. *Handbook of optical biomedical diagnostics*, 7:405–453, 2002.

[20] R. C. Haskell, L. O. Svaasand, T. T. Tsay, T. C. Feng, M. S. McAdams, and B. J. Tromberg. Boundary conditions for the diffusion equation in radiative transfer. *J Opt Soc Am A Opt Image Sci Vis*, 11(10):2727–2741, Oct 1994.

[21] John Mathews and Russell Howell. *Complex analysis for mathematics and engineering*. Jones & Bartlett Publishers, 2012.

[22] Nunu Ren, Jimin Liang, Xiaochao Qu, Jianfeng Li, Bingjia Lu, and Jie Tian. Gpu-based monte carlo simulation for light propagation in complex heterogeneous tissues. *Optics express*, 18(7):6811–6823, 2010.

[23] William Chun Yip Lo, Tianyi David Han, Jonathan Rose, and Lothar Lilge. Gpu-accelerated monte carlo simulation for photodynamic therapy treatment planning. In *European Conferences on Biomedical Optics*, pages 737313–737313. International Society for Optics and Photonics, 2009.

[24] Erik Alerstam, William Chun Yip Lo, Tianyi David Han, Jonathan Rose, Stefan Andersson-Engels, and Lothar Lilge. Next-generation acceleration and code optimization for light transport in turbid media using gpus. *Biomedical optics express*, 1(2):658–675, 2010.

[25] Qianqian Fang and David A Boas. Monte carlo simulation of photon migration in 3d turbid media accelerated by graphics processing units. *Optics express*, 17(22):20178, 2009.

[26] SR Arridge, M Schweiger, M Hiraoka, and DT Delpy. A finite element approach for modeling photon transport in tissue. *Medical physics*, 20(2):299–309, 1993.

[27] M Schweiger, SR Arridge, M Hiraoka, and DT Delpy. The finite element method for the propagation of light in scattering media: boundary and source conditions. *Medical physics*, 22(11):1779–1792, 1995.

[28] Walter Egan and Theodore W Hilgeman. *Optical properties of inhomogeneous materials : applications to geology, astronomy, chemistry, and engineering*. Academic Press, New York, 1979.

[29] Marleen Keijzer, Willem M Star, and Pascal RM Storchi. Optical diffusion in layered media. *Applied Optics*, 27(9):1820–1824, 1988.

[30] Donald W Marquardt. An algorithm for least-squares estimation of nonlinear parameters. *Journal of the Society for Industrial & Applied Mathematics*, 11(2):431–441, 1963.

[31] Simon R Arridge. Optical tomography in medical imaging. *Inverse problems*, 15(2):R41, 1999.

[32] Gary Strangman, Maria Angela Franceschini, and David A Boas. Factors affecting the accuracy of near-infrared spectroscopy concentration calculations for focal changes in oxygenation parameters. *Neuroimage*, 18(4):865–879, 2003.

[33] Douglas C Montgomery, Elizabeth A Peck, and G Geoffrey Vining. *Introduction to linear regression analysis*, volume 821. John Wiley & Sons, 2012.

[34] T J Huppert, S G Diamond, M A Franceschini, and D A Boas. Homer: a review of time-series analysis methods for near-infrared spectroscopy of the brain. *Appl. Opt.*, 48(10):280–298, Apr 2009.

[35] Jeffrey W Barker, Ashok Panigrahy, and Theodore J Huppert. Accuracy of oxygen saturation and total hemoglobin estimates in the neonatal brain using the semi-infinite slab model for fd-nirs data analysis. *Biomedical Optics Express*, 5(12):4300–4312, 2014.

[36] F F Jöbsis. Noninvasive, infrared monitoring of cerebral and myocardial oxygen sufficiency and circulatory parameters. *Science*, 198(4323):1264–1267, Dec 1977.

[37] Maria Angela Franceschini, Sonal Thaker, George Themelis, Kalpathy K Krishnamoorthy, Heather Bortfeld, Solomon G Diamond, David A Boas, Kara Arvin, and P Ellen Grant. Assessment of infant brain development with frequency-domain near-infrared spectroscopy. *Pediatric research*, 61:546–551, 2007.

[38] Frank van Bel, Petra Lemmers, and Gunnar Naulaers. Monitoring neonatal regional cerebral oxygen saturation in clinical practice: value and pitfalls. *Neonatology*, 94(4):237–244, 2008.

[39] Sergio Fantini, Maria Angela Franceschini, and Enrico Gratton. Semi-infinite-geometry boundary problem for light migration in highly scattering media: a frequency-domain study in the diffusion approximation. *JOSA B*, 11(10):2128–2138, 1994.

[40] Mathieu Dehaes, P. Ellen Grant, Danielle D. Sliva, Nadège Roche-Labarbe, Rudolph Pienaar, David A. Boas, Maria Angela Franceschini, and Juliette Selb. Assessment of the frequency-domain multi-distance method to evaluate the brain optical properties: Monte carlo simulations from neonate to adult. *Biomedical optics express*, 2(3):552–567, Feb 2011.

[41] C Rebecca Simpson, Matthias Kohl, Matthias Essenpreis, and Mark Cope. Near-infrared optical properties of ex vivo human skin and subcutaneous tissues measured using the monte carlo inversion technique. *Physics in medicine and biology*, 43(9):2465, 1998.

[42] M Firbank, M Hiraoka, M Essenpreis, and DT Delpy. Measurement of the optical properties of the skull in the wavelength range 650-950 nm. *Physics in Medicine and Biology*, 38(4):503, 1993.

[43] S A Prahl. Optical absortpion of hemoglobin, 1999.

[44] S A Prahl. Optical absorption of water, 2012.

[45] Sergio Fantini, Beniamino B Barbieri, Enrico Gratton, Maria-Angela Franceschini, John S Maier, and Scott A Walker. Frequency-domain multichannel optical detector for noninvasive tissue spectroscopy and oximetry. *Optical Engineering*, 34(1):32–42, 1995.

[46] Feng Shi, Pew-Thian Yap, Guorong Wu, Hongjun Jia, John H Gilmore, Weili Lin, and Dinggang Shen. Infant brain atlases from neonates to 1-and 2-year-olds. *PLoS One*, 6(4):e18746, 2011.

[47] Gerhard Nellhaus. Head circumference from birth to eighteen years practical composite international and interracial graphs. *Pediatrics*, 41(1):106–114, 1968.

[48] Qianqian Fang and David A Boas. Tetrahedral mesh generation from volumetric binary and grayscale images. In *Biomedical Imaging: From Nano to Macro, 2009. ISBI'09. IEEE International Symposium on*, pages 1142–1145. IEEE, 2009.

[49] Hamid Dehghani, Matthew E Eames, Phaneendra K Yalavarthy, Scott C Davis, Subhadra Srinivasan, Colin M Carpenter, Brian W Pogue, and Keith D Paulsen. Near infrared optical tomography using nirfast: Algorithm for numerical model and image reconstruction. *Communications in numerical methods in engineering*, 25(6):711–732, 2009.

[50] Anna Custo, William M Wells Iii, Alex H Barnett, Elizabeth Hillman, and David A Boas. Effective scattering coefficient of the cerebral spinal fluid in adult head models for diffuse optical imaging. *Applied optics*, 45(19):4747–4755, 2006.

[51] Jeffrey W Barker, Ardalan Aarabi, and Theodore J Huppert. Autoregressive model based algorithm for correcting motion and serially correlated errors in fnirs. *Biomedical optics express*, 4(8):1366–1379, 2013.

[52] F Scholkmann, S Spichtig, T Muehlemann, and M Wolf. How to detect and reduce movement artifacts in near-infrared imaging using moving standard deviation and spline interpolation. *Physiol. Meas.*, 31(5):649–662, May 2010.

[53] B Molavi and G A Dumont. Wavelet-based motion artifact removal for functional near-infrared spectroscopy. *Physiol. Meas.*, 33(2):259–270, Feb 2012.

[54] M Izzetoglu, P Chitrapu, S Bunce, and B Onaral. Motion artifact cancellation in nir spectroscopy using discrete kalman filtering. *Biomed. Eng. Online*, 9:16–16, 2010.

[55] R J Cooper, J Selb, L Gagnon, D Phillip, H W Schytz, H K Iversen, M Ashina, and D A Boas. A systematic comparison of motion artifact correction techniques for functional near-infrared spectroscopy. *Front. Neurosci.*, 6:147–147, 2012.

[56] J C Ye, S Tak, K E Jang, J Jung, and J Jang. Nirs-spm: statistical parametric mapping for near-infrared spectroscopy. *Neuroimage*, 44(2):428–447, Jan 2009.

[57] G H Orcutt and D Cochrane. A sampling study of the merits of autoregressive and reduced form transformation in regression analysis. *J. Am. Stat. Assoc.*, 44(247):356–372, Sep 1949.

[58] M J Hofmann, M J Herrmann, I Dan, H Obrig, M Conrad, L Kuchinke, A M Jacobs, and A J Fallgatter. Differential activation of frontal and parietal regions during visual word recognition: an optical topography study. *Neuroimage*, 40(3):1340–1349, Apr 2008.

[59] M M Plichta, M J Herrmann, C G Baehne, A C Ehlis, M M Richter, P Pauli, and A J Fallgatter. Event-related functional near-infrared spectroscopy (fnirs): are the measurements reliable? *Neuroimage*, 31(1):116–124, May 2006.

[60] M M Plichta, S Heinzel, A C Ehlis, P Pauli, and A J Fallgatter. Model-based analysis of rapid event-related functional near-infrared spectroscopy (nirs) data: a parametric validation study. *Neuroimage*, 35(2):625–634, Apr 2007.

[61] Andrew C Harvey. *The econometric analysis of time series*. MIT Press, 1990.

[62] TP Speed and Bin Yu. Model selection and prediction: normal regression. *Ann. I. Stat. Math.*, 45(1):35–54, 1993.

[63] Karl J Friston, John T Ashburner, Stefan J Kiebel, Thomas E Nichols, and William D Penny. *Statistical Parametric Mapping: The Analysis of Functional Brain Images: The Analysis of Functional Brain Images*. Academic Press, 2011.

[64] A M Dale. Optimal experimental design for event-related fmri. *Hum. Brain Mapp.*, 8(2-3):109–114, 1999.

[65] S G Diamond, T J Huppert, V Kolehmainen, M A Franceschini, J P Kaipio, S R Arridge, and D A Boas. Dynamic physiological modeling for functional diffuse optical tomography. *Neuroimage*, 30(1):88–101, Mar 2006.

[66] Paul W Holland and Roy E Welsch. Robust regression using iteratively reweighted least-squares. *Commun. Stat.-Theor. M.*, 6(9):813–827, 1977.

[67] Albert E Beaton and John W Tukey. The fitting of power series, meaning polynomials, illustrated on band-spectroscopic data. *Technometrics*, 16(2):147–185, 1974.

[68] Peter J Huber. Robust regression: asymptotics, conjectures and monte carlo. *The Annals of Statistics*, 1(5):799–821, 1973.

[69] Susan B Perlman, Beatriz Luna, Tyler C Hein, and Theodore J Huppert. fnirs evidence of prefrontal regulation of frustration in early childhood. *Neuroimage*, 85:326–334, 2014.

[70] Ranganatha Sitaram, Haihong Zhang, Cuntai Guan, Manoj Thulasidas, Yoko Hoshi, Akihiro Ishikawa, Koji Shimizu, and Niels Birbaumer. Temporal classification of multichannel near-infrared spectroscopy signals of motor imagery for developing a brain–computer interface. *NeuroImage*, 34(4):1416–1427, 2007.

[71] Shirley M Coyle, Tomas E Ward, and Charles M Markham. Brain–computer interface using a simplified functional near-infrared spectroscopy system. *Journal of neural engineering*, 4(3):219, 2007.

[72] Angela R Harrivel, Daniel H Weissman, Douglas C Noll, and Scott J Peltier. Monitoring attentional state with fnirs. *Frontiers in human neuroscience*, 7, 2013.

[73] Susan R Hintz, David A Benaron, Andrew M Siegel, Anna Zourabian, David K Stevenson, and David A Boas. Bedside functional imaging of the premature infant brain during passive motor activation. *Journal of perinatal medicine*, 29(4):335–343, 2001.

[74] Nikolaus Weiskopf. Real-time fmri and its application to neurofeedback. *Neuroimage*, 62(2):682–692, 2012.

[75] Rudolph Emil Kalman. A new approach to linear filtering and prediction problems. *Journal of Fluids Engineering*, 82(1):35–45, 1960.

[76] Pere Vendrell, Carme Junqué, Jesús Pujol, M Jurado, Joan Molet, and Jordan Grafman. The role of prefrontal regions in the stroop task. *Neuropsychologia*, 33(3):341–352, 1995.

[77] John G Kerns, Jonathan D Cohen, Angus W MacDonald, Raymond Y Cho, V Andrew Stenger, and Cameron S Carter. Anterior cingulate conflict monitoring and adjustments in control. *Science*, 303(5660):1023–1026, 2004.

[78] Steven D Wolff and Robert S Balaban. Magnetization transfer contrast (mtc) and tissue water proton relaxation in vivo. *Magn Reson Med*, 10(1):135–144, 1989.

[79] RM Henkelman, GJ Stanisz, and SJ Graham. Magnetization transfer in mri: a review. *NMR Biomed*, 14(2):57–64, 2001.

[80] Klaus Schmierer, Francesco Scaravilli, Daniel R Altmann, Gareth J Barker, and David H Miller. Magnetization transfer ratio and myelin in postmortem multiple sclerosis brain. *Ann Neurol*, 56(3):407–415, 2004.

[81] Didier Laurent, James Wasvary, Jianyun Yin, Markus Rudin, Theodore C Pellas, and Elizabeth OByrne. Quantitative and qualitative assessment of articular cartilage in the goat knee with magnetization transfer imaging. *Magn Reson Imaging*, 19(10):1279–1286, 2001.

[82] Goetz H Welsch, Siegfried Trattnig, Klaus Scheffler, Pavol Szomonanyi, Sebastian Quirbach, Stefan Marlovits, Stephan Domayer, Oliver Bieri, and Tallal C Mamisch. Magnetization transfer contrast and t2 mapping in the evaluation of cartilage repair tissue with 3t mri. *J Magn Reson Imaging*, 28(4):979–986, 2008.

[83] Steven D Wolff, Scott Chesnick, JA Frank, KO Lim, and RS Balaban. Magnetization transfer contrast: Mr imaging of the knee. *Radiology*, 179(3):623–628, 1991.

[84] Chenyang Wang, Walter Witschey, Ari Goldberg, Mark Elliott, Arijitt Borthakur, and Ravinder Reddy. Magnetization transfer ratio mapping of intervertebral disc degeneration. *Magn Reson Med*, 64(5):1520–1528, 2010.

[85] Ayumi Okumura, Katsunobu Takenaka, Yasuaki Nishimura, Yoshitaka Asano, Noboru Sakai, Kazuo Kuwata, and Seiichi Era. The characterization of human brain tumor using magnetization transfer technique in magnetic resonance imaging. *Neurol Res*, 21(3):250–254, 1999.

[86] Margaret H Pui. Magnetization transfer analysis of brain tumor, infection, and infarction. *J Magn Reson Imaging*, 12(3):395–399, 2000.

[87] W Thomas Dixon, Hans Engels, Mauricio Castillo, and Maziar Sardashti. Incidental magnetization transfer contrast in standard multislice imaging. *Magn Reson Imaging*, 8(4):417–422, 1990.

[88] PS Melki and RV Mulkern. Magnetization transfer effects in multislice rare sequences. *Magn Reson Med*, 24(1):189–195, 1992.

[89] Giles E Santyr. Magnetization transfer effects in multislice mr imaging. *Magn Reson Imaging*, 11(4):521–532, 1993.

[90] Matthias Weigel, Gunther Helms, and Juergen Hennig. Investigation and modeling of magnetization transfer effects in two-dimensional multislice turbo spin echo sequences with low constant or variable flip angles at 3 t. *Magn Reson Med*, 63(1):230–234, 2010.

[91] Sung-Hong Park and Timothy Q Duong. Alternate ascending/descending directional navigation approach for imaging magnetization transfer asymmetry. *Magn Reson Med*, 65(6):1702–1710, 2011.

[92] SJ Graham and R Mark Henkelman. Understanding pulsed magnetization transfer. *J Magn Reson Imaging*, 7(5):903–912, 1997.

[93] Clare Morrison, Greg Stanisz, and R Mark Henkelman. Modeling magnetization transfer for biological-like systems using a semi-solid pool with a super-lorentzian lineshape and dipolar reservoir. *Journal of Magnetic Resonance, Series B*, 108(2):103–113, 1995.

[94] Jun Hua, Craig K Jones, Jaishri Blakeley, Seth A Smith, Peter van Zijl, and Jinyuan Zhou. Quantitative description of the asymmetry in magnetization transfer effects around the water resonance in the human brain. *Magn Reson Med*, 58(4):786–793, 2007.

[95] O Bieri and K Scheffler. On the origin of apparent low tissue signals in balanced ssfp. *Magn Reson Med*, 56(5):1067–1074, 2006.

[96] M Gloor, K Scheffler, and O Bieri. Quantitative magnetization transfer imaging using balanced ssfp. *Magn Reson Med*, 60(3):691–700, 2008.

[97] Greg J Stanisz, Ewa E Odrobina, Joseph Pun, Michael Escaravage, Simon J Graham, Michael J Bronskill, and R Mark Henkelman. T1, t2 relaxation and magnetization transfer in tissue at 3t. *Magn Reson Med*, 54(3):507–512, 2005.

[98] Oliver Bieri, Tallas C Mamisch, Siegfried Trattnig, and Klaus Scheffler. Steady state free precession magnetization transfer imaging. *Magn Reson Med*, 60(5):1261–1266, 2008.

[99] O Bieri and K Scheffler. Optimized balanced steady-state free precession magnetization transfer imaging. *Magn Reson Med*, 58(3):511–518, 2007.

[100] Sung-Hong Park, Tiejun Zhao, Jung-Hwan Kim, Fernando E Boada, and Kyongtae Ty Bae. Suppression of effects of gradient imperfections on imaging with alternate ascending/descending directional navigation. *Magn Reson Med*, 68(5):1600–1606, 2012.

[101] Sung-Hong Park and Timothy Q Duong. Brain mr perfusion-weighted imaging with alternate ascending/descending directional navigation. *Magn Reson Med*, 65(6):1578–1591, 2011.

[102] Meritxell Garcia, Monika Gloor, Oliver Bieri, Stephan G Wetzel, Ernst-Wilhelm Radue, and Klaus Scheffler. Mtr variations in normal adult brain structures using balanced steady-state free precession. *Neuroradiology*, 53(3):159–167, 2011.